Appendix A

Characteristics of Spherical Electrostatic Analyzers (LEP-EA, SW) onboard the GEOTAIL Satellite

Two of the low energy particle experiment (LEP) sensors, LEP-EA and LEP-SW, on the GEOTAIL satellite are both spherical electrostatic analyzers. These analyzers are designed on the basis of the results of a numerical calculation, and their transmission characteristics are verified by experimental calibration in the laboratory. In this appendix, the method of numerical calculation and the method of experimental calibration of LEP-EA and LEP-SW with detailed characteristics of these analyzers are presented.

A.1 Numerical Calculation of the Transmission Characteristics of LEP-EA and LEP-SW

In order to decide the optimized parameters of the analyzers, we have calculated the transmission characteristics of the instruments. The calculation technique we have used is primarily the same as that of Mukai et al.[1986]. Since LEP-EA and LEP-SW are both spherical electrostatic analyzers, we can use the same formula in calculation. In this appendix, we will derive equations assuming 90° spherical electrostatic analyzer. Figure A.1 shows a trajectory of a charged particle in the orbit plane on a cross section of a spherical section analyzer. The equation of the particle trajectory is given by

$$\frac{r_0}{r} = \frac{1}{(1+\delta\prime)\cos^2\alpha} - \tan\alpha\sin\phi + (1 - \frac{1}{(1+\delta\prime)\cos^2\alpha})\cos\phi \qquad \text{(A.1)}$$

$$\delta' = \frac{E(r_0) - E_0(r_0)}{E_0(r_0)} \qquad \text{(A.2)}$$

where $E_0(r_0)$ is the kinetic energy of a particle which executes a circular orbit of radius r_0, and $E(r_0)$ is the kinetic energy of a particle at the entrance edge of the analyzer plates $r = r_0$. The conditions that a particle which has the trajectory expressed by the equation (A.1) can pass through the spherical section analyzer are as follows.

1. Trajectory of the particle should intersect the exit edge of the analyzer plates at $r = r_\Phi$, where

$$R_1 < r_\Phi < R_2.$$

Using the equations (A.1) and (A.2) this condition can be expressed in terms of δ'. Substituting Φ for ϕ in (A.1) and solving this equation for δ', we obtain

$$\delta' = \frac{1 - \cos\Phi}{\frac{r_0}{r}\cos^2\alpha - \cos\alpha\cos(\alpha + \Phi)} - 1 \tag{A.3}$$

If we let δ'_{11} and δ'_{12} as δ' when $r = R_1$ and $r = R_2$, respectively, the condition can be expressed as follows.

$$\delta'_{11} < \delta' < \delta'_{12} \tag{A.4}$$

$$\delta'_{11} = \frac{(1 - \cos\Phi)}{\frac{r_0}{R_1}\cos^2\alpha - \cos\alpha\cos(\alpha + \Phi)} - 1 \tag{A.5}$$

$$\delta'_{12} = \frac{(1 - \cos\Phi)}{\frac{r_0}{R_2}\cos^2\alpha - \cos\alpha\cos(\alpha + \Phi)} - 1 \tag{A.6}$$

2. While a particle passes through the spherical analyzer, r has to be in the range $R_1 < r < R_2$ for all ϕ. Changing the formula (A.1), we have

$$\frac{r_0}{r} = \frac{1}{(1+\delta\prime)\cos^2\alpha} + \{(1 - \frac{1}{(1+\delta\prime)\cos^2\alpha})^2 + \tan^2\alpha\}^{\frac{1}{2}}\cos(\phi + \beta_1) \tag{A.7}$$

where β_1 is defined as

$$\cos\beta_1 = \frac{1 - \frac{1}{(1+\delta\prime)\cos^2\alpha}}{\{(1 - \frac{1}{(1+\delta\prime)\cos^2\alpha})^2 + \tan^2\alpha\}^{\frac{1}{2}}} \tag{A.8}$$

$$\sin\beta_1 = \frac{\tan\alpha}{\{(1-\frac{1}{(1+\delta t)\cos^2\alpha})^2+\tan^2\alpha\}^{\frac{1}{2}}}. \tag{A.9}$$

The variable r has the maximum value r_{max} when $\cos(\phi+\beta_1) = -1$, and the minimum value r_{min} when $\cos(\phi+\beta_1) = 1$. Therefore we obtain

$$\phi_{max} = \pi - \beta_1 \tag{A.10}$$

$$\phi_{min} = -\beta_1 \tag{A.11}$$

$$r_{max} = \frac{r_0}{\frac{1}{(1+\delta t)\cos^2\alpha} - \{(1-\frac{1}{(1+\delta t)\cos^2\alpha})^2+\tan^2\alpha\}^{\frac{1}{2}}} \tag{A.12}$$

$$r_{min} = \frac{r_0}{\frac{1}{(1+\delta t)\cos^2\alpha} + \{(1-\frac{1}{(1+\delta t)\cos^2\alpha})^2+\tan^2\alpha\}^{\frac{1}{2}}} \tag{A.13}$$

Using (A.10)$\sim$(A.13), the condition can be expressed as follows.

$$0 \le \phi_{max} \le \Phi \text{ and } R_1 \le r_{max} \le R_2 \tag{A.14}$$

or

$$0 \le \phi_{min} \le \Phi \text{ and } R_1 \le r_{min} \le R_2 \tag{A.15}$$

So far, we have derived two conditions for a particle to pass through the spherical electrostatic analyzer. The conditions are written in the particle orbit plane coordinate system. To compare the calculated results with the results of calibration, we must express those conditions in the spacecraft coordinate system. Strictly speaking, the spacecraft coordinate system and the coordinate system used in the calibration is different. This point will be discussed later. The spacecraft coordinate system is defined as Figure A.2.

The equation of transformation is

$$\sin\alpha = -\cos\theta\sin\beta\cos\psi - \sin\theta\sin\psi, \tag{A.16}$$

where θ and β are the polar and azimuthal angles measured in the spacecraft system, ψ is the aperture angle of the incident point, and α is defined in Figure A.1. Solving the equation (A.16) for α, we have

$$\alpha = \arcsin(-\cos\theta\sin\beta\cos\psi - \sin\theta\sin\psi), \tag{A.17}$$

where $\mid \alpha \mid \leq \pi/2$.

The electrostatic potential at the entrance edge of the analyzer plates is generally not the same as that at infinity. Therefore, we define a relative energy δ as

$$\delta = \frac{E_\infty(r_0) - E_{\infty 0}(r_c)}{E_{\infty 0}(r_c)} \tag{A.18}$$

where $r_c = (R_1 + R_2)/2$, $E_\infty(r_0)$ is the kinetic energy at infinity of a particle injected into the spherical analyzer at $r = r_0$, and $E_{\infty 0}(r_c)$ is the kinetic energy at infinity of a particle which executes a circular orbit of radius r_c. When we apply voltage V to the outer sphere, and voltage $-$V to the inner sphere, $E_\infty(r_0)$, $E_{\infty 0}(r_c)$, $E(r_0)$, and $E(r_c)$ are expressed as follows.

$$E_\infty(r_0) = E(r_0) - qV + \frac{2R_2q}{R_2 - R_1}V - \frac{2qVR_2R_1}{r_0(R_2 - R_1)} \tag{A.19}$$

$$E_{\infty 0}(r_c) = E_0(r_c) - qV + \frac{2R_2q}{R_2 - R_1}V - \frac{2qVR_2R_1}{r_0(R_2 - R_1)} \tag{A.20}$$

$$E(r_0) = (\delta' + 1)E_0(r_0) \tag{A.21}$$

$$E_0(r_c) = \frac{1}{r_c}\frac{qVR_1R_2}{R_2 - R_1} \tag{A.22}$$

where q is the electric charge of a particle. Then we obtain the relation between relative energy δ and the variable δ' defined by equation (A.2) as below.

$$\delta = \frac{2R_1R_2}{R_1^2 + R_2^2}\{(\delta' - 1)\frac{r_c}{r_0} + 1\} \tag{A.23}$$

The effective bending angle Φ_e is a function of the aperture angle of the incident point ψ and the incident azimuthal and elevation angles of a particle β and θ. The aperture angle ψ_{out} of the output point and the projection angles θ''_{out} and β''_{out} of a particle at the exit edge of the analyzer plates are also functions of ψ, β, and θ. Here, ψ_{out}, θ''_{out}, and β''_{out} are defined in Figure A.3. Here, we will express Φ_e, ψ_{out}, θ''_{out}, and β''_{out} by ψ, β, and θ. Figure A.4 shows the orbit of a particle projected on the inner sphere. In this figure, O is the center of the sphere, A is the point projected on the entrance edge of the analyzer plates $\psi = 0$, C is the incident point, D is the exit point, and E is the point projected on the exit edge of the analyzer plates $\psi_{out} = 0$. Figures A.6~A.9 show developments of Figure A.4. The variables θ''_{out2} and β''_{out} are defined in Figure A.5. Using formulas of spherical trigonometry, we obtain

$$\sin\theta''_{out2} = \cos\Phi\sin\theta''_2 + \sin\Phi\cos\theta''_2\sin\psi \tag{A.24}$$

$$\frac{\cos\psi}{\cos\theta''_{out2}} = \frac{\cos\psi_{out}}{\cos\theta''} = \frac{\sin(\Phi + \Delta\Phi)}{\sin\Phi} \tag{A.25}$$

$$\Delta\Phi = \Phi_e - \Phi \tag{A.26}$$

$$\sin\psi_{out} = \sin\psi\cos(\Phi+\Delta\Phi) - \cos\psi\sin(\Phi+\Delta\Phi)\sin\theta_2'' \tag{A.27}$$

where θ_2'' is defined in Figure A.4(c), θ_{out2}'', Φ, ψ, and Φ_e are the same as before. From (A.24) we have

$$\theta_{out2}'' = \arcsin(\cos\Phi\sin\theta_2'' + \sin\Phi\cos\theta_2''\sin\psi) \tag{A.28}$$

and from (A.25) we have

$$\sin(\Phi+\Delta\Phi) = \frac{\cos\psi}{\cos\theta_{out2}''}\sin\Phi. \tag{A.29}$$

Applying formulas of spherical trigonometry to Figures A.8 and A.9, we have

$$\cos C = \cos\psi\cos(\Phi+\Delta\Phi) + \sin(\Phi+\Delta\Phi)\sin\psi\sin\theta_2'' \tag{A.30}$$

$$\cos C = \cos\Phi\cos\psi_{out} \tag{A.31}$$

and from (A.30) and (A.31)

$$\cos(\Phi+\Delta\Phi) = \frac{\cos\Phi\cos\psi_{out} - \sin(\Phi+\Delta\Phi)\sin\psi\sin\theta_2''}{\cos\psi}. \tag{A.32}$$

Arranging (A.24)$\sim$(A.32) we obtain following formulas.

$$\theta_{out2}'' = \arcsin(\cos\Phi\sin\theta_2'' + \sin\Phi\cos\theta_2''\sin\psi) \tag{A.33}$$

$$\sin(\Phi+\Delta\Phi) = \frac{\cos\psi}{\cos\theta_{out2}''}\sin\Phi \tag{A.34}$$

$$\cos(\Phi+\Delta\Phi) = \frac{\frac{\cos\Phi\cos\theta_2''\cos\psi}{\cos\theta_{out2}''} - \frac{\cos\psi\sin\Phi\sin\psi\sin\theta_2''}{\cos\theta_{out2}''}}{\cos\psi} \tag{A.35}$$

$$\sin\psi_{out} = \sin\psi\cos(\Phi+\Delta\Phi) - \cos\psi\sin(\Phi+\Delta\Phi)\sin\theta_2''. \tag{A.36}$$

The relations among θ_2'', θ'' and β'', among θ_{out2}'', θ_{out}'' and β_{out}'', and among θ'', β'', θ and β are as follows.

$$\tan\theta_2'' = \frac{\tan\theta''}{\cos\beta''} \tag{A.37}$$

$$\tan\theta_{out2}'' = \frac{\tan\theta_{out}''}{\cos\beta_{out}''} \tag{A.38}$$

$$\cos\theta''\sin\beta'' = \cos\theta\sin\beta\cos\psi - \sin\theta\sin\psi \tag{A.39}$$

$$\sin\theta'' = \cos\theta\sin\beta\cos\psi + \sin\theta\cos\psi \tag{A.40}$$

To express θ_{out}'' and β_{out}'' in terms of ψ, β and θ, we define a variable α_{out} (see Figure A.1).

$$\tan\alpha_{out} = \frac{r_{out}}{r_0}\{\tan\alpha\cos\Phi_e + (1 - \frac{1}{(1+\delta')\cos^2\alpha})\sin\Phi_e\} \tag{A.41}$$

$$\alpha_{out} = \arctan\{\frac{r_{out}}{r_0}(\tan\alpha\cos\Phi_e + (1 - \frac{1}{(1+\delta')\cos^2\alpha})\sin\Phi_e\}. \tag{A.42}$$

A particle is ejected from the spherical analyzer at radius of r_{out},

$$r_{out} = \frac{r_0}{\frac{1}{(1+\delta')\cos^2\alpha} - \tan\alpha\sin\Phi_e + (1 - \frac{1}{(1+\delta')\cos^2\alpha})\cos\Phi_e}. \tag{A.43}$$

From (A.38) we have

$$\cos\beta_{out}'' = \frac{\tan\theta_{out}''}{\tan\theta_{out2}''}. \tag{A.44}$$

On the other hand, β_{out}'' satisfies

$$\sin\beta_{out}'' = \frac{\sin\alpha_{out}}{\cos\theta_{out}''} \tag{A.45}$$

From (A.44) and (A.45), we have

$$\sin\theta_{out}'' = \sin\theta_{out2}''\cos\alpha_{out} \tag{A.46}$$

so we have

$$\theta''_{out} = \arcsin(\sin\theta''_{out2}\cos\alpha_{out}) \tag{A.47}$$

$$\beta''_{out} = \arcsin(\frac{\sin\alpha_{out}}{\cos\theta''_{out}}). \tag{A.48}$$

Using the results obtained above, we can rewrite the conditions that a particle can pass through the spherical electrostatic analyzer in the spacecraft coordinate system. We want to know whether a particle can transmit the spherical electrostatic analyzer, when the parameters β, θ, r_0, ψ, and δ are specified. As for the condition 1 the procedure is as follows. First, we calculate θ'' and β'' from (A.39) and (A.40). Then using (A.37), we have θ''_2, and we can calculate $\Phi_e = \Phi + \Delta\Phi$ from (A.34) and (A.35). Then using (A.17), we calculate $\cos\alpha$ and $\cos(\alpha + \Phi_e)$. Substituting these into (A.5) and (A.6), we obtain δ'_{11} and δ'_{12}, in which we substitute Φ_e for Φ. Next, we can check if $\delta'_{11} < \delta' < \delta'_{12}$ or not, where δ' can be calculated from δ using (A.23). The condition 2 can be transformed as below. First, we calculate $\cos\alpha$ and $\tan\alpha$ using (A.17), δ' from δ using (A.23). Then substituting these into (A.8), (A.9), (A.12) and (A.13), we obtain β_1, r_{max}, and r_{min}. Finally, we can calculate ϕ_{max} and ϕ_{min} from (A.10) and (A.11), and examine the conditions (A.14) and (A.15).

An incident particle which can pass through the analyzer and be detected must satisfy some additional conditions that it can pass through collimators and slits of the instruments. Here, we will define a function $P(\beta, \theta, \delta, \psi, r_0)$

as follows.

$$P(\beta,\theta,\delta,\psi,r_0) = \begin{cases} 1 & \text{(when a particle is detected by MCP or CEM)} \\ 0 & \text{(when a particle is not detected by MCP or CEM)} \end{cases}$$

The E$-\alpha$ characteristics define the energy resolution and the angular response of the azimuthal field of view. The calculated E$-\alpha$ contour is a contour of the calculated count rate C_c which is a function of δ and α when θ is fixed. The calculated count rate C_c is defined as follows.

$$C_c(\delta,\alpha,\theta) = \int\int P(\beta,\theta,\delta,\psi,r_0)\cos\beta\cos\theta r_0 d\psi dr_0, \tag{A.49}$$

where, from equation (A.16), $\beta = \arcsin(-(\sin\alpha + \sin\theta\sin\psi)/(\cos\theta\cos\psi))$. The theoretical geometrical factor is obtained by integrating the calculated count rate C_c with respect to β, δ, and θ, and is defined as below.

$$g = \int\int\int\int\int P(\beta,\theta,\delta,\psi,r_0)\cos\beta(\cos\theta)^2 r_0 d\psi dr_0 d\beta d\theta d\delta.$$

Observed count rate C_o is converted to the differential flux by the next equation.

$$f = \frac{C_o}{\tau g E_0} \tag{A.50}$$

where τ is the sampling time, E_0 is the observed energy, and f is the differential flux. In order to use this relation, we have to assume that the flux is constant within the energy resolution and uniform within the field of view. If this assumption is not satisfied, we cannot use the relation (A.50), and we have to convert the observed count rate data to the differential flux considering the E$-\alpha$ characteristics.

We have calculated the integration of the geometrical factor by using quasi-random numbers. The integration is executed over the area as small as possible inside the range below.

$$\begin{cases} r_0 & (R_1 \leq r_0 \leq R_2) \\ \psi & (-\frac{\pi}{2} \leq \psi \leq \frac{\pi}{2}) \\ \beta & (-\frac{\pi}{2} \leq \beta \leq \frac{\pi}{2}) \\ \theta & (-\frac{\pi}{2} \leq \theta \leq \frac{\pi}{2}) \\ \delta & (-\infty \leq \delta \leq \infty). \end{cases}$$

A.2 Experimental Calibration of LEP-EA and LEP-SW

In theoretical calculation, we have assumed that the mechanical accuracy of the analyzer assembly is infinitely good, that there is no fringing field, and that the detection efficiency of the seven CEMs or MCPs are identical. Therefore we have to experimentally calibrate the characteristics of the analyzers before launching. The main purpose of the calibration is to obtain the geometrical factor, the field of view, and the energy resolution, which are essential for analyzing the flight data. In processing the data, we have drawn E$-\alpha$ contours which describe the energy resolution and the field of view.

The calibration is carried out as follows. Figure A.10 shows a schematic diagram of the calibration system. Analyzers are put on a two-axis gimbal platform in a vacuum chamber, and exposed to an ion beam with a fixed

energy from the ion source. Though one of the analyzers, LEP-EAe is an instrument to observe electrons, we have used ions for calibration. This is justified theoretically as follows. From the equations (A.1), (A.23), the motion of the charged particles is determined by the geometrical shape of the spheres, the injection angle of the incident particles, and the variable δ defined by (A.18), so the property of the particle is included in the variable δ. The relation between the voltage applied to the inner and outer spheres $-V$, V and the variable δ is expressed as

$$\delta = \frac{1}{V}\frac{E}{q}\frac{R_2^2 - R_1^2}{R_1^2 + R_2^2} - 1 \tag{A.51}$$

where E is the kinetic energy of the incident particle at infinity, q is the charge of a particle, R_1 and R_2 are the radii of the inner and the outer spheres, respectively. Since the mass of a charged particle is not included in the variable δ, we can use charged particles with arbitrary mass for calibration. If the effect due to the magnetic field, including the geomagnetic field is taken into account, there may be difference between using electrons with light mass and using ions with heavy mass. There may also be a difference in detection efficiency of the CEM between using electrons and using ions. As for the polarity of the charge, there is no difference in δ if we change the polarity of the voltages applied to the inner and outer spheres according to the polarity of the charge. In order to check the effectiveness of the suppresser mesh, we also have to change the polarity of the mesh potential.

We have to be careful about the injection angle of the incident particles.

By turning analyzers around the two axis of the turntable, we can change the azimuthal angle θ (defined in Figure A.3) and elevation angle of the gimbal γ. The elevation angle γ and the azimuthal angle of the analyzer α has a relation

$$\sin\alpha = \sin\gamma\cos\psi - \sin\psi\sin\theta \tag{A.52}$$

where ψ is defined in Figure A.2. We have to obtain count rate data as a function of the variable δ, the injection angle of the incident particles γ and θ in order to calibrate analyzers. We can change δ by changing E with V fixed, or by changing V with E fixed. Actually, we have changed V with E fixed, in order to keep the beam properties as stable as possible. When we draw the E$-\alpha$ contours, we draw contours of the obtained count rate data as a function of δ and γ with θ fixed. In drawing the E$-\alpha$ contours by calculation we have executed double integration over the area of the particle injection point of the analyzer. (see A.23) This integration is realized in calibration by injecting ion beam with sufficiently large area. As for the energy width of the beam, it must be much narrower than the energy resolution of the analyzer, and the angular width of the beam must be much narrower than the field of view of the analyzer, in order to obtain the E$-\alpha$ characteristics.

From the obtained experimental data, we have drawn E$-\alpha$ contours and have calculated geometrical factors. In calculating the geometrical factor, we have used the count rate data obtained for each channel by sweeping the voltage with the azimuthal angle θ and the elevation angle γ fixed. The

obtained count rate data are the function of azimuthal angle θ(deg), elevation angle γ(deg), and high voltage V(volt) applied to the spheres. Therefore we can express these count rate as $C_n(\theta, \gamma, V)$, where n represents channels (n=1,2,...,7). First, we transform these count rate from the function of θ, γ, V to the function of θ, γ, δ. As discussed above(see (A.51)), the relation between δ and V is theoretically as follows.

$$\delta = \frac{a}{V} - 1 \tag{A.53}$$

$$a = \frac{E_{fix}}{e} \frac{R_2^2 - R_1^2}{R_1^2 + R_2^2} \tag{A.54}$$

where e is unit charge, E_{fix} is the fixed energy of the ion beam, R_2 is the radius of the outer sphere, and R_1 is the radius of the inner sphere. Since the geometrical factor of each channel is different, we have changed the ion beam intensity to keep nearly the same count rate. We have used the data obtained by sweeping the azimuthal angle θ with the elevation angle γ and the voltage applied on analyzer plates fixed in order to correct the difference in beam parameters for each channel. Then we have normalized the count rate by the count rate $C_4(\theta = 0, \gamma = 0, \delta = 0)$, and defined the normalized count N_c as

$$N_c(\theta, \gamma, \delta) = \frac{C_n(\theta, \gamma, \delta)}{C_4(\theta = 0, \gamma = 0, \delta = 0)}. \tag{A.55}$$

Next we estimate the following quantity of d

$$d = \sum_{\theta} \sum_{\alpha} \sum_{\delta} N_c(\theta, \alpha, \delta) \Delta\theta \Delta\alpha \Delta\delta \tag{A.56}$$

where $\Delta\theta$, $\Delta\alpha$, and $\Delta\delta$ are increment of azimuthal angle, elevation angle, and energy, respectively. By multiplying the area of the incident surface by d, we can obtain the geometrical factor. We have obtained the area of the incident surface by numerical calculation.

A.3 Characteristics of LEP-EA and LEP-SW

Figures A.11-A.16 are examples of experimentally obtained E-α contours of EAe, EAi, and SW. Each figure consists of 7 panels. The E-α contour in the left-side of each figure is an E-α contour integrated over the azimuthal angle θ. At the right and at the bottom of the E-α contour, transmission characteristics with respect to the energy and elevation angle α are drawn. The panel at the bottom left of each figure shows transmission characteristics with respect to the azimuthal angle θ. The three panels at the right-side of each figure are E-α contours obtained at three different azimuthal angles. These E-α contours are drawn every 0.1 from 0.1 to 0.9 by normalizing the data. The E-α contours of the center channel (channel 4) of EAe and EAi show skewing characteristics of quadri-spherical analyzers. The E-α contour for the channel 1 with large polar angle are broad and the center direction of the field of view deviates from the mechanical center. The E-α contours of SW are compact, which enables us to observe solar wind ions with high angular and energy resolution.

The experimentally obtained geometrical factor, the energy resolution

(FWHM), the angular coverage (FWHM) and the center direction of field of view are summarized in Tables 2.2 and 2.5 in Chapter 2. We have designed the shape of the collimator of EAe and EAi so that the geometrical factor should be proportional to the cosine of the polar angle measured from the center channel of each analyzer. The experimentally obtained geometrical factors are nearly proportional to the cosine of the polar angle as we have expected.

Appendix B

Fast Plasma Velocity Moment Calculation with a Digital Signal Processor onboard the GEOTAIL Satellite

Plasma velocity moments up to the third order are calculated with a digital signal processor inside the low energy particle experiment common electronics (LEP-E) onboard the GEOTAIL satellite. Using the count rate data obtained by LEP-EA and LEP-SW, the velocity moments are calculated in one spin period (about 3 seconds). In this appendix we will present the detailed method of the velocity moment calculation and will discuss the accuracy of the calculated velocity moments.

B.1 Method of Velocity Moment Calculation

B.1.1 Velocity Moment Calculation on the Spacecraft

Plasma velocity moments up to the third order, density, bulk velocity vector, pressure tensor, and heat flux tensor of electrons, ions, and solar wind ions are calculated with a digital signal processor. The velocity moments are calculated from raw count rates obtained by two of the LEP sensors LEP-EA, and LEP-SW. A detailed description of the observation sequence and observed data of these sensors are presented in Chapter 2. The method of velocity moment calculation is basically the same for 3 species (electrons, ions, and solar wind ions). During one spin period (about 3 seconds) we obtain 3584 raw count rates for each species $C_{ijk}(i = 0 \sim 6, j = 0 \sim 15, k = 0 \sim 31)$ where the suffix 'i' stands for channel or elevation angle, 'j' stands for azimuthal angle, and 'k' stands for energy step. The formula of the calculated velocity moments are as follows.

$$n = \sum_{i=0}^{6}\sum_{j=0}^{15}\sum_{k=0}^{31} C_{ijk}\left(\frac{\frac{\Delta E_k}{E_k}\frac{1}{v_k}}{v_{norm}}\right)\left(\frac{(\Delta\theta)\alpha_i}{\alpha_{norm}}\right)\left\{(\Delta\phi)\frac{T_s}{\frac{g_i}{\cos\theta_i}}v_{norm}\alpha_{norm}\right\} \quad \text{(B.1)}$$

$$nV_x = \sum_{i=0}^{6}\sum_{j=0}^{15}\sum_{k=0}^{31} C_{ijk}\left(\frac{\frac{\Delta E_k}{E_k}}{d_{norm}}\right)\left(\frac{\cos\theta_i}{t_{norm}}\right)\left(\frac{\cos\phi_{jk}}{p_{norm}}\right)\left(\frac{(\Delta\theta)\alpha_i}{\alpha_{norm}}\right)$$
$$\left\{(\Delta\phi)\frac{T_s}{\frac{g_i}{\cos\theta_i}}d_{norm}t_{norm}p_{norm}\alpha_{norm}\right\} \quad \text{(B.2)}$$

$$nV_y = \sum_{i=0}^{6}\sum_{j=0}^{15}\sum_{k=0}^{31} C_{ijk}\left(\frac{\frac{\Delta E_k}{E_k}}{d_{norm}}\right)\left(\frac{\cos\theta_i}{t_{norm}}\right)\left(\frac{\sin\phi_{jk}}{p_{norm}}\right)\left(\frac{(\Delta\theta)\alpha_i}{\alpha_{norm}}\right)$$
$$\left\{(\Delta\phi)\frac{T_s}{\frac{g_i}{\cos\theta_i}} d_{norm} t_{norm} p_{norm} \alpha_{norm}\right\} \quad \text{(B.3)}$$

$$nV_z = \sum_{i=0}^{6}\sum_{j=0}^{15}\sum_{k=0}^{31} C_{ijk}\left(\frac{\frac{\Delta E_k}{E_k}}{d_{norm}}\right)\left(\frac{\sin\theta_i}{t_{norm}}\right)\left(\frac{(\Delta\theta)\alpha_i}{\alpha_{norm}}\right)$$
$$\left\{(\Delta\phi)\frac{T_s}{\frac{g_i}{\cos\theta_i}} d_{norm} t_{norm} \alpha_{norm}\right\} \quad \text{(B.4)}$$

$$P_{xx} = \sum_{i=0}^{6}\sum_{j=0}^{15}\sum_{k=0}^{31} C_{ijk}\left(\frac{\frac{\Delta E_k}{E_k} v_k}{v_{norm}}\right)\left(\frac{\cos^2\theta_i}{t_{norm}}\right)\left(\frac{\cos^2\phi_{jk}}{p_{norm}}\right)\left(\frac{(\Delta\theta)\alpha_i}{\alpha_{norm}}\right)$$
$$\left\{m(\Delta\phi)\frac{T_s}{\frac{g_i}{\cos\theta_i}} v_{norm} t_{norm} p_{norm} \alpha_{norm}\right\} \quad \text{(B.5)}$$

$$P_{yy} = \sum_{i=0}^{6}\sum_{j=0}^{15}\sum_{k=0}^{31} C_{ijk}\left(\frac{\frac{\Delta E_k}{E_k} v_k}{v_{norm}}\right)\left(\frac{\cos^2\theta_i}{t_{norm}}\right)\left(\frac{\sin^2\phi_{jk}}{p_{norm}}\right)\left(\frac{(\Delta\theta)\alpha_i}{\alpha_{norm}}\right)$$
$$\left\{m(\Delta\phi)\frac{T_s}{\frac{g_i}{\cos\theta_i}} v_{norm} t_{norm} p_{norm} \alpha_{norm}\right\} \quad \text{(B.6)}$$

$$P_{zz} = \sum_{i=0}^{6}\sum_{j=0}^{15}\sum_{k=0}^{31} C_{ijk}\left(\frac{\frac{\Delta E_k}{E_k} v_k}{v_{norm}}\right)\left(\frac{\sin^2\theta_i}{t_{norm}}\right)\left(\frac{(\Delta\theta)\alpha_i}{\alpha_{norm}}\right)$$
$$\left\{m(\Delta\phi)\frac{T_s}{\frac{g_i}{\cos\theta_i}} v_{norm} t_{norm} \alpha_{norm}\right\} \quad \text{(B.7)}$$

$$P_{xy} = \sum_{i=0}^{6}\sum_{j=0}^{15}\sum_{k=0}^{31} C_{ijk}\left(\frac{\frac{\Delta E_k}{E_k} v_k}{v_{norm}}\right)\left(\frac{\cos^2\theta_i}{t_{norm}}\right)\left(\frac{\sin\phi_{jk}\cos\phi_{jk}}{p_{norm}}\right)\left(\frac{(\Delta\theta)\alpha_i}{\alpha_{norm}}\right)$$
$$\left\{m(\Delta\phi)\frac{T_s}{\frac{g_i}{\cos\theta_i}} v_{norm} t_{norm} p_{norm} \alpha_{norm}\right\} \quad \text{(B.8)}$$

$$P_{yz} = \sum_{i=0}^{6}\sum_{j=0}^{15}\sum_{k=0}^{31} C_{ijk}\left(\frac{\frac{\Delta E_k}{E_k} v_k}{v_{norm}}\right)\left(\frac{\cos\theta_i\sin\theta_i}{t_{norm}}\right)\left(\frac{\sin\phi_{jk}}{p_{norm}}\right)\left(\frac{(\Delta\theta)\alpha_i}{\alpha_{norm}}\right)$$
$$\left\{m(\Delta\phi)\frac{T_s}{\frac{g_i}{\cos\theta_i}} v_{norm} t_{norm} p_{norm} \alpha_{norm}\right\} \quad \text{(B.9)}$$

$$P_{zx} = \sum_{i=0}^{6}\sum_{j=0}^{15}\sum_{k=0}^{31} C_{ijk}\left(\frac{\frac{\Delta E_k}{E_k}v_k}{v_{norm}}\right)\left(\frac{\cos\theta_i \sin\theta_i}{t_{norm}}\right)\left(\frac{\cos\phi_{jk}}{p_{norm}}\right)\left(\frac{(\Delta\theta)\alpha_i}{\alpha_{norm}}\right)$$
$$\left\{m(\Delta\phi)\frac{T_s}{\frac{g_i}{\cos\theta_i}}v_{norm}t_{norm}p_{norm}\alpha_{norm}\right\} \quad \text{(B.10)}$$

$$H_{xxx} = \sum_{i=0}^{6}\sum_{j=0}^{15}\sum_{k=0}^{31} C_{ijk}\left(\frac{\frac{\Delta E_k}{E_k}v_k^2}{v_{norm}}\right)\left(\frac{\cos^3\theta_i}{t_{norm}}\right)\left(\frac{\cos^3\phi_{jk}}{p_{norm}}\right)\left(\frac{(\Delta\theta)\alpha_i}{\alpha_{norm}}\right)$$
$$\left\{(\Delta\phi)\frac{T_s}{\frac{g_i}{\cos\theta_i}}v_{norm}t_{norm}p_{norm}\alpha_{norm}\right\} \quad \text{(B.11)}$$

$$H_{yyy} = \sum_{i=0}^{6}\sum_{j=0}^{15}\sum_{k=0}^{31} C_{ijk}\left(\frac{\frac{\Delta E_k}{E_k}v_k^2}{v_{norm}}\right)\left(\frac{\cos^3\theta_i}{t_{norm}}\right)\left(\frac{\sin^3\phi_{jk}}{p_{norm}}\right)\left(\frac{(\Delta\theta)\alpha_i}{\alpha_{norm}}\right)$$
$$\left\{(\Delta\phi)\frac{T_s}{\frac{g_i}{\cos\theta_i}}v_{norm}t_{norm}p_{norm}\alpha_{norm}\right\} \quad \text{(B.12)}$$

$$H_{zzz} = \sum_{i=0}^{6}\sum_{j=0}^{15}\sum_{k=0}^{31} C_{ijk}\left(\frac{\frac{\Delta E_k}{E_k}v_k^2}{v_{norm}}\right)\left(\frac{\sin^3\theta_i}{t_{norm}}\right)\left(\frac{(\Delta\theta)\alpha_i}{\alpha_{norm}}\right)$$
$$\left\{(\Delta\phi)\frac{T_s}{\frac{g_i}{\cos\theta_i}}v_{norm}t_{norm}\alpha_{norm}\right\} \quad \text{(B.13)}$$

$$H_{xyy} = \sum_{i=0}^{6}\sum_{j=0}^{15}\sum_{k=0}^{31} C_{ijk}\left(\frac{\frac{\Delta E_k}{E_k}v_k^2}{v_{norm}}\right)\left(\frac{\cos^3\theta_i}{t_{norm}}\right)\left(\frac{\sin^2\phi_{jk}\cos\phi_{jk}}{p_{norm}}\right)\left(\frac{(\Delta\theta)\alpha_i}{\alpha_{norm}}\right)$$
$$\left\{(\Delta\phi)\frac{T_s}{\frac{g_i}{\cos\theta_i}}v_{norm}t_{norm}p_{norm}\alpha_{norm}\right\} \quad \text{(B.14)}$$

$$H_{xzz} = \sum_{i=0}^{6}\sum_{j=0}^{15}\sum_{k=0}^{31} C_{ijk}\left(\frac{\frac{\Delta E_k}{E_k}v_k^2}{v_{norm}}\right)\left(\frac{\cos\theta_i\sin^2\theta_i}{t_{norm}}\right)\left(\frac{\cos\phi_{jk}}{p_{norm}}\right)\left(\frac{(\Delta\theta)\alpha_i}{\alpha_{norm}}\right)$$
$$\left\{(\Delta\phi)\frac{T_s}{\frac{g_i}{\cos\theta_i}}v_{norm}t_{norm}p_{norm}\alpha_{norm}\right\} \quad \text{(B.15)}$$

$$H_{yxx} = \sum_{i=0}^{6}\sum_{j=0}^{15}\sum_{k=0}^{31} C_{ijk}\left(\frac{\frac{\Delta E_k}{E_k}v_k^2}{v_{norm}}\right)\left(\frac{\cos^3\theta_i}{t_{norm}}\right)\left(\frac{\sin\phi_{jk}\cos^2\phi_{jk}}{p_{norm}}\right)\left(\frac{(\Delta\theta)\alpha_i}{\alpha_{norm}}\right)$$
$$\left\{(\Delta\phi)\frac{T_s}{\frac{g_i}{\cos\theta_i}}v_{norm}t_{norm}p_{norm}\alpha_{norm}\right\} \quad \text{(B.16)}$$

$$H_{yzz} = \sum_{i=0}^{6}\sum_{j=0}^{15}\sum_{k=0}^{31} C_{ijk}\left(\frac{\frac{\Delta E_k}{E_k}v_k^2}{v_{norm}}\right)\left(\frac{\cos\theta_i \sin^2\theta_i}{t_{norm}}\right)\left(\frac{\sin\phi_{jk}}{p_{norm}}\right)\left(\frac{(\Delta\theta)\alpha_i}{\alpha_{norm}}\right)$$
$$\{(\Delta\phi)\frac{T_s}{\frac{g_i}{\cos\theta_i}}v_{norm}t_{norm}p_{norm}\alpha_{norm}\} \quad \text{(B.17)}$$

$$H_{zxz} = \sum_{i=0}^{6}\sum_{j=0}^{15}\sum_{k=0}^{31} C_{ijk}\left(\frac{\frac{\Delta E_k}{E_k}v_k^2}{v_{norm}}\right)\left(\frac{\cos^2\theta_i \sin\theta_i}{t_{norm}}\right)\left(\frac{\cos^2\phi_{jk}}{p_{norm}}\right)\left(\frac{(\Delta\theta)\alpha_i}{\alpha_{norm}}\right)$$
$$\{(\Delta\phi)\frac{T_s}{\frac{g_i}{\cos\theta_i}}v_{norm}t_{norm}p_{norm}\alpha_{norm}\} \quad \text{(B.18)}$$

$$H_{zyy} = \sum_{i=0}^{6}\sum_{j=0}^{15}\sum_{k=0}^{31} C_{ijk}\left(\frac{\frac{\Delta E_k}{E_k}v_k^2}{v_{norm}}\right)\left(\frac{\cos^2\theta_i \sin\theta_i}{t_{norm}}\right)\left(\frac{\sin^2\phi_{jk}}{p_{norm}}\right)\left(\frac{(\Delta\theta)\alpha_i}{\alpha_{norm}}\right)$$
$$\{(\Delta\phi)\frac{T_s}{\frac{g_i}{\cos\theta_i}}v_{norm}t_{norm}p_{norm}\alpha_{norm}\} \quad \text{(B.19)}$$

$$H_{xyz} = \sum_{i=0}^{6}\sum_{j=0}^{15}\sum_{k=0}^{31} C_{ijk}\left(\frac{\frac{\Delta E_k}{E_k}v_k^2}{v_{norm}}\right)\left(\frac{\cos^2\theta_i \sin\theta_i}{t_{norm}}\right)\left(\frac{\sin\phi_{jk}\cos\phi_{jk}}{p_{norm}}\right)\left(\frac{(\Delta\theta)\alpha_i}{\alpha_{norm}}\right)$$
$$\{(\Delta\phi)\frac{T_s}{\frac{g_i}{\cos\theta_i}}v_{norm}t_{norm}p_{norm}\alpha_{norm}\} \quad \text{(B.20)}$$

$$q_x = H_{xxx} + H_{xyy} + H_{xzz} \quad \text{(B.21)}$$

$$q_y = H_{xxy} + H_{yyy} + H_{yzz} \quad \text{(B.22)}$$

$$q_z = H_{xxz} + H_{yyz} + H_{zzz} \quad \text{(B.23)}$$

The variable n stands for density, and $\mathbf{V}$, $\mathbf{P}$, $\mathbf{H}$, and $\mathbf{q}$ stand for bulk velocity vector, kinetic pressure tensor, kinetic heat flux tensor, and kinetic heat flux vector, respectively. In the above formula, ΔE_k, $\Delta\theta$, and $\Delta\phi$, are an energy gap between each energy step, an angle gap between channels, and an angle gap between the azimuthal angles of two successive sampling periods. Other variables, E_k, v_k, θ_i, ϕ_{jk}, α_i , T_s, and g_i stand for the center energy of energy step k, the particle velocity at the energy step k, the ele-

vation angle, the azimuthal angle, correction factor for geometrical factor of each channel, the reciprocal of sampling time, and geometrical factor of each channel, respectively. The geometrical factor of each channel is designed to be proportional to the cosine of the elevation angle. Therefore the quantity $g_i/\cos\theta_i$ is a constant of each sensor. Actually the geometrical factor is not strictly proportional to the cosine of the elevation angle. The correction factor for this deviation is given by α_i. We have calculated the quantity outside the medium parenthesis with the onboard digital signal processor, and multiplied the quantity inside the medium parenthesis on the ground. Each quantity inside the small parenthesis are tabulated in the memory of the processor, and multiplication and summation are executed. In the velocity moment calculation, the summation with respect to the suffix i is executed first. In doing this summation, we have used fixed-point 32-bit variables, in order to minimize the calculation time, since the digital signal processor we have used does not support floating-point operation. The variables d_{norm}, v_{norm}, t_{norm}, p_{norm}, and α_{norm} are normalization factors of the tabulated quantities inside the small parenthesis. The summations with respect to the suffix j and k are executed using floating-point 32-bit variables in order to minimize the numerical errors. The constant m in the formula of pressure tensor stand for the mass of ions (assuming protons) and electrons.

If there exists a counterstreaming flow, the resultant bulk flow velocity $\mathbf{V}$ will be small and we cannot recognize the existence of such counterstreaming

particles without dividing the azimuthal direction. Therefore we have calculated n and $n\mathbf{V}$ of ions and electrons (except solar wind ions), separately in 4 azimuthal sectors; sunward, anti-sunward, duskward, and dawnward. Energy steps can also be divided into two ranges, lower energy and higher energy, in calculating n and $n\mathbf{V}$ of ions and electrons. The energy boundary between the two energy ranges can be selected by command. We have set this energy boundary in order to eliminate the photoelectron contamination included in the electron velocity moments. The higher-order velocity moments $\mathbf{P}$ and $\mathbf{H}$ are calculated by using only the count rates of the higher-energy range. The calculated velocity moments are compressed from 32 bits to 8 bits by a special algorithm and transmitted to the ground every spin period (about 3 sec.).

B.1.2 Data Processing on the Ground

Some noise counts are included in the observed raw count rate data especially of the ion sensor, LEP-EAi. These noise counts are due to the electrical noise and/or generated by solar EUV photons. We have removed the effect of the noise count rate at a fixed level, which has been estimated from three-dimensional count rate data. We also have to correct the effects of time variation of the efficiency of the detector by the ground data processing.

After removing the effects of noise counts and correcting the effect of the efficiency variation, we have calculated fluid pressure tensor $\mathbf{Pf}$ and fluid

heat flux tensor **Hf** (or fluid heat flux vector **qf**) as follows,

$$Pf_{lm} = P_{lm} - nmV_lV_m \tag{B.24}$$

$$Hf_{lmn} = \frac{m}{2}H_{lmn} + nmV_lV_mV_n - \frac{1}{2}P_{lm}V_n \tag{B.25}$$

$$qf_l = \frac{m}{2}q_l + nmV^2V_l - P_{lm}V_m - \frac{1}{2}(P_{xx} + P_{yy} + P_{zz})V_l \tag{B.26}$$

where the suffix l, m, and n represent x, y, or z.

B.2 Evaluation of the Observed Velocity Moments

We have evaluated the accuracy of the onboard calculated velocity moments by comparison with the velocity moments calculated from three-dimensional count rate data obtained every four-spin period. The difference between these two velocity moments are summarized as follows.

1. We have used only 32-bit floating-point variables in calculating velocity moments from three-dimensional count rate data, while the cosine and sine tables and other constants have only 16-bit fixed-point values in the onboard velocity moment calculation.

2. Onboard velocity moments are calculated from the count rate data obtained during one spin period, while the velocity moments on the ground are calculated from the count rate data obtained during four-spin period. The result calculated on the ground has higher statistical accuracy especially when the count rate is low.

3. Onboard calculated velocity moments are compressed when they are transmitted to the ground, while the velocity moments calculated on the ground do not need such a procedure that reduces accuracy.

4. The noise reduction level is set at a certain fixed value for results of the onboard calculations, whereas it can be determined from the raw count data for the velocity moments calculated on the ground, as described in Section 4 of Chapter 2.

We can easily expect that the accuracy of the velocity moments calculated on the ground is much better than onboard calculated velocity moments. What we want to know is how much these two results agree and under what condition these two velocity moments become different.

In this appendix, we will present only the result of the comparison of velocity moments up to the second order, density, bulk velocity and pressure. We have made four-spin period average on the onboard calculated moments for the comparison.

Figure B.1 compares onboard calculated electron velocity moments and ion velocity moments calculated on the ground obtained on 13 January, 1994. The spacecraft was in the lobe or plasma sheet during the time period between 1100UT and 1500UT shown in Figure B.1. During this period, electrons were observed in the high-energy mode. The ion and electron density roughly corresponded with each other (see Panel (a)). Though three components of the electron bulk velocity were scattered, the average values agreed

roughly with those of the ion bulk velocity vector (see Panel (b)(c) and (d)). Therefore the onboard calculated electron velocity moments can be regarded as correct during the period shown in Figure B.1.

Figure B.2 compares onboard calculated ion velocity moments with those calculated on the ground obtained during the same period as Figure B.1. When ion density was larger than about 0.03 $/cm^3$, both of the ion densities agreed well (see Panel (a)). Three components of the bulk velocity vector also showed good agreement (see Panel (b)(c) and (d)). Some scattering data points may correspond to the data in low-density regions. The temperature data are scattered more than the lower-order velocity moments, however most of the data points show a reasonable agreement (see Panel (e) and (f)).

The format of Figure B.3 is the same as Figure B.1. The spacecraft was in the plasma sheet or lobe during the period shown in Figure B.3, between 1500UT and 1900UT on February 13, 1994. Electrons were observed in the low-energy mode during this period. Though density and bulk velocity roughly agreed with those of ions, there were periods when they showed big difference. Electron data of low energy steps in the low-energy mode were contaminated by photoelectrons. Though we set the energy boundary in order to remove the photoelectron contaminated data, some of them might still remain.

Figure B.4 shows electron and ion velocity moments in the magnetosheath observed on February 1, 1994. The energy sweeping mode of electrons was

high-energy mode. The electron density was much lower than ion density, since most of the electrons were under the observed energy range. Higher-order electron velocity moments might not be correct during this period, because onboard calculated electron density were used in calculation.

Figure B.5 compares onboard calculated ion velocity moments with those calculated on the ground observed in the magnetosheath. All ion velocity moments showed good correspondence in the sheath region.

Figure B.6 also shows electron and ion velocity moments in the magnetosheath. During the period shown in Figure B.6, the energy sweeping mode of electrons were low-energy mode. Electron density was much lower than ion density, though electron density showed the similar variation as the ion density variation. Since we set the energy boundary in order to remove photoelectrons in plasma sheet and lobe regions, the boundary was not suitable for sheath regions.

During the period shown in Figure B.7, the spacecraft was in the plasma sheet or lobe. Since cold dense plasma was observed in the lobe, the density in the plasma sheet was lower than the density in the lobe. Electron density was nearly the same as ion density between 1230UT and 1320UT, when the spacecraft was in the plasma sheet or lobe without cold dense plasma. However, onboard calculated electron density was much lower than ion density in the lobe region with cold dense plasma. Since the energy sweeping mode of electrons was high energy mode, most of the electrons were under the

observed energy range.

Figure B.8 compares ion velocity moments during the same period as Figure B.7. Density and velocity showed good coincidence. Temperature also showed good agreement when it was above about 20eV.

Figure B.9 compares electron and ion velocity moments when the spacecraft was in the lobe with cold dense plasma. The energy sweeping mode of electrons was low-energy mode. Though the difference between electron density and ion density was smaller than the previous case (Figure B.7). electron density was still smaller than ion density. Since we set the energy boundary to remove photoelectrons in the plasma sheet or lobe (without cold dense plasma), the boundary level was not proper for the cases when cold dense plasma was observed.

In summary, the onboard calculated ion density and ion bulk velocity vector are correct when the ion density is above $\sim 0.03\ /cm^3$. Onboard calculated temperature is also correct on the average, when the ion density is above $0.03\ /cm^3$ and the temperature is above $\sim$20eV, though it scatters more than the lower-order velocity moments, density and bulk velocity vector. As for the onboard calculated electron velocity moments, the onboard results are roughly the same as the ion density in the plasma sheet and lobe without cold dense plasma. However the onboard calculated electron density is much lower than the ion density when the spacecraft is in the sheath region or in the lobe region with cold dense plasma. This discrepancy is due

to the inappropriate selection of the energy boundary in these regions, since the energy boundary is usually set at an optimum level for measurement in the plasma sheet and lobe regions without cold dense plasma.

References

Akasofu, S.-I., The development of the auroral substorm, *Planet. Space Sci., 12*, 273, 1964

Angelopoulos, V., C. F. Kennel, F. V. Coroniti, W. C. Feldman, J. T. Gosling, M. G. Kivelson, R. J. Walker, C. T. Russel, Observations of a quasi-static plasma sheet boundary,*Geophys. Res. Lett., 20*, 2813, 1993

Ashour-Abdalla, M., J. Berchem, J. Büchner and L.M. Zelenyi, Large and small scale structures in the plasma sheet:A signature of chaotic motion and resonance effects, *Geophys. Res. Lett., 18*, 1603, 1991

Ashour-Abdalla, M., L.M. Zelenyi, J.M. Bosqued, and R.A. Kovrazhkin, Precipitation of fast ion beams from the plasma sheet boundary layer, *Geophys. Res. Lett., 19*, 617, 1992

Baumjohann, W., G. Pashmann, and H. Lühr, Characteristics of high-speed ion flows in the plasma sheet, *J. Geophys. Res., 95*, 3801, 1990

Birn, J., E. W. Hones, Jr., and K. Schindler, Field-aligned plasma flow in MHD simulations of magnetotail reconnection and the formation of boundary layers, *J. Geophys. Res., 91*, 11116, 1986

Bosqued, J.M., AUREOL-3 results on ion precipitation, *Phys. Scr., 18*, 158, 1987

Cattell, C. A., C. W. Carlson, W. Baumjohann, and H. Lühr, The MHD structure of the plasmasheet boundary: (1) tangential momentum balance and consistency with slow mode shocks, *Geophys. Res. Lett., 19*, 2083, 1992

Coroniti, F. V., Laminar wave-train structure of collisionless magnetic slow mode shocks, *Nucl. Fusion, 11*, 261, 1971

DeCoster, R. J., and L. A. Frank, Observations pertaining to the dynamics of the plasma sheet, *J. Geophys. Res., 84*, 5099, 1979

Dungey, J. W., Interplanetary magnetic field and the auroral zones, *Phys. Rev. Lett., 6*, 47, 1961

Eastman, T. E., L. A. Frank, W. K. Peterson, and W. Lennartsson, The plasma sheet boundary layer, *J. Geophys. Res., 89*, 1553, 1984

Eastman, T. E., L. A. Frank, and C. Y. Huang, The boundary layers as the primary transport regions of the Earth's magnetotail, *J. Geophys. Res., 90*, 9541, 1985

Eastman, T. E., R. J. DeCoster, and L. A. Frank, Velocity distributions of ion beams in the plasma sheet boundary layer, *Geophys. Mon.#38*, ed by T. Chang, 117, American Geophysical Union, Washington, D. C., 1986

Feldman, W. C., S. J. Schwaltz, S. J. Bame, D. N. Baker, J. Birn, J. T. Gosling, E. W. Hones, Jr., D. J. McComas, J. A. Slavin, E. J. Smith, and R. D. Zwickl, Evidence for slow-mode shocks in the deep geomagnetic tail, *Geophys. Res. Lett., 11*, 599, 1984a

Feldman, W. C., D. N. Baker, S. J. Bame, J. Birn, E. W. Hones, Jr., S. J. Schwaltz, and R. L. Tokar, Power dissipation at slow-mode shocks in the distant geomagnetic tail, *Geophys. Res. Lett., 11*, 1058, 1984b

Feldman, W. C., R. L. Tokar, J. Birn, E. W. Hones, Jr., S. J. Bame, and C. T. Russel, Structure of a slow mode shock observed in the plasma sheet boundary layer, *J. Geophys. Res., 92*, 83, 1987

Feldman, W. C., D. N. Baker, S. J. Bame, J. Birn, J. T. Gosling, E. W. Hones, Jr., and S. J. Schwartz, Slow-mode shocks: A semipermanent feature of the distant geomagnetic tail, *J. Geophys. Res., 90*, 233, 1985

Forbes, T. G., E. W. Hones, Jr., S. J. Bame, J. R. Asbridge, G. Paschmann, N. Sckopke, and C. T. Russel, Evidence for the tailward retreat of a magnetic neutral line in the magnetotail during substorm recovery, *Geophys. Res. Lett, 8*, 261, 1981a

Forbes, T. G., E. W. Hones, Jr., S. J. Bame, J. R. Asbridge, G. Paschmann, N. Scopke, and C. T. Russel, Substorm-related plasma sheet motions as determined from differential timing of plasma changes at the isee satellites, *J. Geophys. Res., 86*, 3459, 1981b

Hesse, M. and J. Birn, Plasmoid evolution in an extended magnetotail, *J. Geophys. Res., 96*, 5683, 1991

Hill, T. W., Magnetic merging in a collisionless plasma, *J. Geophys. Res., 80*, 4689, 1975

Hill, T. W., and P. H. Reiff, Evidence of magnetospheric cusp proton acceleration by magnetic merging at the magnetopause, *J. Geophys. Res., 82*, 3623, 1977

Hill, T. W., Solar-wind magnetosphere coupling, *Solar-Terrestrial Physics*, ed by R.L. Carovillano and J.M. Forbes, 261, D. Reidel Publishing Company, 1983

Hirahara, M., T. Mukai, Satellite borne energetic ion mass spectrometer for three-dimensional measurement of velocity distribution, *Rev. Sci. Instrum., 64*, 406, 1993

Hirahara, M., T. Mukai, S. Machida, Y. Saito, T. Terasawa, M. Nakamura, A. Nishida, S. Kokubun, and T. Yamamoto, Acceleration and heating of cold ion beam in the plasma sheet boundary layer observed with GEOTAIL, *Geophys. Res. Lett., in press*, 1994

Hones, E. W., Jr., Substorm Processes in the Magnetotail: Comments on 'On Hot Tenuous Plasmas, Fireballs, and Boundary Layers in the Earth's Magnetotail', *J. Geophys. Res., 82*, 5633, 1977

Hones, E., W., Jr., G. Paschmann, S. J. Bame, J. R. Asbridge, N. Scopke and K. Schindler, Vortices in Magnetospheric Plasma Flow, *Geophys. Res. Lett., 5*, 1059, 1978

Hones, E. W. Jr., Plasma flow in the magnetotail and its implications for substorm theories, *Dynamics of the Magnetosphere*, ed by S.-I. Akasofu, 545, D. Reidel Publishing Company, 1979

Hones, E. W., Jr., J. Birn, S. J. Bame, J. R. Asbridge, G. Paschmann, N. Scopke and G. Haerendel, Further Determination of the Characteristics of Magnetospheric Plasma Vortices with Isee 1 and 2, *J. Geophys. Res., 86*, 814, 1981

Hones, E., W., Jr., J. Birn, S. J. Bame, C. T. Russel, New Observations of Plasma Vortices and Insights into Their Interpretation, *Geophys. Res. Lett., 10*, 674, 1983

Hones, E. W., Jr., T. Pytte, H. I. West, Jr., Association of geomagnetic activity with plasma sheet thinning and expansion : a statistical study, *J. Geophys. Res., 89*, 5471,1984

Kokubun, S., T. Yamamoto, M. H. Acuna, K. Hayashi, K. Shiokawa, and H. Kawano, The GEOTAIL magnetic field experiment,*J. Geomag. Geoelectr., 46*, 7, 1994

Kovrazkhin, R.A., J.M. Bosqued, L.M. Zelenyi, and N.V. Jorjio, Observation of evidence of reconnection and plasma acceleration at a distance of about 5×10^5 km in the tail of the earth's magnetosphere, *JETP Lett., Engl. Transl., 45(8)*, 479, 1987

Lui, A.T.Y., T.E. Eastman, D.J. Williams, and L.A. Frank, Observations of ion streaming during substorms, *J. Geophys. Res., 88*, 7753, 1983

Lyons, L.R., and T.W. Speiser, Evidence for current sheet acceleration in the geomagnetic tail, *J. Geophys. Res., 87*, 2276, 1982

Matsumoto, H., I. Nagano, R. R. Anderson, H. Kojima, K. Hashimoto, M. Tsutsui, T. Okada, I. Kimura, Y. Omura, and M. Okada, *J. Geomag. Geoelectr., 46*, 59, 1994

Mukai, T., and W. Miyake, Transmission characteristics and fringing field effect of a 270° spherical electrostatic analyzer, *Rev. Sci. Instrum., 57*, 49, 1986.

Mukai, T., N. Kaya, E. Sagawa, M. Hirahara, W. Miyake, T. Obara, H. Miyaoka, S. Machida, H. Yamaguchi, M. Ejiri, H. Matsumoto, and T. Itoh, Low energy charged particle observations in the "auroral" magnetosphere:first results from Akebono(EXOS-D) satellite, *J. Geomag. Geoelectr., 42*, 479, 1990

Mukai, T., M. Hirahara, S. Machida, Y. Saito, T. Terasawa, and A. Nishida, GEOTAIL Observation of Cold Ion Streams in the Medium Distance Magnetotail Lobe in the Cource of a Substorm, *Geophys. Res. Lett.*, *21*,1023, 1994a

Mukai, T., S. Machida, Y. Saito, M. Hirahara, T. Terasawa, N. Kaya, T. Obara, M. Ejiri, and A. Nishida, The Low Energy Particle (LEP) experiment onboard the GEOTAIL satellite, *J. Geomag. Geoelectr.*, *46*, 669, 1994b

Nakamura, M., G. Paschmann, W. Baumjohann, and N. Sckopke, Ion distributions and flows in and near the plasma sheet boundary layer, *J. Geophys. Res.*, *97*, 1449, 1992

Omidi, N., D. Winske, Kinetic Structure of Slow Shocks: Effects of the Electromagnetic Ion/Ion Cyclotron Instability, *J. Geophys. Res.*, *97*, 14801, 1992

Onsager, T. G., M. F. Thomsen, R. C. Elphic, and J. T. Gosling, Model of electron and ion distributions in the plasma sheet boundary layer, *J. Geophys. Res.*, *96*, 20992, 1991

Petschek, H. E., Magnetic field annihilation, *AAS-NASA Symposium on the Physics of Solar Flares, NASA Spec. Publ. SP-50*, 425, 1964

Pilipp, W. G., and G. Morfill, The formation of the plasma sheet resulting from plasma mantle dynamics, *J. Geophys. Res., 83*, 5670, 1978

Saito, Y., T. Mukai, M. Hirahara, S. Machida, A. Nishida, T. Terasawa, S. Kokubun, and T. Yamamoto, GEOTAIL observation of ring-shaped ion distribution functions in the plasma sheet-lobe boundary, *Geophys. Res. Lett., in press*, 1994

Sanderson, T. R., P. W. Daly, K. P. Wenzel, E. W. Hones, Jr. and S. J. Bame, Energetic Ion Observations of a Large Scale Vortex in the Distant Geotail, *Geophys. Res. Lett., 11*, 1094, 1984

Saunders, M. A., D. J. Southwood, E. W. Hones, Jr. and C. T. Russel, A Hydromagnetic Vortex Seen by ISEE-1 and 2, *J. Atm. Terr. Phys., 43*, 927, 1981

Saunders, M. A., D. J. Southwood, T. A. Fritz and E. W. Hones, Jr., Hydromagnetic Vortices-1. The 11 December 1977 Event, *Planet. Space Sci., 31*, 1099, 1983a

Saunders, M. A., D. J. Southwood and E. W. Hones, Jr., Hydromagnetic Vortices-2. Further Dawnside Events, *Planet. Space Sci., 31*, 1117, 1983b

Sato, T., Strong plasma acceleration by slow shocks resulting from magnetic reconnection, *J. Geophys. Res., 84*, 7177, 1979

Scarf, F. L., F. V. Coroniti, C. F. Kennel, E. J. Smith, J. A. Slavin, B. T. Tsurutani, S. J. Bame, and W. C. Feldman, Plasma wave spectra near slow mode shocks in the distant magnetotail, *Geophys. Res. Lett., 11*, 1050, 1984

Schwartz, S. J., M. F. Thomsen, W. C. Feldman, and F. T. Douglas, Electron dynamics and potential jump across slow mode shocks, *J. Geophys. Res., 92*, 3165, 1987

Sholer, M., and D. Roth, A simulation study on reconnection and small-scale plasmoid formation, *J. Geophys. Res., 92*, 3223, 1987

Smith, E. J., J. A. Slavin, B. T. Tsurutani, W. C. Feldman, and S. J. Bame, Slow mode shocks in the Earth's magneto tail: ISEE-3, *Geophys. Res. Lett., 11*, 1054, 1984

Southwood, D. J. and M. A. Saunders, Curvature Coupling of Slow and Alfvén MHD Waves in a Magnetotail Field Configuration, *Planet. Space Sci., 33*, 127, 1985

Speiser, T. W., Particle trajectories in model current sheets, 1, analytical solutions, *J. Geophys. Res., 70*, 4219, 1965

Speiser, T. W., Particle trajectories in model current sheets, 2, applications to auroras using a geomagnetic tail model, *J. Geophys. Res., 72*, 3919, 1967

Speiser, T. W., and L. R. Lyons, Comparison of an analytical approximation for particle motion in a current sheet with precise numerical calculations, *J. Geophys. Res., 89*, 147, 1984

Swift, D. W., On the structure of the magnetic slow switch-off shock, *J. Geophys. Res., 88*, 5685, 1983

Takahashi, K., and E.W. Hones, Jr., ISEE 1 and 2 Observations of Ion Distributions at the Plasma Sheet-Tail Lobe Boundary, *J. Geophys. Res., 93*, 8558, 1988

Tsuruda, K., H. Hayakawa, M. Nakamura, T. Okada, A. Matsuoka, F. S. Mozer, and R. Schmidt, Electric Field Measurements on the GEOTAIL Satellite, *J. Geomag. Geoelectr., 46*, 693, 1994

Ugai, M., Computer studies on the fast reconnection mechanism in a sheared field geometry, *Phys. Fluids B, 5*, 3021, 1993

Vasyliunas, V. M., Theoretical Models of Magnetic Field Line Merging, 1, *Rev. Geophysics. Space Phys., 13*, 303, 1975

Zelenyi, L.M., R.A. Kovrazkhin, and J.M., Bosqued, Velocity-Dispersed Ion Beams in the Nightside Auroral Zone: AUREOL 3 Observations, *J. Geophys. Res., 95*, 12119, 1990

Table Captions

schematic figure of satellite position with respect to the X-type neutral line are shown. The downstream parameters of the shock are the observed value (left side value), the calculated value (in the parenthesis), and the difference between calculated and observed values (right side value).

Table 5.2 Upstream and downstream shock parameters of a shock observed on the front side of a plasmiod observed on 18 September, 1993. The format is the same as Table 5.1.

Table 5.3 Ratio of the slow-mode shocks and other 8 types of plasma sheet-lobe boundaries observed between 14 September, 1993 and 16 February, 1994.

Table 6.1 Characteristics of the ring distributed ions and high-energy beam ions for 11 examples observed between September 14, 1993 and October 15, 1993. From left to right, the flow direction of the high-energy beam ions, the angle δ between the normal direction of the ring distribution and the magnetic field direction, the flow velocity of the center of the ring (tailward) along the magnetic field, the radius of the ring in the velocity space, density of the ring ions, density of the high-energy beam ions, velocity of the high-energy beam ions, date, time, and the position of the spacecraft in the GSM coordinate system when the ring ion was observed are shown.

Figure Captions

Figure 1.1 Magnetic and plasma structure around the Earth (adapted from Pilipp and Morfill [1978], slightly modified).

Figure 1.2 The reconnection model of the Earth's magnetosphere proposed by Dungey [1961] (adapted from Hill [1983]).

Figure 1.3 Plasma sheet configuration changes during a substorm. Magnetic field lines 1, 2, 3, 4 are in the plasma sheet (fine hatching), field line 5 bounds the pre-substorm plasma sheet and field lines 6 and 7 are initially in the tail lobe. N marks the location of a distant neutral line that terminates the closed pre-substorm plasma sheet. N$\prime$ marks the "substorm neutral line" that appears at substorm onset. Coarse shading represents lobe plasma that has come through the merging region and has been accelerated. The dot represents an observing satellite at $X_{SM} \sim -30$Re. White arrows indicate directions and approximate relative magnitude of plasma flow (adapted from Hones [1979]).

Figure 1.4 Ion and electron motion in a model current sheet. The current sheet has a small magnetic field, B_Z, normal to the sheet and a guiding center drift along the $E \times B_Z$ direction adds to the particle motions which involve a meandering about the neutral sheet due to the changing sign of B_x and the associated Lorentz force. During its simultaneous displacement along the direction of the applied electric field, the par-

Figure 3.3 Relation between the bulk energy and temperature of shifted-Maxwellians fitted to 50 distribution functions of the ion beams.

Figure 3.4 Relation between the bulk energy and the width of the invariant latitude (where the ion beam was observed) divided by the square root of the temperature. The curves in the figure obey the relation $\Delta I/\sqrt{E_{th}} \times E_0 = \text{const}$. The constant values are 4, 8, 12, and 16 (deg $\cdot$ keV$^{\frac{1}{2}}$), respectively.

Figure 4.1 E-t diagrams of electrons (a) and ions (b) and velocity moments of electrons (small dots) and ions (large dots) between 1300 UT and 1700 UT calculated from three-dimensional data of 13.1s time resolution. Since we changed the energy range of the electrons at 1516 UT (indicated by an arrow in panel (a)), the left-hand side scale should be used before this time, and the right-hand side scale should be used thereafter. The panel (c) is the density (cm^{-3}), the panel (d) is the magnitude of the bulk velocity (km sec^{-1}), and the panels (e) and (f) are the polar and azimuthal angles of the bulk flow velocity vector in the GSE polar coordinate system. Two 40-minute periods 'period 1' and 'period 2' are indicated by arrows.

Figure 4.2 Panels (a) (b) (c) are the spectra of the motion of the angles between the ion bulk flow direction and GSE x, y, z axes $(\theta_x, \theta_y, \theta_z)$ during the time interval between 1440 UT and 1632 UT. The spectra

are normalized by the highest power in each spectra. Panels (d) (e) (f) (g) are the dynamic spectra of the angles $\theta_x, \theta_y, \theta_z$ and the magnitude of the bulk velocity during the time interval between 1428 UT and 1634 UT. The spectra are calculated every 2 minutes using the data between 1400 UT and 1700 UT with the time window of 3354 seconds. All the spectra are normalized by the highest power in each time.

Figure 4.3 Rapidly varying component (2-minute running averaged data – 20-minute running averaged data) of the bulk flow velocity vector projected on GSE x-y, x-z and y-z planes during the time interval between 1400 UT and 1700 UT. Two 40-minute periods 'period 1' and 'period 2' are indicated by arrows.

Figure 4.4 Slowly varying component of the bulk flow velocity vector between 1606 UT and 1646 UT which is obtained by conducting 20 minutes running average over the calculated velocity moments (solid line). The top panel is the magnitude of the vector (km $\sec^{-1}$). The second and third panels are the polar and azimuthal angles of the vector in the GSE polar coordinate system. The direction of the magnetic field estimated from the anisotropy of the electron temperature tensor is also plotted in these panels (dot).

Figure 4.5 An example of the gyrotropic electron distribution function and the estimated magnetic field direction.

Figure 4.6 Rapidly varying component of the bulk flow velocity vector between 1606 UT and 1646 UT (panels (a)(b)(c)) which is obtained by subtracting 20 minutes running averaged velocity moments from 2 minutes running averaged velocity moments. The panel (a) is the magnitude of the vector (km sec^{-1}). The panels (b) and (c) are the polar and azimuthal angles of the vector in the GSE polar coordinate system. Panel (d) is the direction of the rotation axis, p_p, defined in the text. Panel (e) is the angle between the rotation axis and the estimated magnetic field direction. The bottom panel (f) is the angle between the rotation axis projected on the GSE y-z plane and z direction.

Figure 4.7 Slowly varying component of the bulk flow velocity vector between 1445 UT and 1525 UT which is obtained by conducting 14 minutes running average over the calculated velocity moments (solid line). The top panel is the magnitude of the vector (km sec^{-1}). The second and third panels are the polar and azimuthal angles of the vector in the GSE polar coordinate system. The direction of the magnetic field estimated from the anisotropy of the electron temperature tensor is also plotted in these panels (dot).

Figure 4.8 Rapidly varying component of the bulk flow velocity vector between 1445 UT and 1525 UT (panels (a)(b)(c)) which is obtained by subtracting 14 minutes running averaged velocity moments from 2 minutes running averaged velocity moments. The panel (a) is the magni-

tude of the vector (km sec^{-1}). The panels (b) and (c) are the polar and azimuthal angles of the vector in the GSE polar coordinate system. Panel (d) is the angle between the rotation axis and the estimated magnetic field direction.

Figure 4.9 Schematic diagrams of the model which explains the variations of the bulk flow direction during the time interval between 1445 UT and 1525 UT.

Figure 5.1 The definition of upstream (lobe) and downstream (plasma sheet) shock parameters in the normal incidence frame (NIF).

Figure 5.2 Magnetic field data and plasma velocity moments obtained on 14 January, 1994. From top to bottom, total magnetic field, polar and azimuthal angles of the magnetic field direction in the GSE polar coordinate system, ion (thick line) and electron (thin line) density, magnitude of ion bulk velocity, polar and azimuthal angles of the ion bulk flow velocity vector in the GSE coordinate system, and ion(thick line) and electron (thin line) temperature are shown. The upstream region and downstream region are indicated in the figure.

Figure 5.3 Electron distribution function parallel to the magnetic field, observed in the upstream (lobe) region, downstream (plasma sheet) region, and between these two regions, corresponding to the slow-mode shock shown in Figure 5.2.

Figure 5.4 (a) E-t diagram of ions obtained on 14 January, 1994. The upstream and downstream regions are shown. Between the upstream and downstream regions, accelerated cold ions are observed (indicated by arrows). (b)-(e) E-t diagrams of ions flowing dawnward, tailward, duskward, and earthward during the same time interval as Panel (a).

Figure 5.5 (a) E-t diagram of ions obtained on 17 January, 1994. (b) Pitch angle distribution of ions in the de-Hoffmann Teller frame during the same period shown in Panel (a). The phase space density over all the observed energy range is shown by color-coded intensity for every 18 degrees with respect to the magnetic field direction. Backstreaming ions are indicated by an arrow.

Figure 5.6 Magnetic field data and plasma velocity moments obtained on 18 September, 1994. The format is the same as Figure 5.2 except that the scales are different.

Figure 5.7 E-t diagram of ions obtained on 18 September, 1994. The upstream region and downstream region are shown in the figure.

Figure 5.8 Orbit of GEOTAIL satellite in the GSE coordinate system between 14 September, 1993 and 16 February, 1994. Small dots show the position of the satellite at 0000UT every day. Large dots show the first day in each month. The periods when plasma-sheet lobe crossings are observed are indicated by thick line in the orbit projected on GSE X-Y

plane.

Figure 5.9 Distribution of slow-mode shocks and the other 8 types of plasma sheet-lobe boundaries with respect to the distance X in the GSE coordinate system. The number of the boundaries are shown every 20Re in Panel (a), and the normalized occurrence of each category in each distance is shown in Panel (b).

Figure 5.10 Distribution of slow-mode shocks and the other 8 types of plasma sheet-lobe boundaries with respect to the Kp index. The number of the boundaries are shown in Panel (a), and the normalized occurrence of each category is shown in Panel (b). Panel (c) shows the number of the boundary crossings normalized by the occurrence rate of each Kp values during observation.

Figure 5.11 Location of the expected X-type neutral line with respect to the satellite, whether it is in the earthward or tailward of the spacecraft for the 32 slow-shock boundaries. The direction is shown every 20Re in GSE-X distance.

Figure 5.12 "Heart" shaped structure of a plasmoid predicted by a numerical simulation (by courtesy of Dr. K. Maezawa).

Figure 6.1 Cross sections of the ring-shaped ion distribution function in the velocity space observed at 1603:48 UT on September 14, 1993.

Schematic figures of these distributions are drawn above the three panels, and the look direction is shown in each figure by an arrow.

Figure 6.2 E-t diagrams of electrons (a) and ions (b) and the magnetic field data in the GSM polar coordinate system (c)(d)(e) between 1520UT and 1640UT on September 14, 1993. The time when ring-shaped ion distribution function was observed is indicated by an arrow.

Figure 6.3 Ion and electron velocity moments during the time interval between 1520UT and 1640UT on September 14, 1993. Panel (a) is the ion density (cm^{-3}), panel (b) is the magnitude of the ion bulk flow velocity (km sec^{-1}), and panels (c) and (d) are the polar and azimuthal angles of the ion bulk flow velocity vector in the GSM polar coordinate system. Panel (e) is the ion (solid line) and electron (dotted line) temperature deduced from GSE y direction. The left-side scale is for ions and the right-side scale is for electrons. The time when ring-shaped ion distribution function was observed is indicated by an arrow.

Figure A.1 A trajectory of a charged particle in the orbit plane on a cross section of a spherical section analyzer.

Figure A.2 The definition of the spacecraft coordinate system.

Figure A.3 The definition of the projection angles of a particle at the exit edge of the analyzer plates.

Figure A.4 An orbit of a particle projected on the inner sphere.

Figure A.5 The definition of the projection angles of a particle at the exit edge of the analyzer plates.

Figures A.6-A.9 Developments of the inner sphere with a projected orbit of a particle.

Figure A.10 A schematic diagram of the calibration system.

Figures A.11, A.12 Experimentally obtained E-α contours of EAe CH1 and CH4.

Figures A.13, A.14 Experimentally obtained E-α contours of EAi CH1 and CH4.

Figures A.15, A.16 Experimentally obtained E-α contours of SW CH1 and CH4.

Figure B.1 Onboard calculated electron velocity moments and ion velocity moments observed in the plasma sheet or lobe on 13 January, 1994. During the time interval shown in the figure, the energy sweeping mode of electrons were high-energy mode. Electron data are plotted with small dots and ion data are plotted with large dots. From top to bottom, (a) density, (b)-(d) bulk velocity vector in the space craft coordinate system, (e)(f) two components (T_{yy} and T_{zz}) of the temperature tensor are plotted.

Figure B.2 Scatter plots between the onboard calculated ion velocity moments and the ion velocity moments calculated on the ground observed in the plasma sheet or lobe on 13 January, 1994. From top to bottom, (a) density, (b)-(d) bulk velocity vector in the space craft coordinate system, (e)(f) two components (T_{yy} and T_{zz}) of the temperature tensor are plotted.

Figure B.3 Onboard calculated electron velocity moments and ion velocity moments observed in the plasma sheet or lobe on 13 February, 1994. The format is the same as Figure B.1. During the time interval shown in the figure, the energy sweeping mode of electrons was low-energy mode.

Figure B.4 Onboard calculated electron velocity moments and ion velocity moments observed in the magnetosheath on 1 February, 1994. The format is the same as Figure B.1. During the time interval shown in the figure, the energy sweeping mode of electrons was high-energy mode.

Figure B.5 Scatter plots between the onboard calculated ion velocity moments and the ion velocity moments calculated on the ground observed in the magnetosheath on 1 February, 1994. The format is the same as Figure B.2.

Figure B.6 Onboard calculated electron velocity moments and ion velocity moments observed in the magnetosheath on 31 October, 1993. The format is the same as Figure B.1. During the time interval shown in the figure, the energy sweeping mode of electrons was low-energy mode.

Figure B.7 Onboard calculated electron velocity moments and ion velocity moments observed in the plasma sheet or lobe with cold high density plasma on 10 January, 1994. The format is the same as Figure B.1. During the time interval shown in the figure, the energy sweeping mode of electrons was high-energy mode.

Figure B.8 Scatter plots between the onboard calculated ion velocity moments and the ion velocity moments calculated on the ground observed in the plasma sheet or lobe with cold high density plasma on 10 January, 1994. The format is the same as Figure B.2.

Figure B.9 Onboard calculated electron velocity moments and ion velocity moments observed in the plasma sheet or lobe with cold high density plasma on 19 October, 1993. The format is the same as Figure B.1. During the time interval shown in the figure, the energy sweeping mode of electrons was low-energy mode.

Table 2.1 Scientific instruments onboard the GEOTAIL spacecraft.

Item	Instrument	Principal Investigator	Co-Investigator
Electric Field (EFD)	Spherical Probe Wire Antenna Electron Boomerang	K. Tsuruda	F.S. Mozer
Magnetic Field (MGF)	Fluxgate Search Coil	S. Kokubun	R.L. Lepping M. Acuna
Plasma (LEP)	Ion/Ele. Energy Analyzer Solar Wind Ion Analyzer Ion Mass Spectrometer	T. Mukai	
Plasma (CPI)	Hot Plasma Analyzer Solar Wind Ion Analyzer Ion Composition Analyzer	L.A. Frank	
Energetic Particles (HEP)	Low Energy Detector Burst Detector Isotope Telescopes	T. Doke	B. Wilken
Energetic Particles (EPIC)	Supra-Thermal Ion -Composition Spectrometer Ion Composition Subsystem	D.J. Williams	
Plasma Waves (PWI)	Multi-Channel Analyzer Sweep Frequency Analyzer Wave Form Capture (both E and B fields)	H. Matsumoto	R. Anderson

Table 2.2 Basic parameters of the instrument performance for the EAe and EAi sensors.

EA-e				
CHANNEL (DIRECTION)	$\Delta\alpha$ (FWHM)	$\Delta\theta$ (FWHM)	$\Delta\delta$ (FWHM)	g-factor ($cm^2 \cdot str \cdot eV/eV$)
CH1 ($-66.0°$)	8.4°	10.2°	14.0 %	1.68×10^{-5}
CH2 ($-44.4°$)	9.1°	8.6°	12.9 %	2.74×10^{-5}
CH3 ($-22.1°$)	9.1°	6.4°	12.6 %	3.58×10^{-5}
CH4 (0.0°)	9.4°	5.9°	12.4 %	4.08×10^{-5}
CH5 (22.0°)	9.0°	6.1°	12.5 %	3.93×10^{-5}
CH6 (44.2°)	9.5°	8.1°	12.6 %	3.08×10^{-5}
CH7 (65.7°)	8.4°	10.4°	13.6 %	1.80×10^{-5}

EA-i				
CHANNEL (DIRECTION)	$\Delta\alpha$ (FWHM)	$\Delta\theta$ (FWHM)	$\Delta\delta$ (FWHM)	g-factor ($cm^2 \cdot str \cdot eV/eV$)
CH1 ($-65.5°$)	6.8°	12.5°	15.2 %	6.74×10^{-4}
CH2 ($-44.9°$)	10.1°	7.9°	12.8 %	1.28×10^{-3}
CH3 ($-22.2°$)	10.3°	6.9°	11.7 %	1.45×10^{-3}
CH4 (0.0°)	10.2°	6.9°	11.6 %	1.51×10^{-3}
CH5 (22.3°)	10.1°	6.9°	11.7 %	1.44×10^{-3}
CH6 (44.7°)	10.4°	7.9°	12.4 %	1.21×10^{-3}
CH7 (65.6°)	6.7°	12.5°	15.0 %	6.10×10^{-4}

Table 2.3 Energy bins of EA-e.

	EA-e RAM A			EA-e RAM B		
STEP	E_0 (eV)	E_h (eV)	E_l (eV)	E_0 (eV)	E_h (eV)	E_l (eV)
0	3.815×10^4	4.163×10^4	3.488×10^4	7.621×10^3	8.491×10^3	6.813×10^3
1	3.197×10^4	3.488×10^4	2.922×10^4	6.115×10^3	6.813×10^3	5.466×10^3
2	2.678×10^4	2.922×10^4	2.448×10^4	4.906×10^3	5.466×10^3	4.386×10^3
3	2.244×10^4	2.448×10^4	2.051×10^4	3.937×10^3	4.386×10^3	3.519×10^3
4	1.880×10^4	2.051×10^4	1.719×10^4	3.159×10^3	3.519×10^3	2.824×10^3
5	1.575×10^4	1.719×10^4	1.440×10^4	2.535×10^3	2.824×10^3	2.266×10^3
6	1.320×10^4	1.440×10^4	1.207×10^4	2.034×10^3	2.266×10^3	1.818×10^3
7	1.106×10^4	1.207×10^4	1.011×10^4	1.632×10^3	1.818×10^3	1.459×10^3
8	9.266×10^3	1.011×10^4	8.471×10^3	1.309×10^3	1.459×10^3	1.170×10^3
9	7.765×10^3	8.471×10^3	7.098×10^3	1.051×10^3	1.170×10^3	9.392×10^2
10	6.506×10^3	7.098×10^3	5.948×10^3	8.430×10^2	9.392×10^2	7.536×10^2
11	5.452×10^3	5.948×10^3	4.984×10^3	6.764×10^2	7.536×10^2	6.047×10^2
12	4.568×10^3	4.984×10^3	4.177×10^3	5.427×10^2	6.047×10^2	4.852×10^2
13	3.828×10^3	4.177×10^3	3.500×10^3	4.355×10^2	4.852×10^2	3.893×10^2
14	3.208×10^3	3.500×10^3	2.933×10^3	3.494×10^2	3.893×10^2	3.124×10^2
15	2.689×10^3	2.933×10^3	2.458×10^3	2.804×10^2	3.124×10^2	2.506×10^2
16	2.253×10^3	2.458×10^3	2.060×10^3	2.250×10^2	2.506×10^2	2.011×10^2
17	1.888×10^3	2.060×10^3	1.726×10^3	1.805×10^2	2.011×10^2	1.614×10^2
18	1.582×10^3	1.726×10^3	1.447×10^3	1.448×10^2	1.614×10^2	1.295×10^2
19	1.326×10^3	1.447×10^3	1.212×10^3	1.162×10^2	1.295×10^2	1.039×10^2
20	1.111×10^3	1.212×10^3	1.016×10^3	9.325×10	1.039×10^2	8.336×10
21	9.313×10^2	1.016×10^3	8.515×10^2	7.482×10	8.336×10	6.689×10
22	7.806×10^2	8.515×10^2	7.137×10^2	6.004×10	6.689×10	5.367×10
23	6.542×10^2	7.137×10^2	5.981×10^2	4.817×10	5.367×10	4.306×10
24	5.199×10^2	5.981×10^2	4.853×10^2	3.865×10	4.306×10	3.455×10
25	4.518×10^2	4.853×10^2	4.172×10^2	3.101×10	3.455×10	2.772×10
26	3.838×10^2	4.172×10^2	3.491×10^2	2.488×10	2.772×10	2.225×10
27	3.157×10^2	3.491×10^2	2.810×10^2	1.997×10	2.225×10	1.785×10
28	2.477×10^2	2.810×10^2	2.130×10^2	1.602×10	1.785×10	1.432×10
29	1.754×10^2	2.130×10^2	1.343×10^2	1.286×10	1.432×10	1.149×10
30	9.320×10	1.343×10^2	7.660×10	1.031×10	1.149×10	9.221
31	6.000×10	7.660×10	4.340×10	8.276	9.221	7.399

Note: E_0 is the center energy of each bin. E_h and E_l are higher and lower boundaries of each bin.

Table 2.4 Energy bins of EA-i.

	EA-i RAM A			EA-i RAM B		
STEP	E_0 (eV)	E_h (eV)	E_l (eV)	E_0 (eV)	E_h (eV)	E_l (eV)
0	3.948×10^4	4.415×10^4	3.689×10^4	4.298×10^4	4.447×10^4	4.152×10^4
1	3.299×10^4	3.689×10^4	3.082×10^4	4.012×10^4	4.152×10^4	3.876×10^4
2	2.756×10^4	3.082×10^4	2.575×10^4	3.746×10^4	3.876×10^4	3.618×10^4
3	2.303×10^4	2.575×10^4	2.151×10^4	3.497×10^4	3.618×10^4	3.378×10^4
4	1.924×10^4	2.151×10^4	1.797×10^4	3.264×10^4	3.378×10^4	3.153×10^4
5	1.607×10^4	1.797×10^4	1.502×10^4	3.047×10^4	3.153×10^4	2.944×10^4
6	1.343×10^4	1.502×10^4	1.255×10^4	2.845×10^4	2.944×10^4	2.748×10^4
7	1.122×10^4	1.255×10^4	1.048×10^4	2.656×10^4	2.748×10^4	2.566×10^4
8	9.374×10^3	1.048×10^4	8.758×10^3	2.479×10^4	2.566×10^4	2.395×10^4
9	7.832×10^3	8.758×10^3	7.317×10^3	2.315×10^4	2.395×10^4	2.236×10^4
10	6.543×10^3	7.317×10^3	6.113×10^3	2.161×10^4	2.236×10^4	2.087×10^4
11	5.467×10^3	6.113×10^3	5.108×10^3	2.017×10^4	2.087×10^4	1.949×10^4
12	4.567×10^3	5.108×10^3	4.267×10^3	1.883×10^4	1.949×10^2	1.819×10^4
13	3.816×10^3	4.267×10^3	3.565×10^3	1.758×10^4	1.819×10^4	1.698×10^4
14	3.188×10^3	3.565×10^3	2.979×10^3	1.641×10^4	1.698×10^4	1.586×10^4
15	2.664×10^3	2.979×10^3	2.489×10^3	1.532×10^4	1.586×10^4	1.480×10^4
16	2.226×10^3	2.489×10^3	2.079×10^3	1.430×10^4	1.480×10^4	1.382×10^4
17	1.859×10^3	2.079×10^3	1.737×10^3	1.335×10^4	1.382×10^4	1.290×10^4
18	1.554×10^3	1.737×10^3	1.451×10^3	1.247×10^4	1.290×10^4	1.204×10^4
19	1.298×10^3	1.451×10^3	1.213×10^3	1.164×10^4	1.204×10^4	1.124×10^4
20	1.084×10^3	1.213×10^3	1.013×10^3	1.087×10^4	1.124×10^4	1.050×10^4
21	9.061×10^2	1.013×10^3	8.465×10^2	1.014×10^4	1.050×10^4	9.799×10^3
22	7.570×10^2	8.465×10^2	7.073×10^2	9.470×10^3	9.799×10^3	9.148×10^3
23	6.325×10^2	7.073×10^2	5.909×10^2	8.841×10^3	9.148×10^3	8.540×10^3
24	5.681×10^2	5.909×10^2	5.276×10^2	8.254×10^3	8.540×10^3	7.973×10^3
25	4.872×10^2	5.276×10^2	4.467×10^2	7.705×10^3	7.973×10^3	7.443×10^3
26	4.062×10^2	4.467×10^2	3.658×10^2	7.193×10^3	7.443×10^3	6.949×10^3
27	3.253×10^2	3.658×10^2	2.848×10^2	6.716×10^3	6.949×10^3	6.487×10^3
28	2.444×10^2	2.848×10^2	2.039×10^2	6.270×10^3	6.487×10^3	6.057×10^3
29	1.634×10^2	2.039×10^2	1.229×10^2	5.853×10^3	6.057×10^3	5.654×10^3
30	8.247×10	1.229×10^2	4.200×10	5.464×10^3	5.654×10^3	5.278×10^3
31	3.169×10	4.200×10	2.139×10	5.101×10^3	5.278×10^3	4.928×10^3

Note: E_0 is the center energy of each bin. E_h and E_l are higher and lower boundaries of each bin.

Table 2.5 Basic parameters of the instrument performance for the SW sensor.

SW				
CHANNEL (DIRECTION)	$\Delta\alpha$ (FWHM)	$\Delta\theta$ (FWHM)	$\Delta\delta$ (FWHM)	g-factor ($cm^2 \cdot str \cdot eV/eV$)
CH1 (−25.2°)	2.5°	8.0°	3.7 %	7.84×10^{-6}
CH2 (−17.2°)	2.5°	8.9°	3.9 %	9.97×10^{-6}
CH3 (−8.6°)	2.5°	8.3°	3.9 %	1.00×10^{-5}
CH4 (0.0°)	2.5°	8.3°	4.0 %	9.81×10^{-6}
CH5 (8.7°)	2.6°	8.4°	4.2 %	1.05×10^{-5}
CH6 (17.3°)	2.7°	8.6°	4.5 %	1.06×10^{-5}
CH7 (26.0°)	2.8°	9.0°	4.4 %	1.07×10^{-5}

Table 2.6 Energy bins of SW.

	SW RAM A			SW RAM B		
STEP	E_0 (eV)	E_h (eV)	E_l (eV)	E_0 (eV)	E_h (eV)	E_l (eV)
0	8.034×10^3	8.308×10^3	7.811×10^3	3.992×10^3	4.089×10^3	3.894×10^3
1	7.548×10^3	7.811×10^3	7.270×10^3	3.760×10^3	3.894×10^3	3.601×10^3
2	6.829×10^3	7.270×10^3	6.453×10^3	3.408×10^3	3.601×10^3	3.223×10^3
3	6.104×10^3	6.453×10^3	5.768×10^3	3.052×10^3	3.223×10^3	2.887×10^3
4	5.456×10^3	5.768×10^3	5.156×10^3	2.734×10^3	2.887×10^3	2.586×10^3
5	4.877×10^3	5.156×10^3	4.609×10^3	2.449×10^3	2.586×10^3	2.317×10^3
6	4.359×10^3	4.609×10^3	4.119×10^3	2.194×10^3	2.317×10^3	2.075×10^3
7	3.897×10^3	4.119×10^3	3.682×10^3	1.965×10^3	2.075×10^3	1.859×10^3
8	3.483×10^3	3.682×10^3	3.291×10^3	1.760×10^3	1.859×10^3	1.665×10^3
9	3.113×10^3	3.291×10^3	2.942×10^3	1.576×10^3	1.665×10^3	1.491×10^3
10	2.783×10^3	2.942×10^3	2.630×10^3	1.412×10^3	1.491×10^3	1.336×10^3
11	2.487×10^3	2.630×10^3	2.351×10^3	1.265×10^3	1.336×10^3	1.196×10^3
12	2.223×10^3	2.351×10^3	2.101×10^3	1.133×10^3	1.196×10^3	1.072×10^3
13	1.987×10^3	2.101×10^3	1.878×10^3	1.015×10^3	1.072×10^3	9.598×10^2
14	1.776×10^3	1.878×10^3	1.679×10^3	9.089×10^2	9.598×10^2	8.597×10^2
15	1.588×10^3	1.679×10^3	1.500×10^3	8.141×10^2	8.597×10^2	7.701×10^2
16	1.419×10^3	1.500×10^3	1.341×10^3	7.292×10^2	7.701×10^2	6.898×10^2
17	1.269×10^3	1.341×10^3	1.199×10^3	6.531×10^2	6.898×10^2	6.178×10^2
18	1.134×10^3	1.199×10^3	1.072×10^3	5.850×10^2	6.178×10^2	5.534×10^2
19	1.014×10^3	1.072×10^3	9.579×10^2	5.240×10^2	5.534×10^2	4.957×10^2
20	9.061×10^2	9.579×10^2	8.562×10^2	4.694×10^2	4.957×10^2	4.440×10^2
21	8.100×10^2	8.562×10^2	7.653×10^2	4.204×10^2	4.440×10^2	3.977×10^2
22	7.239×10^2	7.653×10^2	6.841×10^2	3.766×10^2	3.977×10^2	3.562×10^2
23	6.471×10^2	6.841×10^2	6.115×10^2	3.373×10^2	3.562×10^2	3.191×10^2
24	5.784×10^2	6.115×10^2	5.466×10^2	3.021×10^2	3.191×10^2	2.858×10^2
25	5.170×10^2	5.466×10^2	4.885×10^2	2.706×10^2	2.858×10^2	2.560×10^2
26	4.621×10^2	4.885×10^2	4.367×10^2	2.424×10^2	2.560×10^2	2.293×10^2
27	4.131×10^2	4.367×10^2	3.903×10^2	2.171×10^2	2.293×10^2	2.054×10^2
28	3.692×10^2	3.903×10^2	3.489×10^2	1.945×10^2	2.054×10^2	1.840×10^2
29	3.300×10^2	3.489×10^2	3.119×10^2	1.742×10^2	1.840×10^2	1.648×10^2
30	2.950×10^2	3.119×10^2	2.788×10^2	1.560×10^2	1.648×10^2	1.476×10^2
31	2.637×10^2	2.788×10^2	2.492×10^2	1.398×10^2	1.476×10^2	1.322×10^2

Note: E_0 is the center energy of each bin. E_h and E_l are higher and lower boundaries of each bin.

Table 2.7 Averaged count rates generated by solar EUV for EA-e sensor.

EA-e	
ENERGY STEP	EUV counts (/ 4 spins) CH4
SECTOR 13	
19	0.35
20	0.78
21	1.03
22	1.13
23	1.22
24	1.22
25	1.22
26	1.22
27	1.10
28	0.96
29	0.74
30	0.51
31	0.35
SECTOR 14	
0	0.25
1	0.12

Note: No count rate is generated by solar EUV for other channels, sectors, and energy steps of EA-e.

Table 2.8 Averaged count rates generated by solar EUV for EA-i sensor.

EA-i		
ENERGY STEP	EUV counts (/ 4 spins) CH3 CH5	CH4
SECTOR 13		
20	0.05	0.26
21	0.12	0.65
22	0.22	1.32
23	0.26	1.82
24	0.26	2.07
25	0.28	2.21
26	0.30	2.35
27	0.28	2.24
28	0.26	2.07
29	0.22	1.68
30	0.12	1.15
31	0.08	0.68
SECTOR 14		
0	0.00	0.61
1	0.00	0.39
2	0.00	0.25

Note: No count rate is generated by solar EUV for other channels, sectors, and energy steps of EA-i.

Table 5.1 Examples of slow-mode shocks.

	No.1 1994/1/14 UP 1535:30-1538:00 DN 1541:00-1542:00		No.2 1993/9/17 UP 1645:00-1646:00 DN 1700:30-1701:30		No.3 1994/1/17 UP 1542:30-1543:30 DN 1528:30-1530:00		No.4 1993/9/18 UP 1052:30-1055:30 DN 1043:30-1046:00	
	UP	DOWN	UP	DOWN	UP	DOWN	UP	DOWN
ρ ($10^{-2}cm^{-3}$)	1.9	5.4 (5.0) 9%	1.3	4.2 (4.3) 4%	1.3	3.0 (2.6) 29%	2.9	9.9 (8.5) 14%
B (nT)	11.5	5.6 (7.2) 25%	8.1	6.1 (7.1) 14%	11.1	7.4(8.5) 14%	10.9	7.1 (8.7) 18%
θ_n (deg.)	83.7	73.8 (79.9) 6.1	74.4	67.5 (72.1) 4.6	84.7	82.0 (83.1) 1.1	79.8	74.3 (77.1) 2.8
V (km/s)	140	819 (974) 17%	179	555(482) 13%	122	606 (828) 26%	133	532 (539) 1.3%
θv (deg.)		86.5(86.8) 0.3		84.3 (83.8) 0.6		85.2 (85.9) 0.7		85.8 (85.1) 0.7
T (keV)	0.20	3.83	0.15	1.03	0.08	4.2	0.17	1.18
Te (keV)	0.17	0.53	0.11	0.25	0.06	0.57	0.10	0.11
Ti (keV)	0.02	3.3	0.03	0.78	0.02	3.7	0.07	1.07
E_{tot} ($10^{-5}J/m^2$)	1.5	1.2 | 25%	0.87	0.63 | 29%	1.2	0.9 | 25%	1.2	0.97 | 19%
M_A	0.08		0.11		0.05		0.10	
Mi	0.71	0.44	0.42	0.22	0.61	0.42	0.54	0.32
Ms	7.24	0.57	4.38	0.48	11.71	0.69	4.53	0.54
$\Delta\phi_{bv}$ (deg.)	8.6		3.3		17.8		2.3	
n (GSE)	(-0.02,-0.03,-0.99)		(0.24,0.21,0.95)		(-0.02,-0.63,-0.77)		(-0.17,0.94,0.28)	
Vs (km/s)	104		133		97		103	
position (Re) (GSE)	(-96.1,8.3,4.5)		(-71.5,11.2,5.1)		(-92.3,0.3,-5.0)		(-69.0,7.9,0.05)	

Table 5.2 A slow-mode shock on the front side of a plasmoid.

	1993/9/18 UP 1032:30-1034:30 DN 1035:30-1036:00	
	UP	DOWN
ρ (10^{-2} cm^{-3})	3.5	9.5 (10.1) 12%
B (nT)	11.1	7.0 (8.0) 13%
θ_b (deg.)	55.8	33.6 (43.4) 9.8
V (km/s)	486	652 (656) 0.7%
θv (deg.)		73.9(76.1) 2.2
T (keV)	0.11	2.19
Te (keV)	0.09	0.16
Ti (keV)	0.02	2.03
E_{tot} (10^{-5} J/m^2)	3.8	3.8 | 0.4%
M_A	0.38	
M_f	0.72	0.41
M_s	7.10	0.52
$\Delta\phi_{bv}$ (deg.)	6.7	
n (GSE)	(-0.56,0.80,-0.21)	
Vs (km/s)	592	
position (Re) (GSE)	(-69.1,9.2,-0.5)	

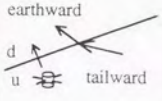

Table 5.3 Types of the plasma sheet boundary layers.

SLOW-SHOCK	32	11 %
(PLASMOID)	(9)	(3 %)
TYPE 1	94	31 %
TYPE 2	80	26 %
TYPE 3	34	11 %
TYPE 4	9	3 %
TYPE 5	19	6 %
TYPE 6	10	3 %
TYPE 7	7	2 %
TYPE 8	18	6 %
TOTAL	303	100%

Table 6.1 Ring distributed ions observed between September 14, 1993 and October 15, 1993.

No.	PSBL "beam"	δ (deg.)	V_{center} (km/s)	V_{gyro} (km/s)	n_{ring} (/cc)	n_{beam} (/cc)	V_{beam} (km/s)	date (1993)	time (UT)	position(GSM) X	Y	Z
1	tailward	5	567	928	0.009	0.002	2240	09/14	1603:48	-71.3	22.2	-4.3
2	×	8	159	284	0.035	×	×	09/17	1138:56	-72.0	12.9	-2.4
3	earthward	~0	0	568	0.044	0.001	1168	09/17	1405:58	-71.8	12.6	-1.4
4	tailward	~0	330	470	0.020	0.078	1098	09/18	1025:34	-69.1	9.2	-0.5
5	tailward	10	159	308	0.021	0.081	1003	09/18	1037:09	-69.0	9.2	-0.5
6	tailward	~0	379	503	0.020	0.087	1115	09/18	1044:09	-69.0	9.2	-0.5
7	tailward	3	163	241	0.034	0.114	753	09/18	1105:43	-69.0	9.1	-0.5
8	tailward	20	243	433	0.048	0.001	1089	09/18	1410:19	-68.4	8.6	0.4
9	earthward	~0	212	478	0.016	0.008	812	09/18	1601:48	-68.0	8.1	1.3
10	tailward	3	0	541	0.043	0.030	1013	10/15	1234:23	-169.1	3.2	9.8
11	tailward	3	113	730	0.020	0.018	1025	10/15	1236:23	-169.1	3.2	9.8

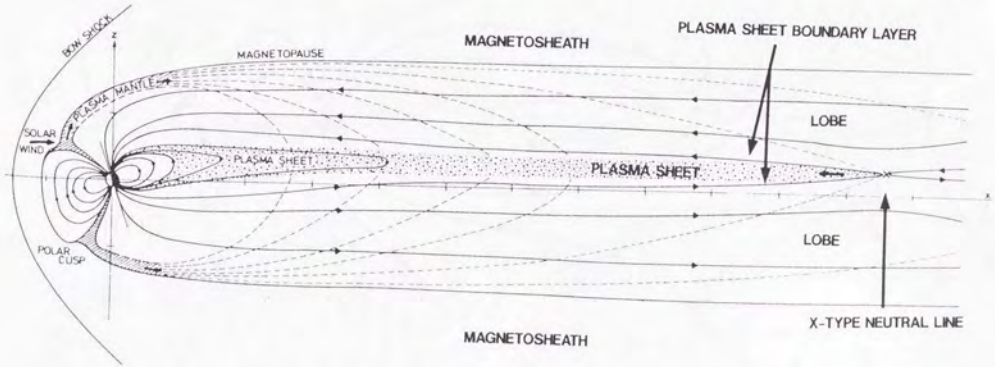
BOW SHOCK
MAGNETOPAUSE
MAGNETOSHEATH
PLASMA SHEET BOUNDARY LAYER
PLASMA MANTLE
SOLAR WIND
LOBE
PLASMA SHEET
PLASMA SHEET
LOBE
POLAR CUSP
X-TYPE NEUTRAL LINE
MAGNETOSHEATH

Figure 1.1

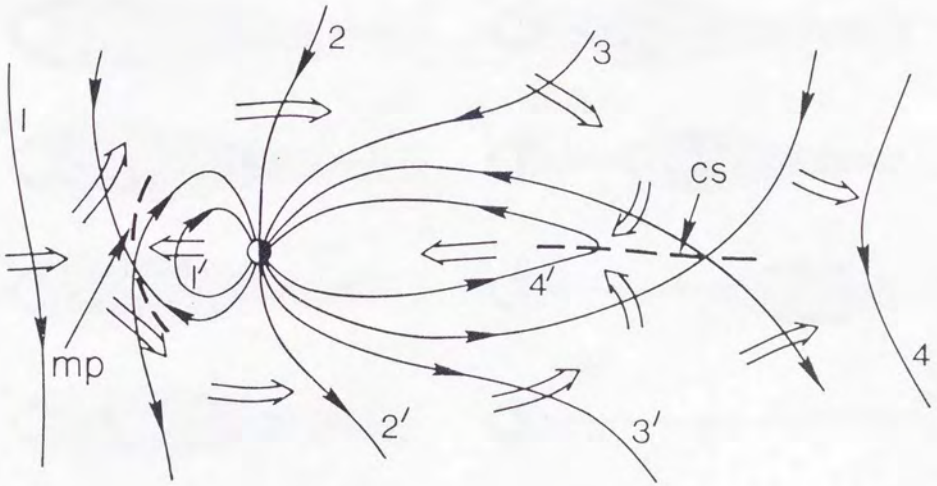

Figure 1.2

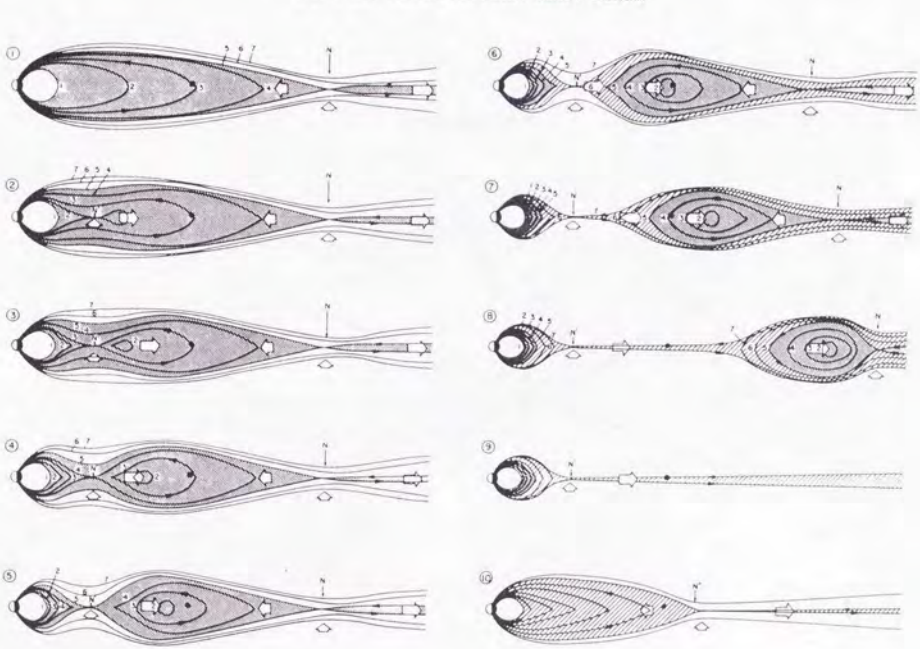

Figure 1.3

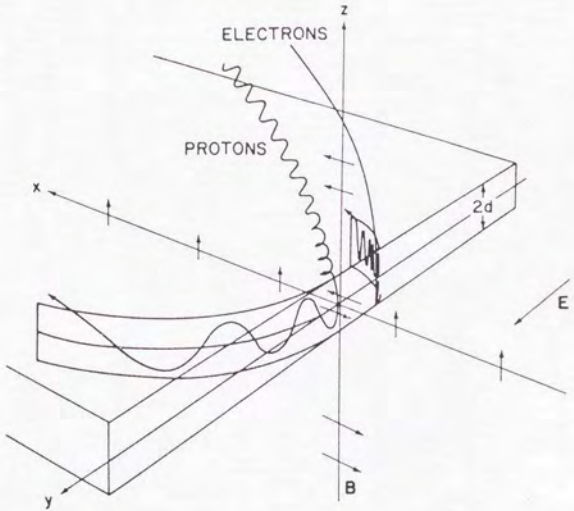

Figure 1.4

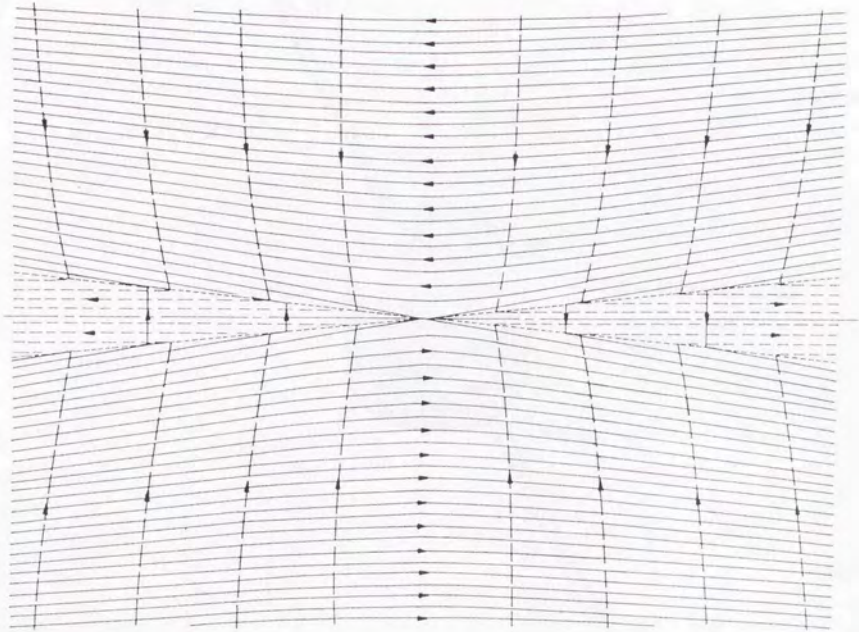

Figure 1.5

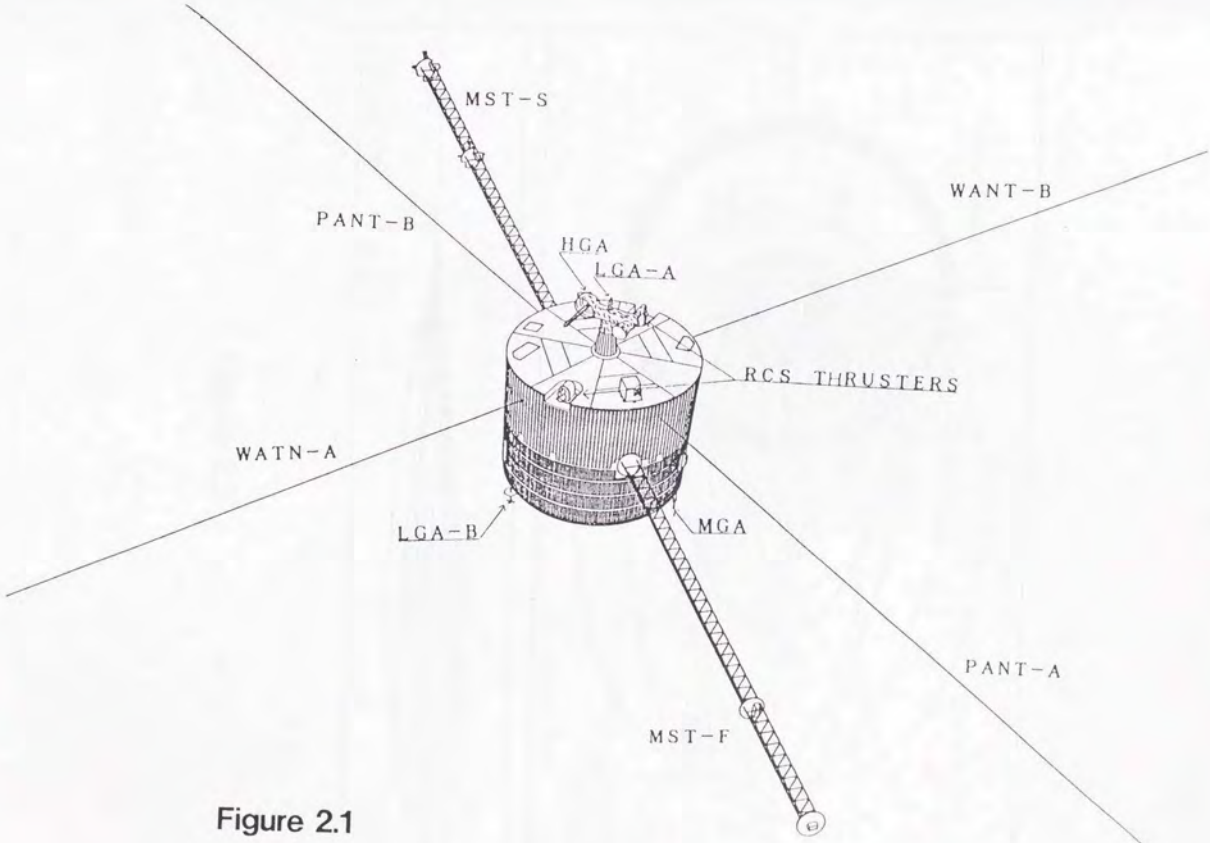
MST-S
PANT-B
WANT-B
HGA
LGA-A
RCS THRUSTERS
WATN-A
LGA-B
MGA
PANT-A
MST-F

Figure 2.1

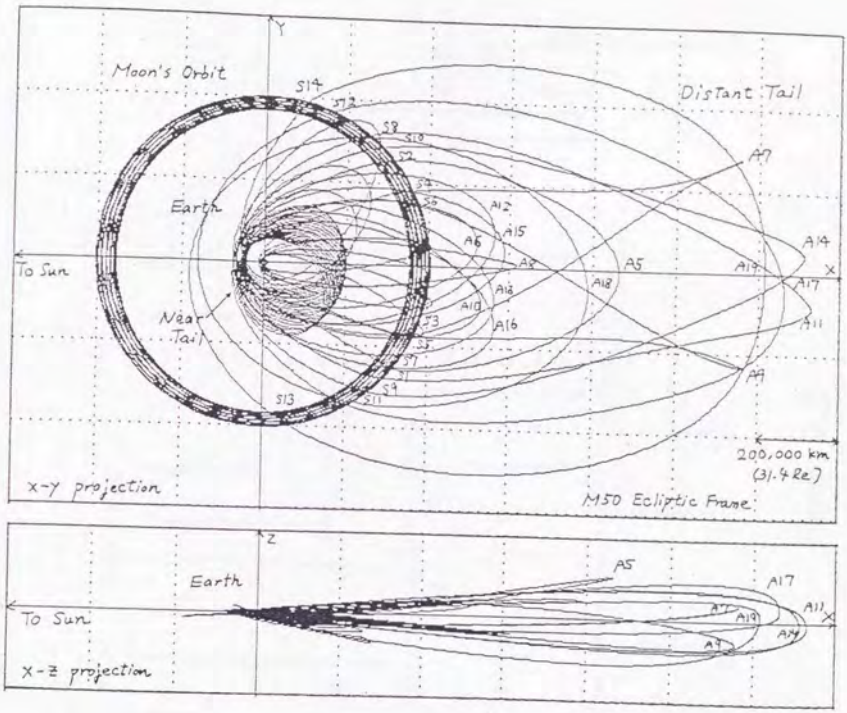
Moon's Orbit
Distant Tail
Earth
To Sun
Near Tail
x-y projection
M50 Ecliptic Frame
200,000 km
(31.4 Re)
Earth
To Sun
x-z projection

Figure 2.2

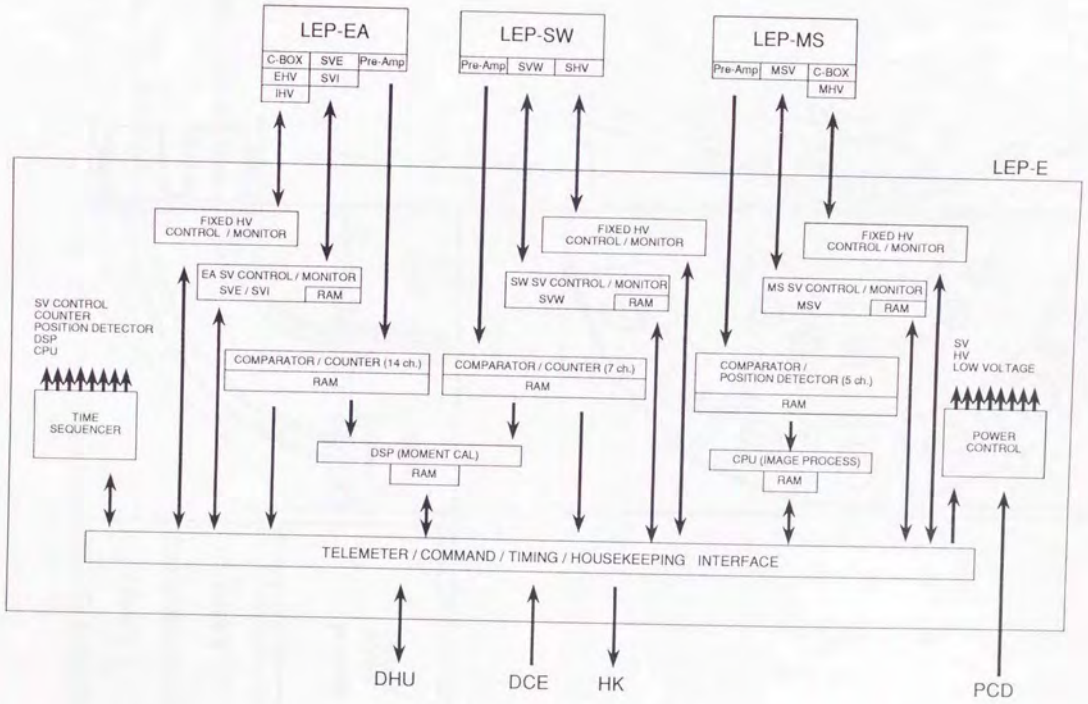
LEP-EA
C-BOX
SVE
Pre-Amp
EHV
SVI
IHV
LEP-SW
Pre-Amp
SVW
SHV
LEP-MS
Pre-Amp
MSV
C-BOX
MHV
LEP-E
FIXED HV CONTROL / MONITOR
FIXED HV CONTROL / MONITOR
FIXED HV CONTROL / MONITOR
EA SV CONTROL / MONITOR
SVE / SVI
RAM
SW SV CONTROL / MONITOR
SVW
RAM
MS SV CONTROL / MONITOR
MSV
RAM
SV CONTROL
COUNTER
POSITION DETECTOR
DSP
CPU
TIME SEQUENCER
COMPARATOR / COUNTER (14 ch.)
RAM
COMPARATOR / COUNTER (7 ch.)
RAM
COMPARATOR / POSITION DETECTOR (5 ch.)
RAM
SV
HV
LOW VOLTAGE
POWER CONTROL
DSP (MOMENT CAL)
RAM
CPU (IMAGE PROCESS)
RAM
TELEMETER / COMMAND / TIMING / HOUSEKEEPING INTERFACE
DHU
DCE
HK
PCD

Figure 2.3

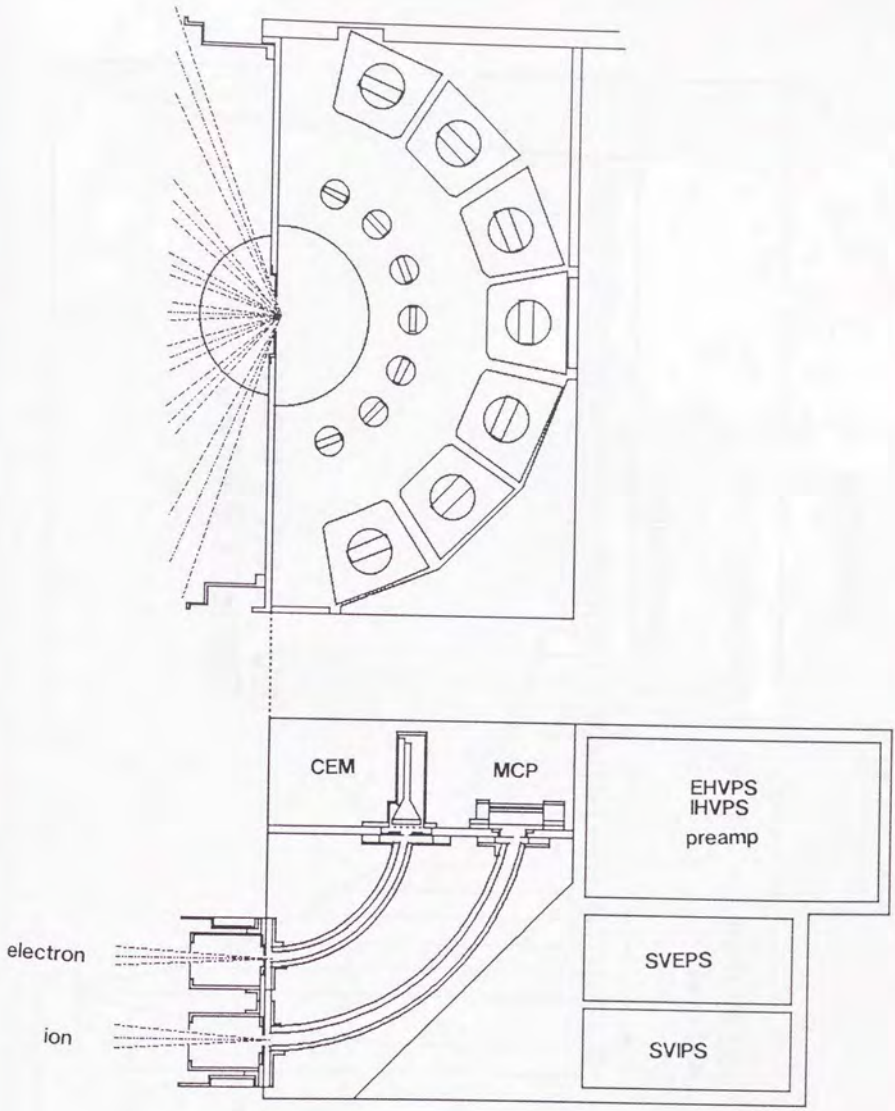

Figure 2.4

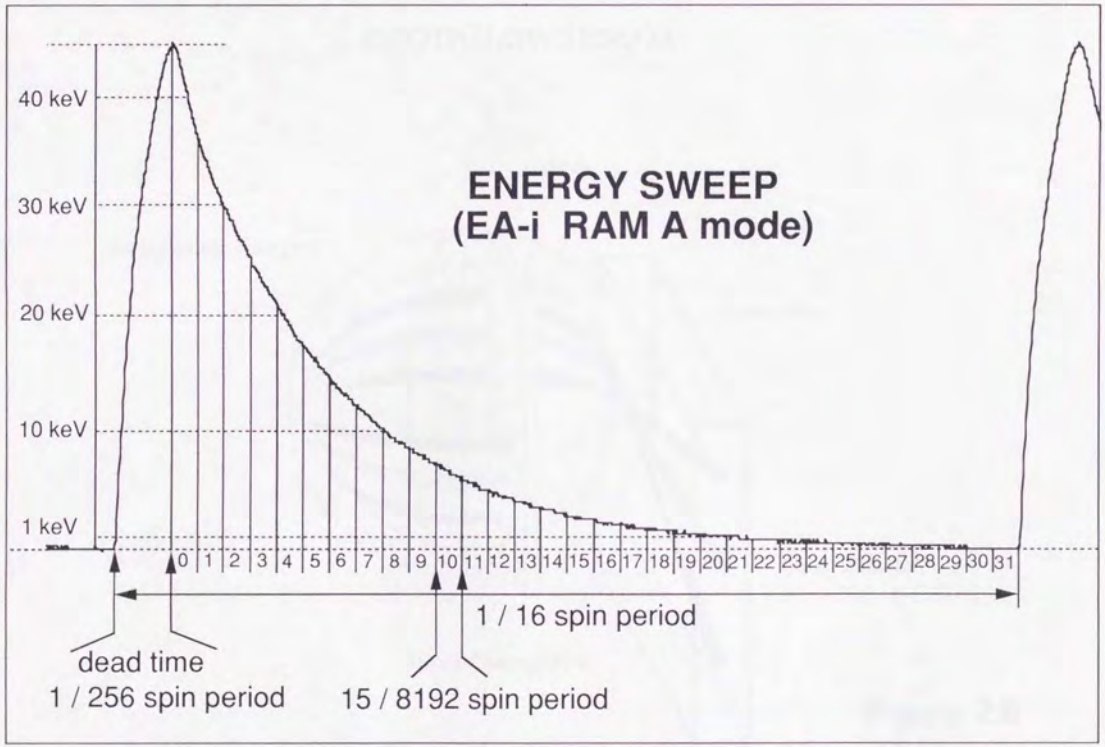
ENERGY SWEEP
(EA-i RAM A mode)
40 keV
30 keV
20 keV
10 keV
1 keV
0 1 2 3 4 5 6 7 8 9 10 11 12 13 14 15 16 17 18 19 20 21 22 23 24 25 26 27 28 29 30 31
1 / 16 spin period
dead time
1 / 256 spin period
15 / 8192 spin period

Figure 2.5

GEOTAIL/SW SENSOR

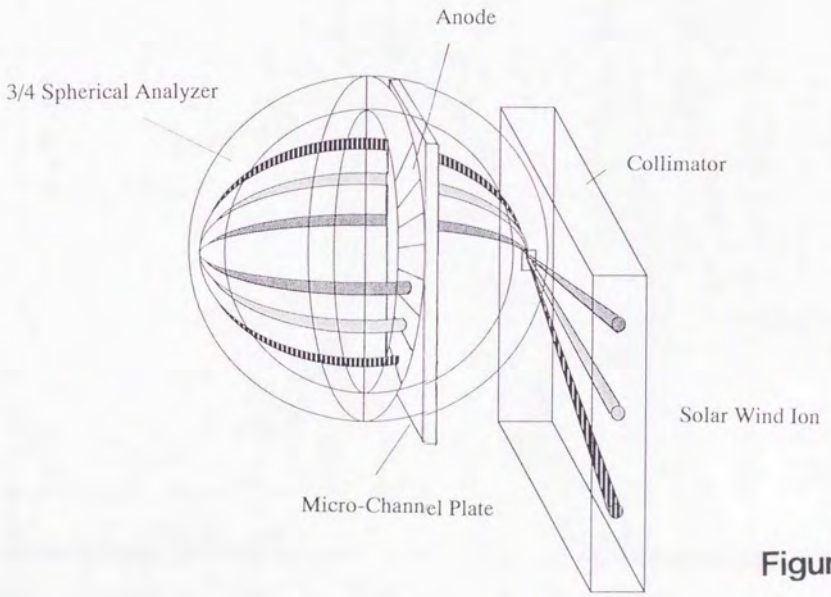

Figure 2.6

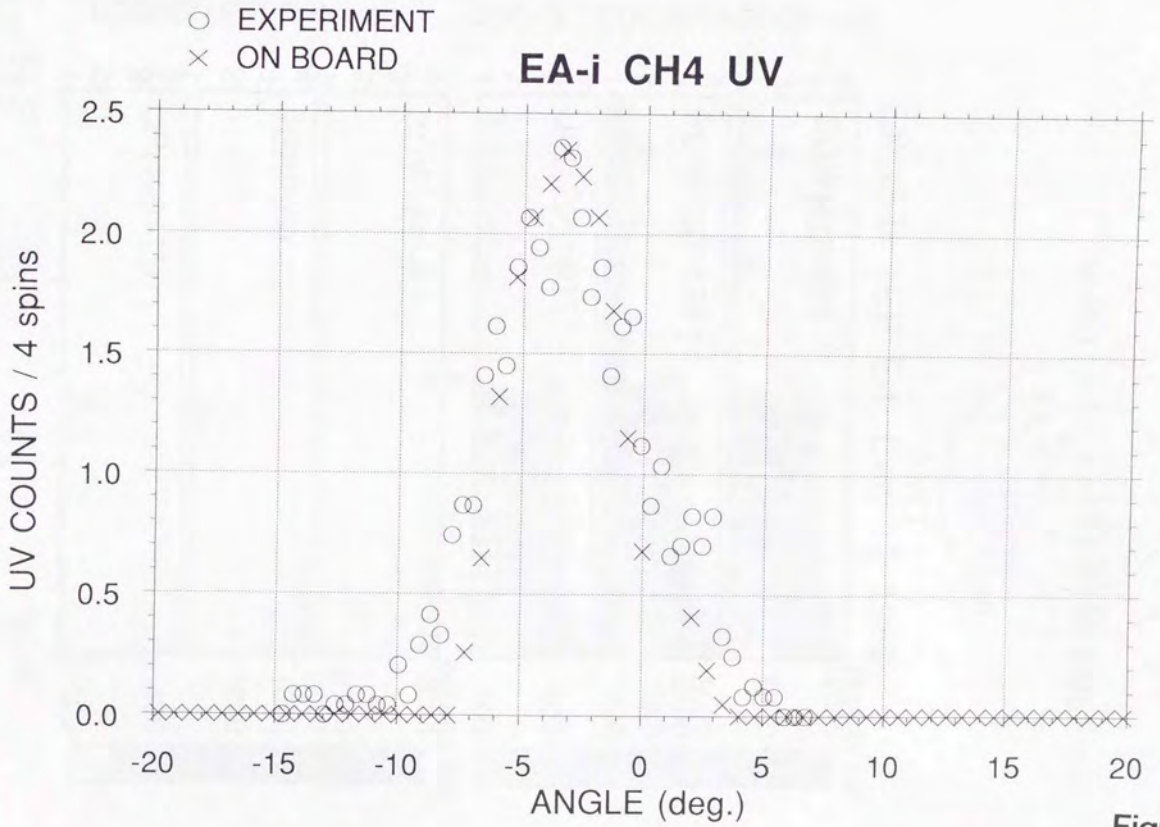
EXPERIMENT
ON BOARD
EA-i CH4 UV
UV COUNTS / 4 spins
2.5
2.0
1.5
1.0
0.5
0.0
-20
-15
-10
-5
0
5
10
15
20
ANGLE (deg.)

Figure 2.7

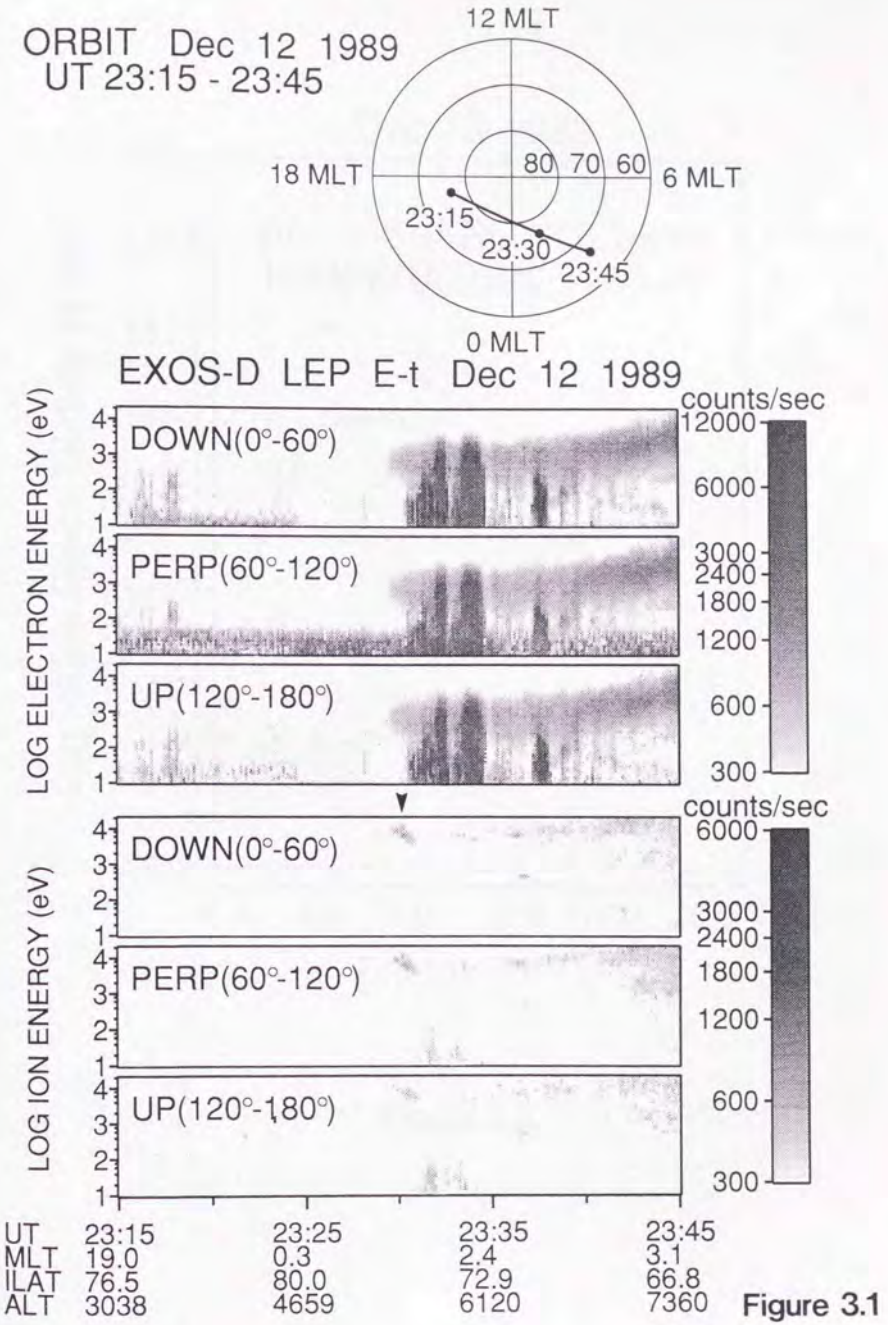
ORBIT Dec 12 1989
UT 23:15 - 23:45
12 MLT
18 MLT
6 MLT
0 MLT
80 70 60
23:15
23:30
23:45
EXOS-D LEP E-t Dec 12 1989
LOG ELECTRON ENERGY (eV)
DOWN(0°-60°)
PERP(60°-120°)
UP(120°-180°)
counts/sec
12000
6000
3000
2400
1800
1200
600
300
LOG ION ENERGY (eV)
DOWN(0°-60°)
PERP(60°-120°)
UP(120°-180°)
counts/sec
6000
3000
2400
1800
1200
600
300
UT 23:15 23:25 23:35 23:45
MLT 19.0 0.3 2.4 3.1
ILAT 76.5 80.0 72.9 66.8
ALT 3038 4659 6120 7360

Figure 3.1

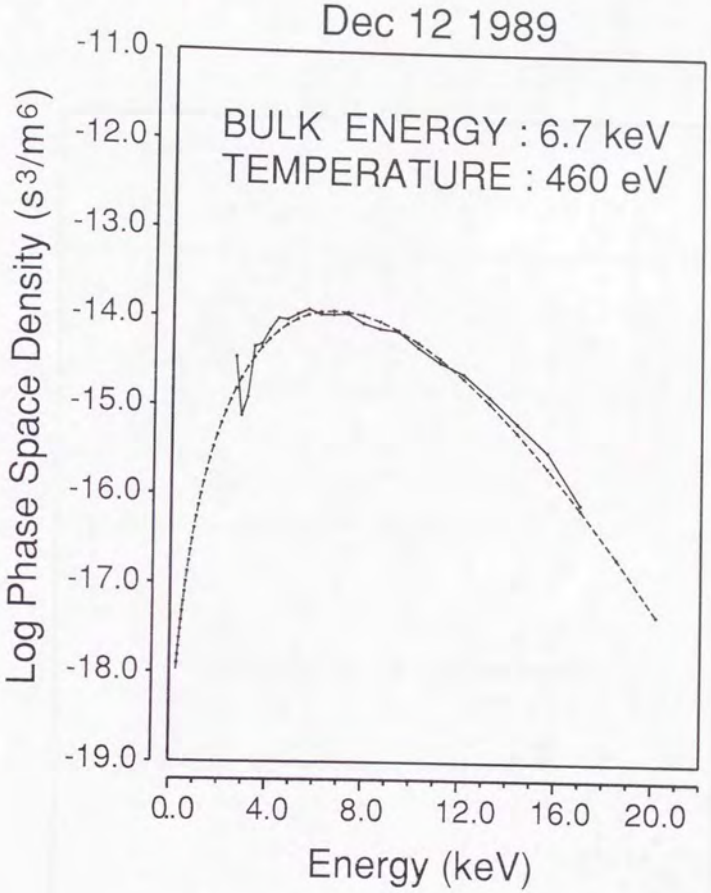
Dec 12 1989
BULK ENERGY : 6.7 keV
TEMPERATURE : 460 eV
Log Phase Space Density (s3/m6)
-11.0
-12.0
-13.0
-14.0
-15.0
-16.0
-17.0
-18.0
-19.0
0.0
4.0
8.0
12.0
16.0
20.0
Energy (keV)

Figure 3.2

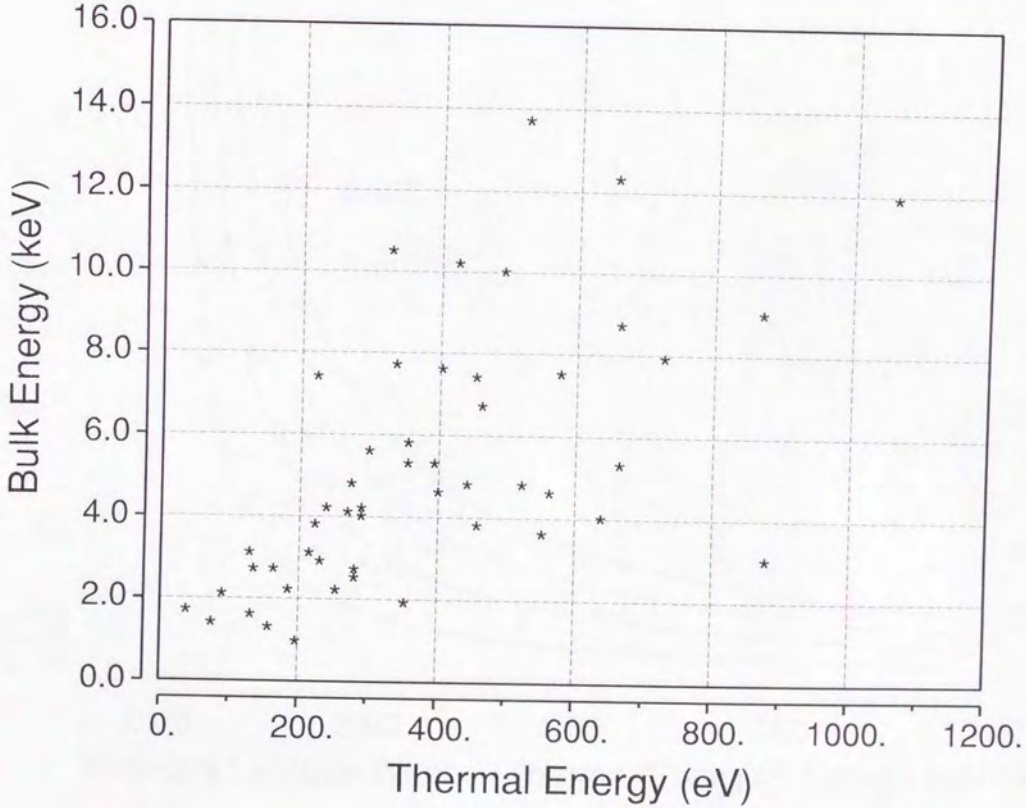
16.0
14.0
12.0
10.0
8.0
6.0
4.0
2.0
0.0
Bulk Energy (keV)
0.
200.
400.
600.
800.
1000.
1200.
Thermal Energy (eV)

Figure 3.3

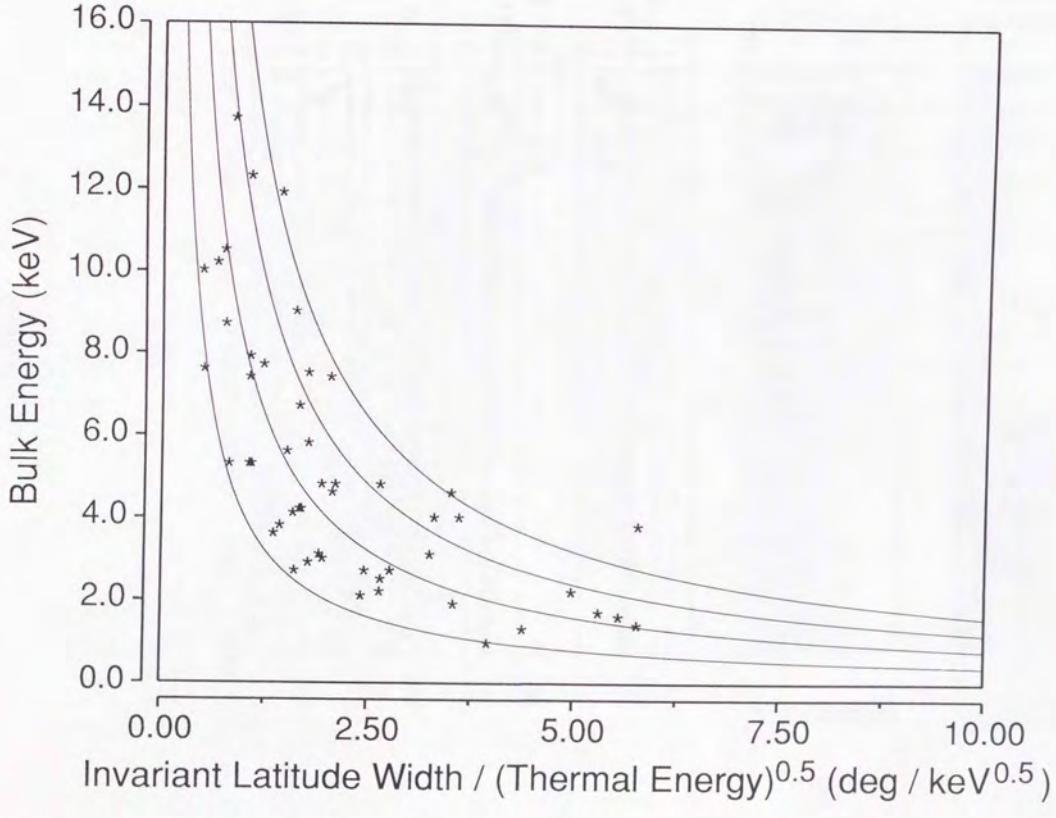
16.0
14.0
12.0
10.0
8.0
6.0
4.0
2.0
0.0
Bulk Energy (keV)
0.00
2.50
5.00
7.50
10.00
Invariant Latitude Width / (Thermal Energy)$^{0.5}$ (deg / keV$^{0.5}$)

Figure 3.4

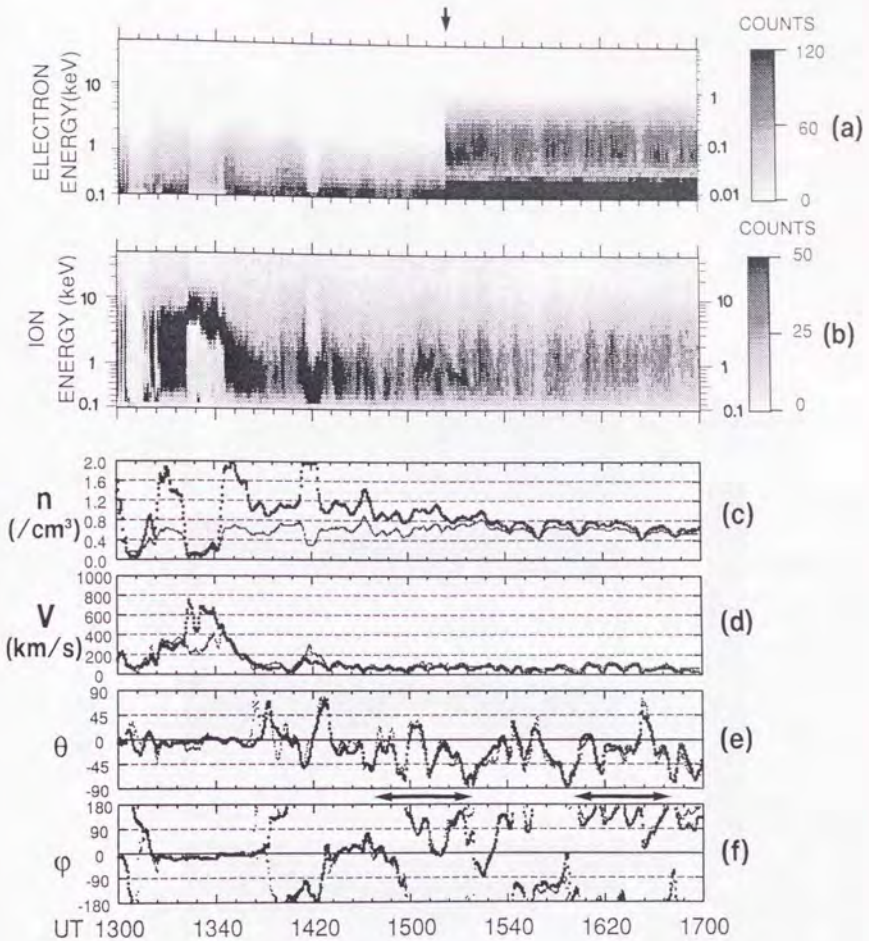
ELECTRON ENERGY(keV)
10
1
0.1
1
0.1
0.01
COUNTS
120
60
0
(a)
ION ENERGY (keV)
10
1
0.1
10
1
0.1
COUNTS
50
25
0
(b)
n (/cm³)
2.0
1.6
1.2
0.8
0.4
0.0
(c)
V (km/s)
1000
800
600
400
200
0
(d)
θ
90
45
0
-45
-90
(e)
φ
180
90
0
-90
-180
(f)
UT 1300
1340
1420
1500
1540
1620
1700

Figure 4.1

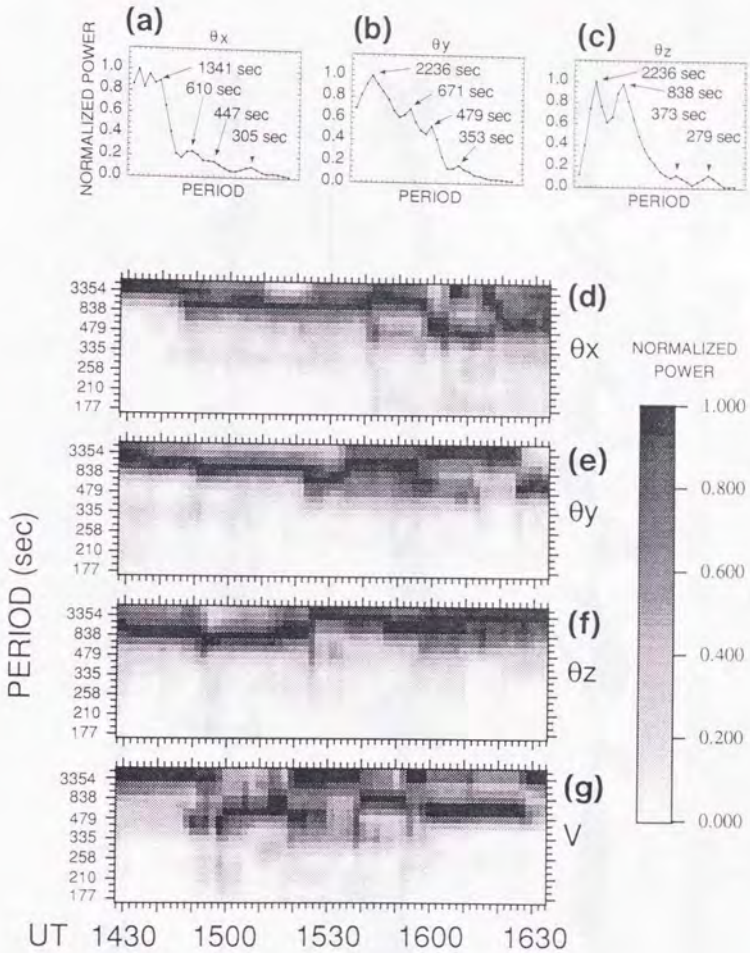
(a)
θx
1341 sec
610 sec
447 sec
305 sec
NORMALIZED POWER
PERIOD
(b)
θy
2236 sec
671 sec
479 sec
353 sec
PERIOD
(c)
θz
2236 sec
838 sec
373 sec
279 sec
PERIOD
(d)
θx
(e)
θy
(f)
θz
(g)
V
PERIOD (sec)
3354
838
479
335
258
210
177
UT 1430 1500 1530 1600 1630
NORMALIZED POWER
1.000
0.800
0.600
0.400
0.200
0.000

Figure 4.2

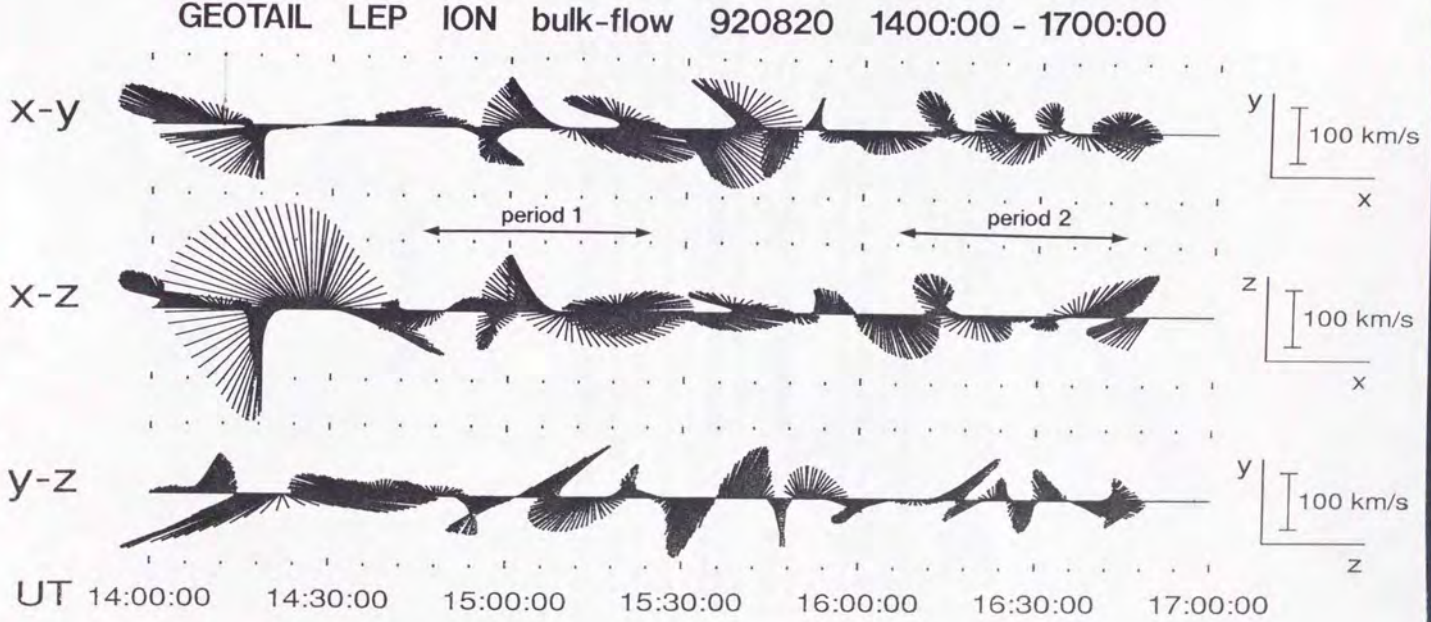
GEOTAIL LEP ION bulk-flow 920820 1400:00 - 1700:00
x-y
y
100 km/s
x
period 1
period 2
x-z
z
100 km/s
x
y-z
y
100 km/s
z
UT 14:00:00 14:30:00 15:00:00 15:30:00 16:00:00 16:30:00 17:00:00

Figure 4.3

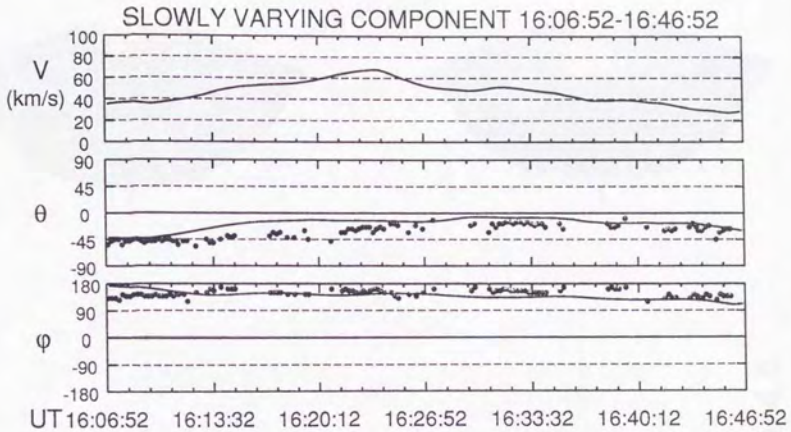
SLOWLY VARYING COMPONENT 16:06:52-16:46:52
V
(km/s)
100
80
60
40
20
0
θ
90
45
0
-45
-90
φ
180
90
0
-90
-180
UT 16:06:52
16:13:32
16:20:12
16:26:52
16:33:32
16:40:12
16:46:52

Figure 4.4

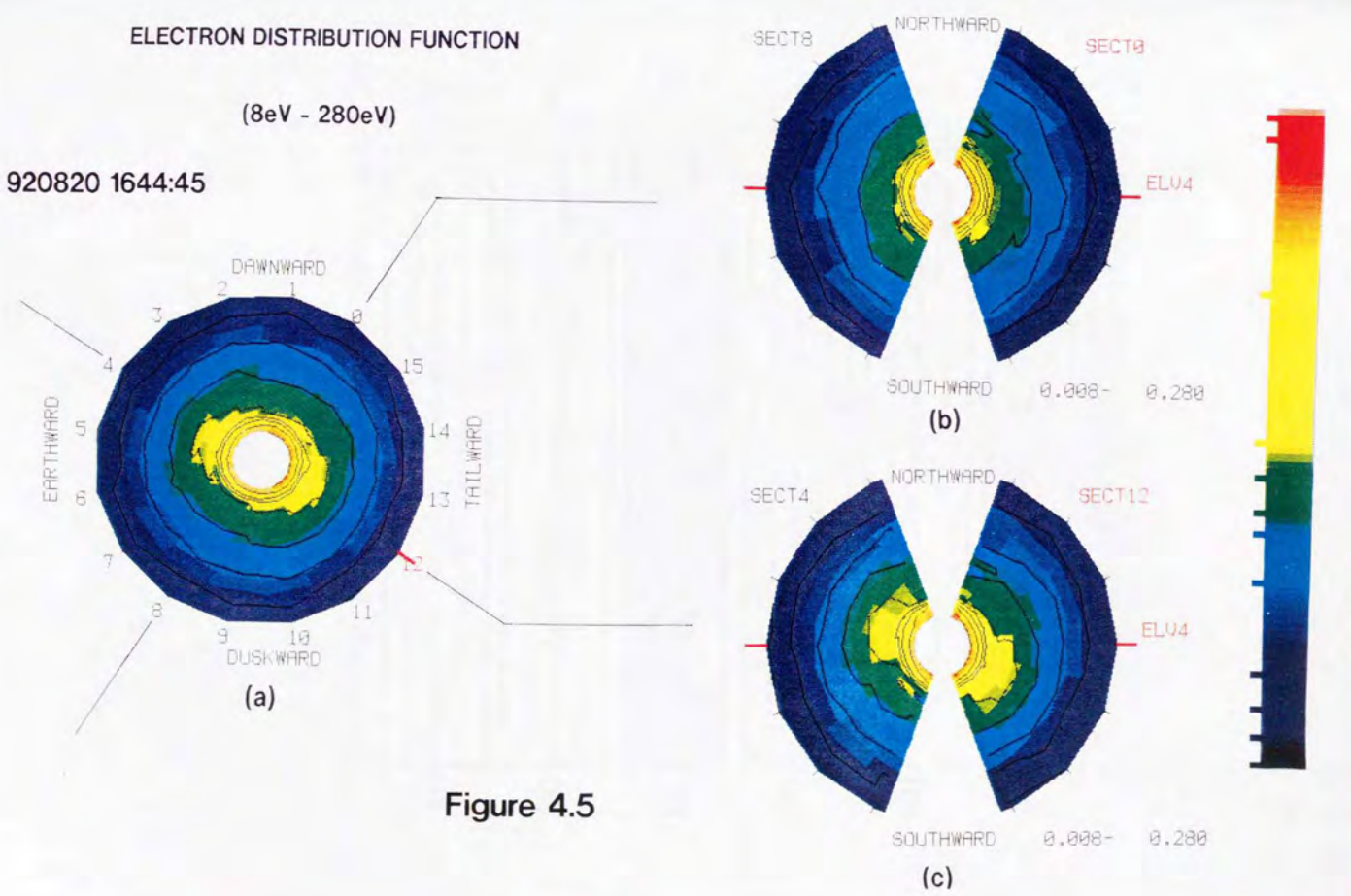
ELECTRON DISTRIBUTION FUNCTION
(8eV - 280eV)
920820 1644:45
DAWNWARD
DUSKWARD
EARTHWARD
TAILWARD
0
1
2
3
4
5
6
7
8
9
10
11
12
13
14
15
(a)
SECT8
NORTHWARD
SECT0
ELV4
SOUTHWARD
0.008-
0.280
(b)
SECT4
NORTHWARD
SECT12
ELV4
SOUTHWARD
0.008-
0.280
(c)

Figure 4.5

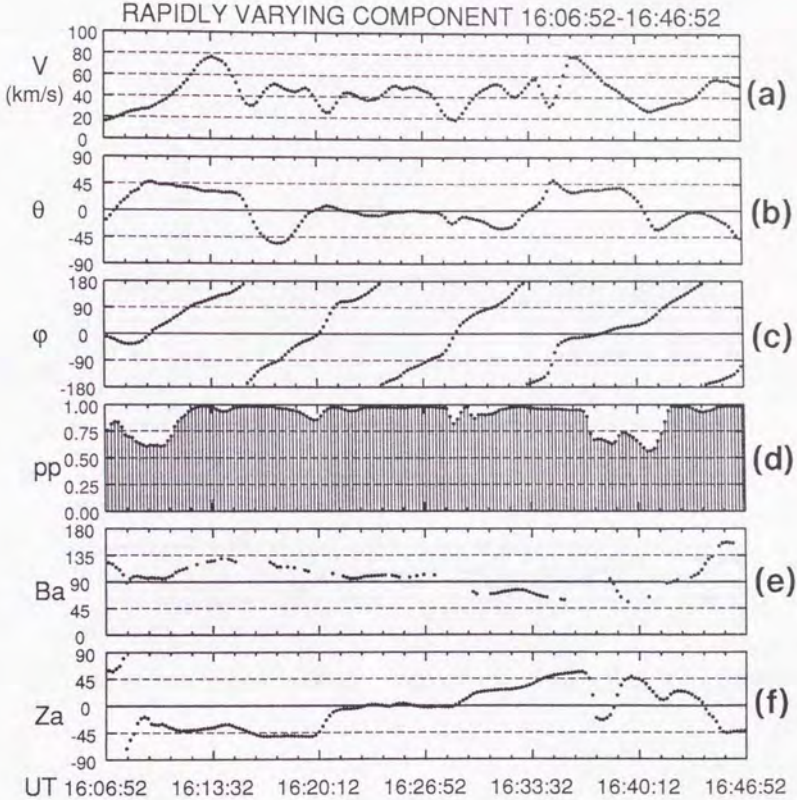
RAPIDLY VARYING COMPONENT 16:06:52-16:46:52
V
(km/s)
100
80
60
40
20
0
(a)
θ
90
45
0
-45
-90
(b)
φ
180
90
0
-90
-180
(c)
pp
1.00
0.75
0.50
0.25
0.00
(d)
Ba
180
135
90
45
0
(e)
Za
90
45
0
-45
-90
(f)
UT 16:06:52 16:13:32 16:20:12 16:26:52 16:33:32 16:40:12 16:46:52

Figure 4.6

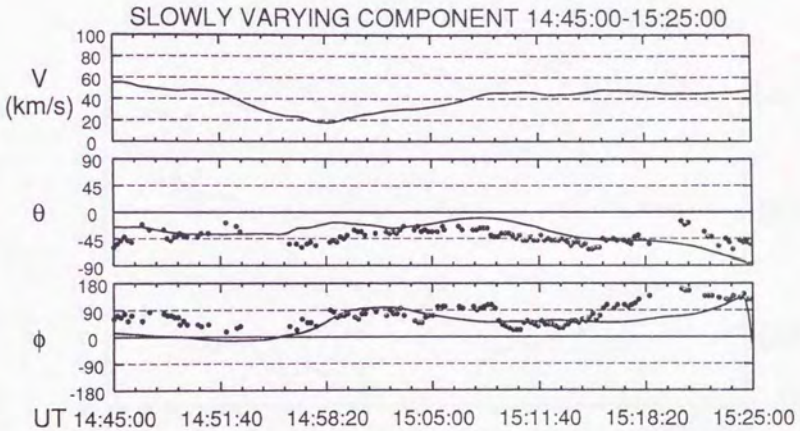
SLOWLY VARYING COMPONENT 14:45:00-15:25:00
V
(km/s)
100
80
60
40
20
0
θ
90
45
0
-45
-90
ϕ
180
90
0
-90
-180
UT 14:45:00
14:51:40
14:58:20
15:05:00
15:11:40
15:18:20
15:25:00

Figure 4.7

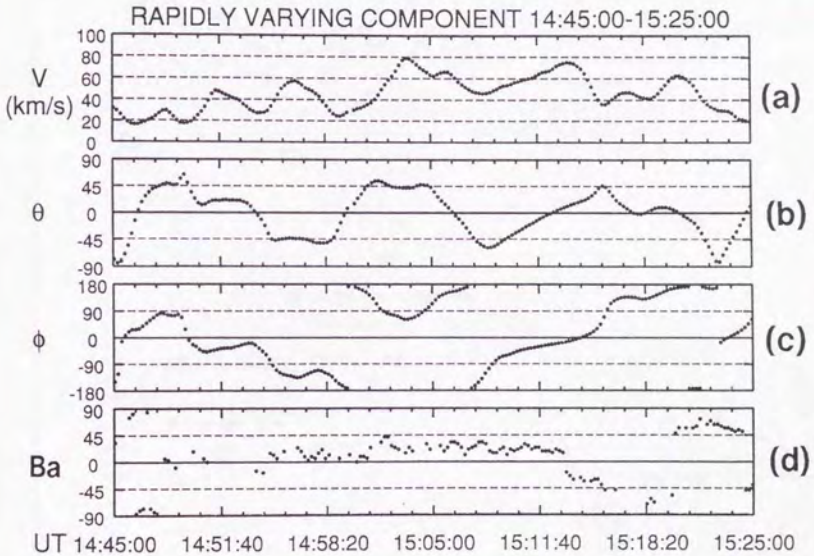
RAPIDLY VARYING COMPONENT 14:45:00-15:25:00
V
(km/s)
100
80
60
40
20
0
(a)
θ
90
45
0
-45
-90
(b)
ϕ
180
90
0
-90
-180
(c)
Ba
90
45
0
-45
-90
(d)
UT 14:45:00
14:51:40
14:58:20
15:05:00
15:11:40
15:18:20
15:25:00

Figure 4.8

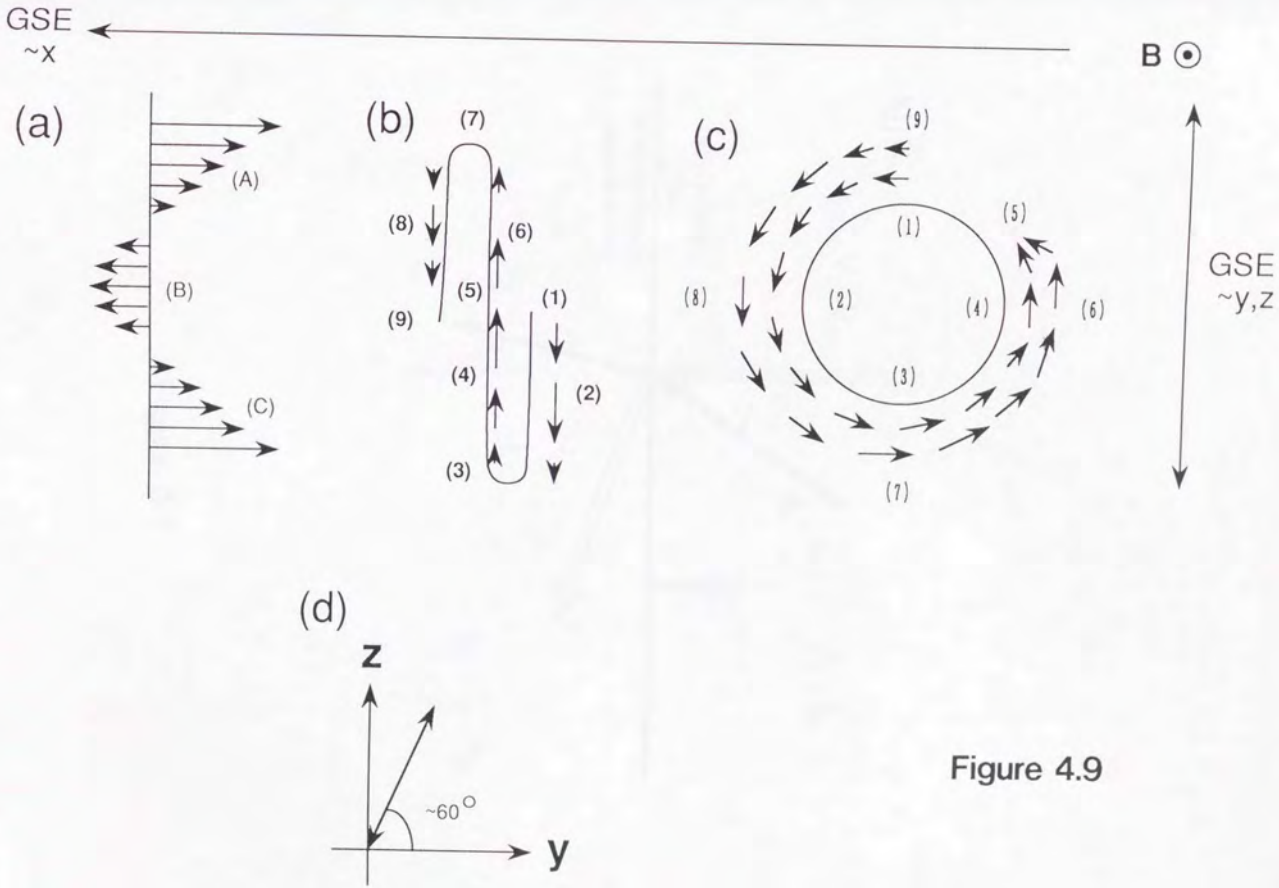

Figure 4.9

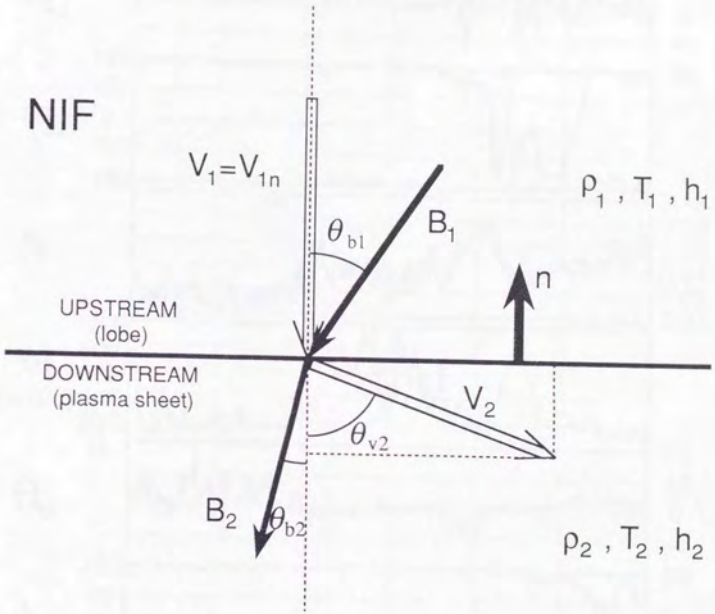
NIF
$V_1=V_{1n}$
θ_{b1}
B_1
ρ_1 , T_1 , h_1
n
UPSTREAM
(lobe)
DOWNSTREAM
(plasma sheet)
V_2
θ_{v2}
B_2
θ_{b2}
ρ_2 , T_2 , h_2

Figure 5.1

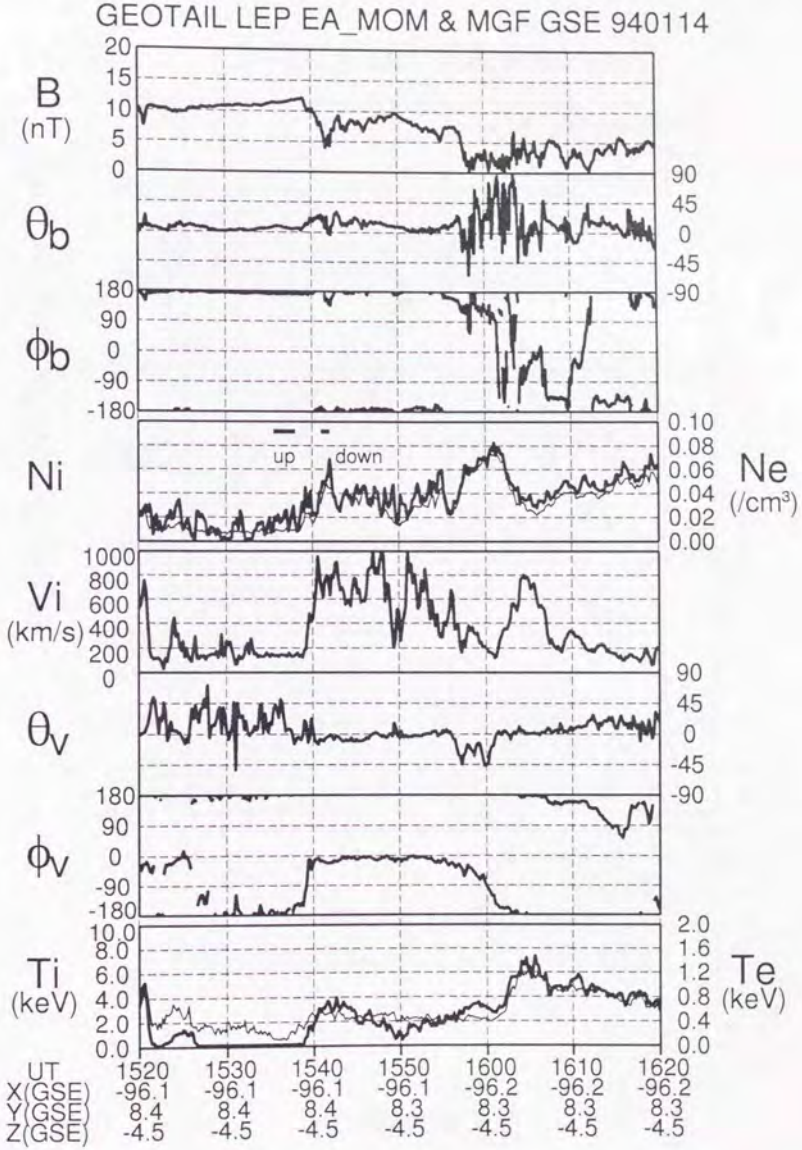
GEOTAIL LEP EA_MOM & MGF GSE 940114
B
(nT)
20
15
10
5
0
θb
90
45
0
-45
-90
φb
180
90
0
-90
-180
Ni
up
down
0.10
0.08
0.06
0.04
0.02
0.00
Ne
(/cm³)
Vi
(km/s)
1000
800
600
400
200
0
θv
φv
10.0
8.0
6.0
4.0
2.0
0.0
Ti
(keV)
2.0
1.6
1.2
0.8
0.4
0.0
Te
(keV)
UT 1520 1530 1540 1550 1600 1610 1620
X(GSE) -96.1 -96.1 -96.1 -96.1 -96.2 -96.2 -96.2
Y(GSE) 8.4 8.4 8.4 8.3 8.3 8.3 8.3
Z(GSE) -4.5 -4.5 -4.5 -4.5 -4.5 -4.5 -4.5

Figure 5.2

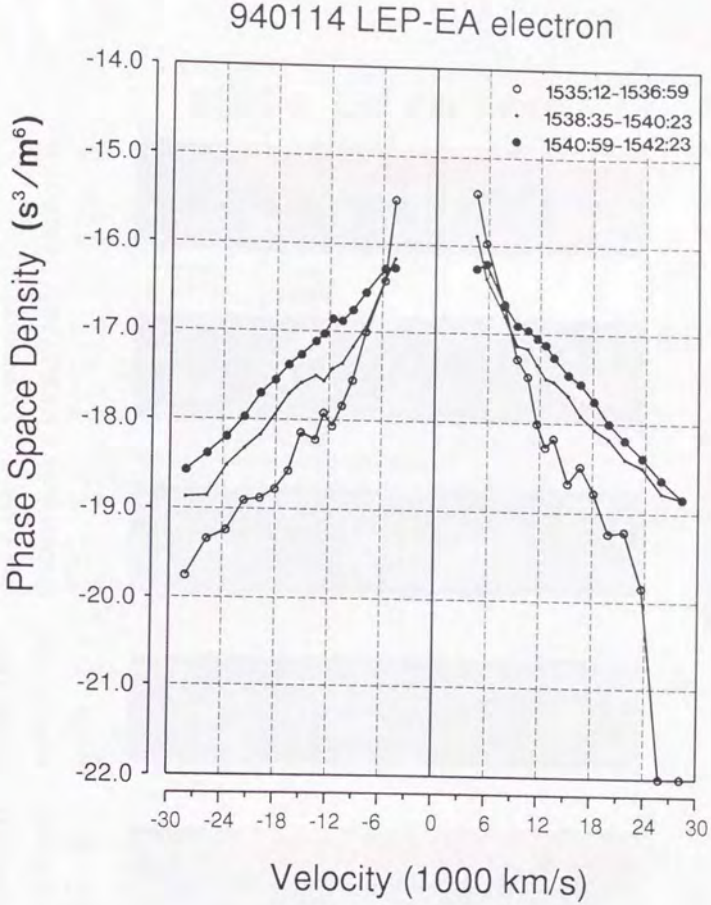
940114 LEP-EA electron
1535:12-1536:59
1538:35-1540:23
1540:59-1542:23
Phase Space Density (s³/m⁶)
-14.0
-15.0
-16.0
-17.0
-18.0
-19.0
-20.0
-21.0
-22.0
-30
-24
-18
-12
-6
0
6
12
18
24
30
Velocity (1000 km/s)

Figure 5.3

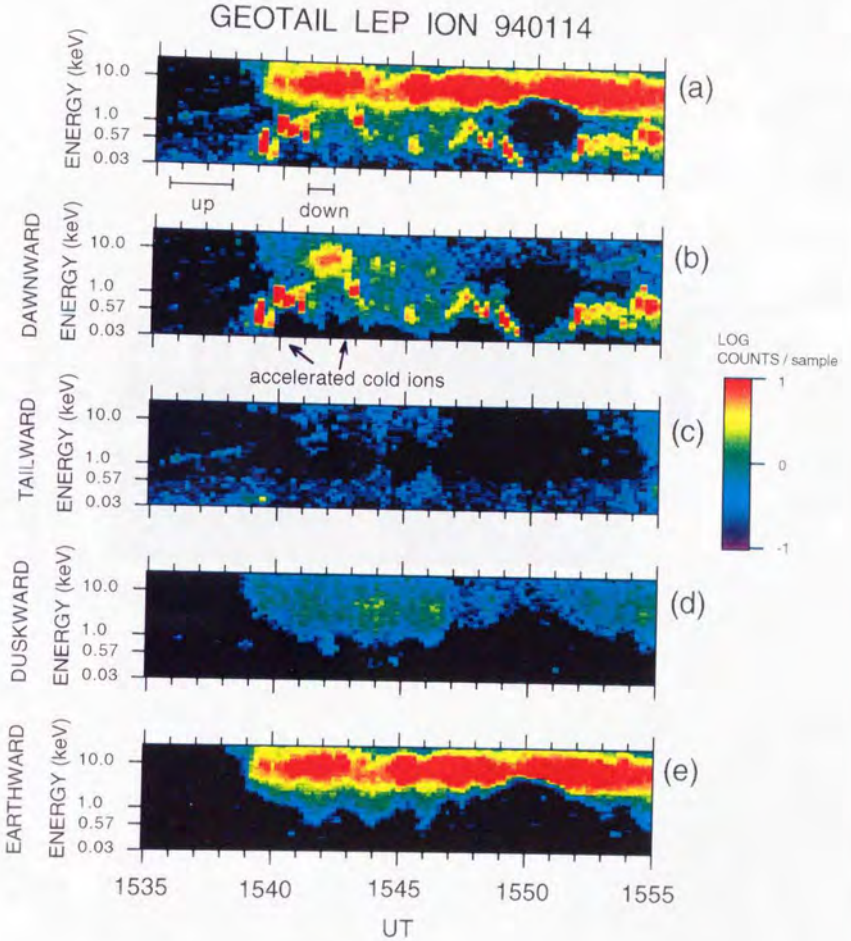
GEOTAIL LEP ION 940114
ENERGY (keV)
10.0
1.0
0.57
0.03
(a)
up
down
DAWNWARD
(b)
accelerated cold ions
TAILWARD
(c)
LOG
COUNTS / sample
1
0
-1
DUSKWARD
(d)
EARTHWARD
(e)
1535
1540
1545
1550
1555
UT

Figure 5.4

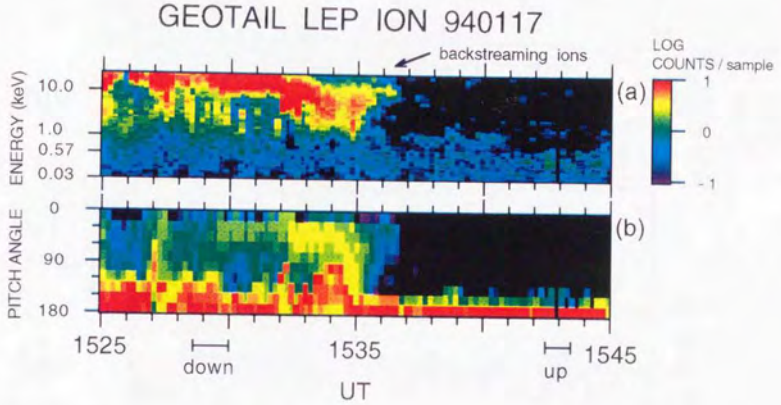
GEOTAIL LEP ION 940117
backstreaming ions
LOG
COUNTS / sample
1
0
- 1
ENERGY (keV)
10.0
1.0
0.57
0.03
(a)
PITCH ANGLE
0
90
180
(b)
1525
down
1535
up
1545
UT

Figure 5.5

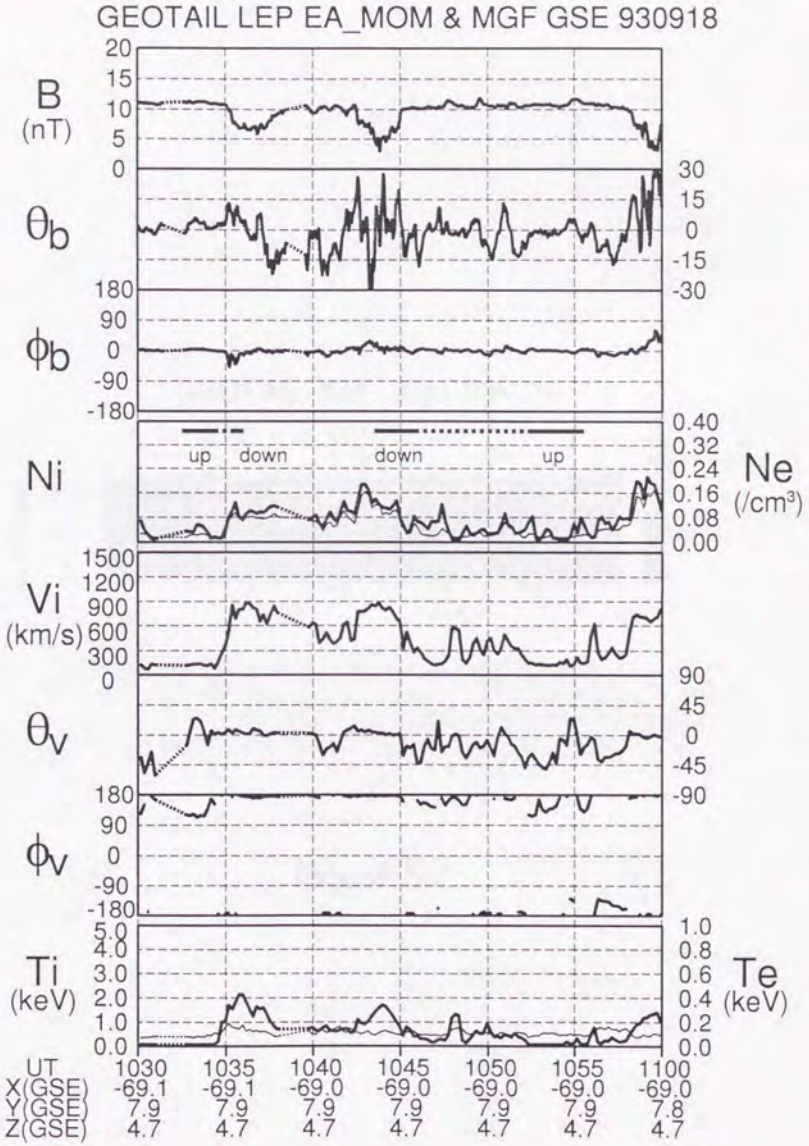
GEOTAIL LEP EA_MOM & MGF GSE 930918
B
(nT)
20
15
10
5
0
θb
30
15
0
-15
-30
180
90
0
-90
-180
φb
Ni
up
down
down
up
0.40
0.32
0.24
0.16
0.08
0.00
Ne
(/cm3)
Vi
(km/s)
1500
1200
900
600
300
0
θv
90
45
0
-45
-90
φv
Ti
(keV)
5.0
4.0
3.0
2.0
1.0
0.0
1.0
0.8
0.6
0.4
0.2
0.0
Te
(keV)
UT 1030 1035 1040 1045 1050 1055 1100
X(GSE) -69.1 -69.1 -69.0 -69.0 -69.0 -69.0 -69.0
Y(GSE) 7.9 7.9 7.9 7.9 7.9 7.9 7.8
Z(GSE) 4.7 4.7 4.7 4.7 4.7 4.7 4.7

Figure 5.6

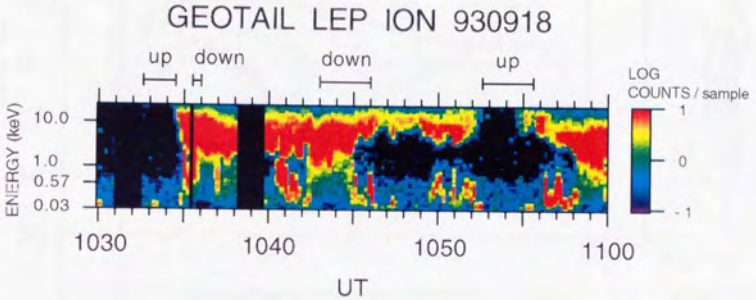
GEOTAIL LEP ION 930918
up
down
H
down
up
LOG
COUNTS / sample
1
0
- 1
ENERGY (keV)
10.0
1.0
0.57
0.03
1030
1040
1050
1100
UT

Figure 5.7

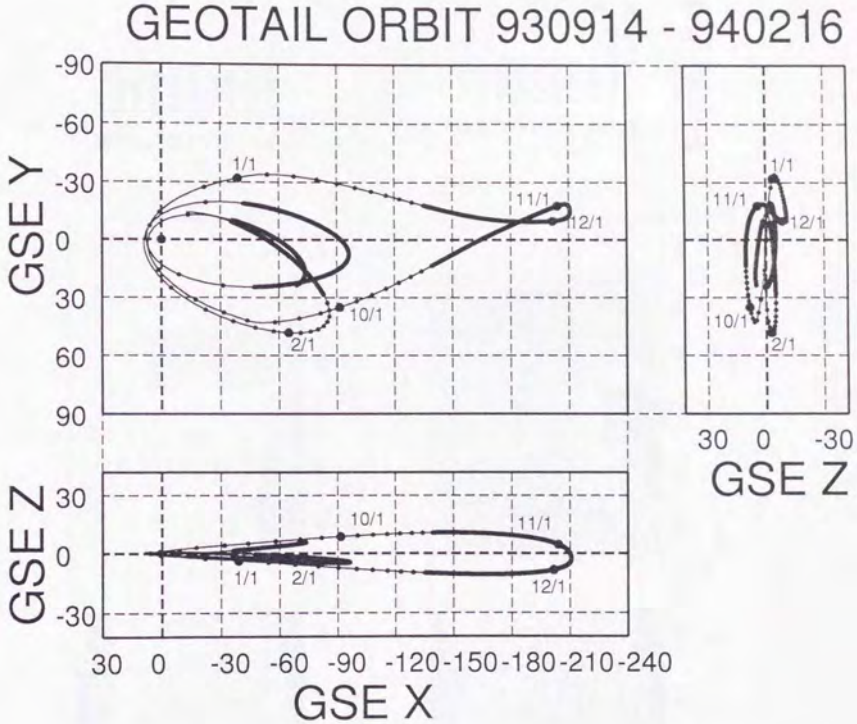
GEOTAIL ORBIT 930914 - 940216
GSE Y
GSE Z
GSE X
-90
-60
-30
0
30
60
90
1/1
11/1
12/1
10/1
2/1
30 0 -30
30 0 -30 -60 -90 -120 -150 -180 -210 -240

Figure 5.8

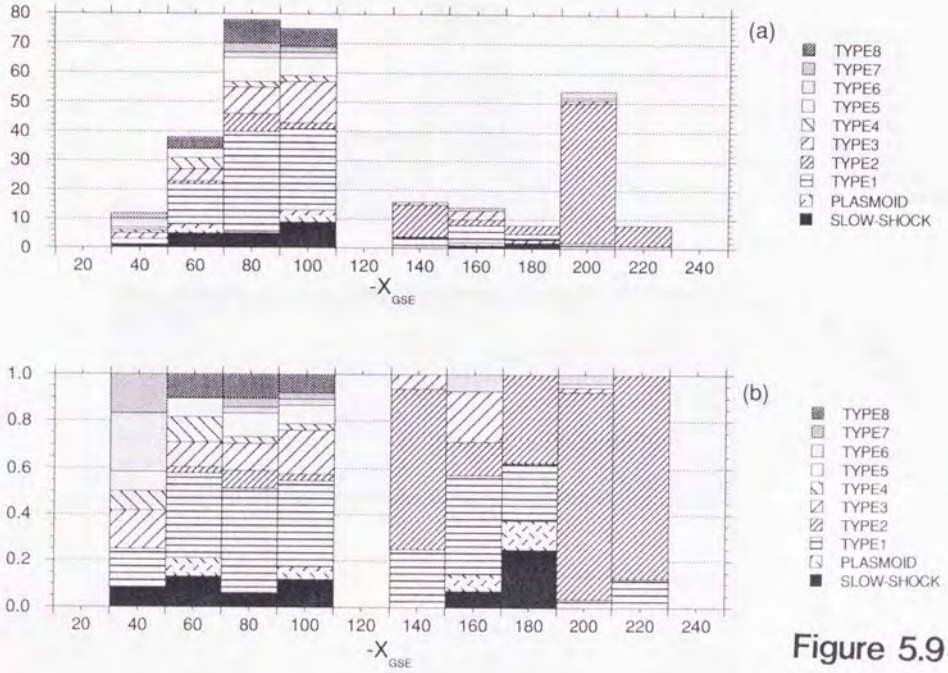
80
70
60
50
40
30
20
10
0
20 40 60 80 100 120 140 160 180 200 220 240
-X GSE
(a)
TYPE8
TYPE7
TYPE6
TYPE5
TYPE4
TYPE3
TYPE2
TYPE1
PLASMOID
SLOW-SHOCK
1.0
0.8
0.6
0.4
0.2
0.0
20 40 60 80 100 120 140 160 180 200 220 240
-X GSE
(b)
TYPE8
TYPE7
TYPE6
TYPE5
TYPE4
TYPE3
TYPE2
TYPE1
PLASMOID
SLOW-SHOCK

Figure 5.9

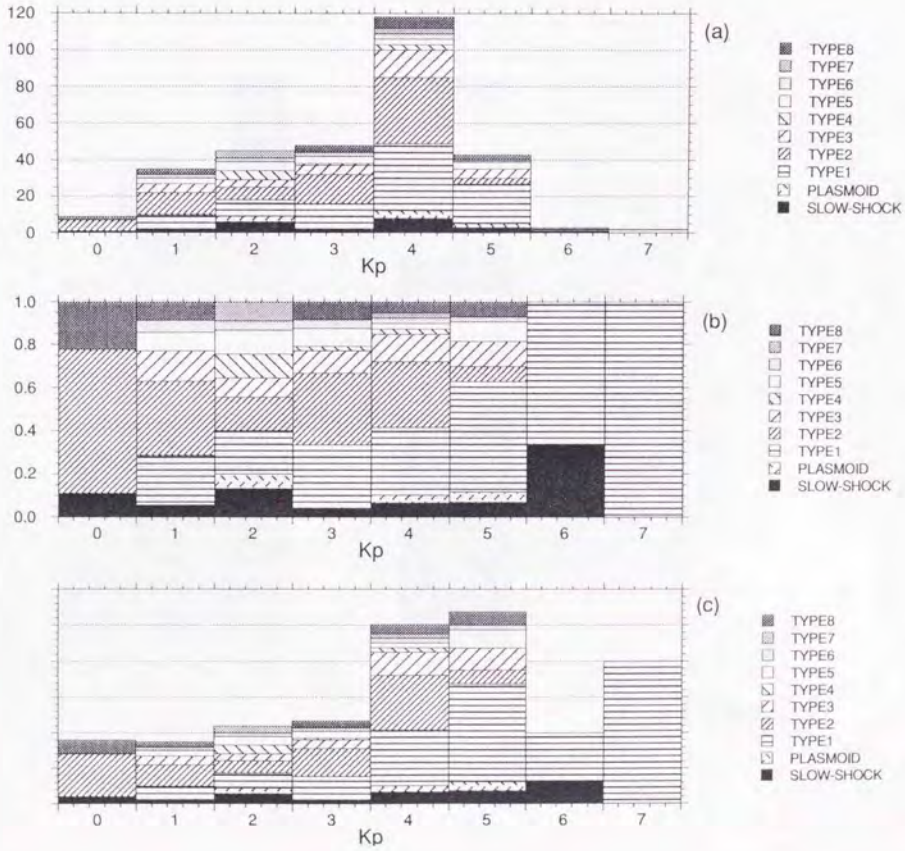
120
100
80
60
40
20
0
0 1 2 3 4 5 6 7
Kp
(a)
TYPE8
TYPE7
TYPE6
TYPE5
TYPE4
TYPE3
TYPE2
TYPE1
PLASMOID
SLOW-SHOCK
1.0
0.8
0.6
0.4
0.2
0.0
0 1 2 3 4 5 6 7
Kp
(b)
TYPE8
TYPE7
TYPE6
TYPE5
TYPE4
TYPE3
TYPE2
TYPE1
PLASMOID
SLOW-SHOCK
0 1 2 3 4 5 6 7
Kp
(c)
TYPE8
TYPE7
TYPE6
TYPE5
TYPE4
TYPE3
TYPE2
TYPE1
PLASMOID
SLOW-SHOCK

Figure 5.10

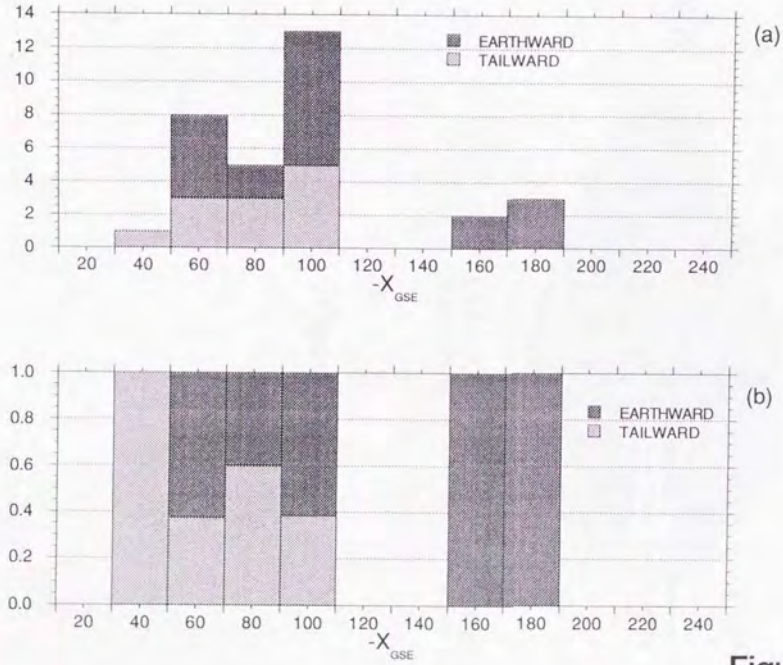
14
12
10
8
6
4
2
0
EARTHWARD
TAILWARD
(a)
20 40 60 80 100 120 140 160 180 200 220 240
-X GSE
1.0
0.8
0.6
0.4
0.2
0.0
EARTHWARD
TAILWARD
(b)
20 40 60 80 100 120 140 160 180 200 220 240
-X GSE

Figue 5.11

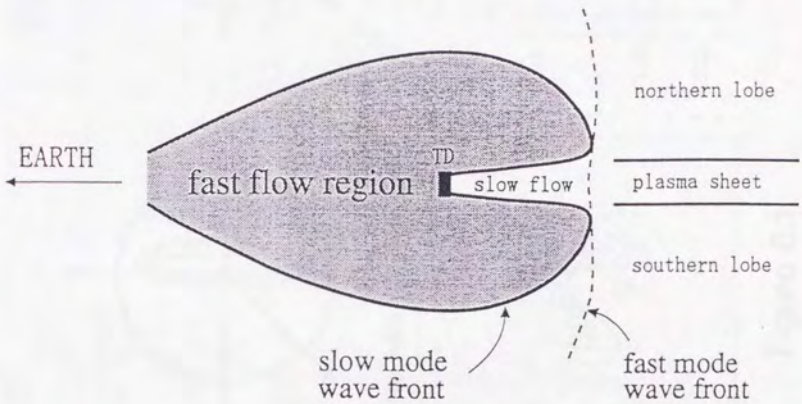
EARTH
fast flow region
TD
slow flow
northern lobe
plasma sheet
southern lobe
slow mode
wave front
fast mode
wave front

Figure 5.12

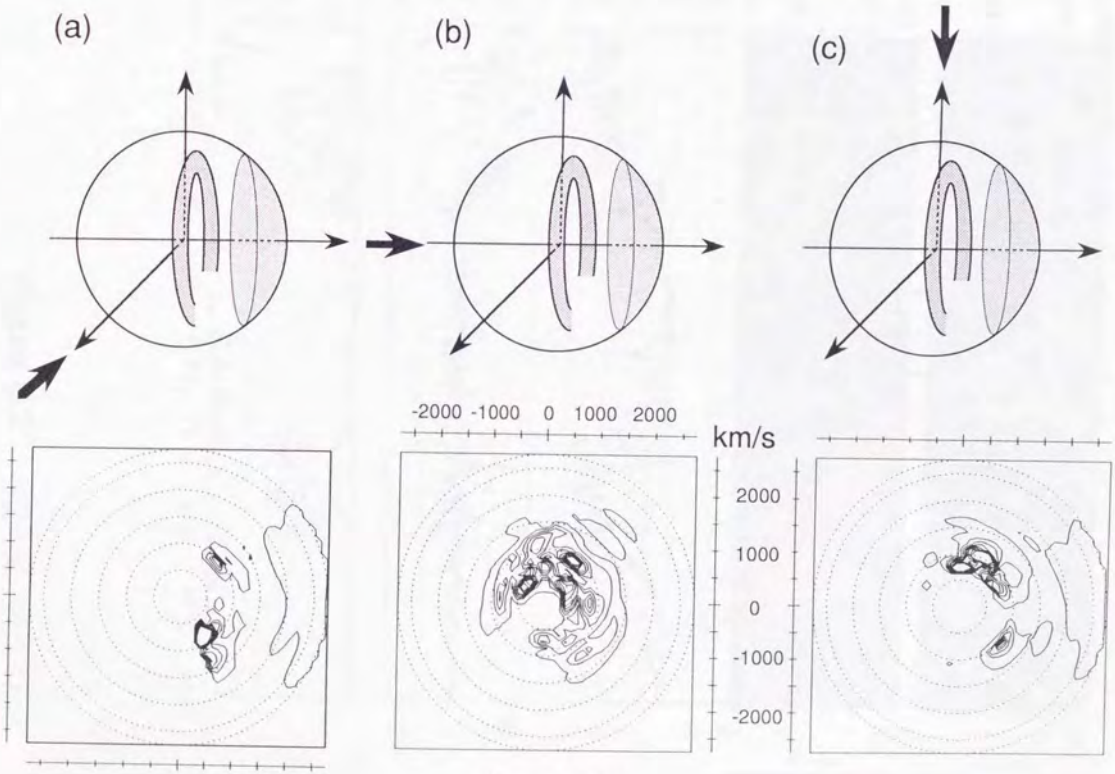

Figure 6.1

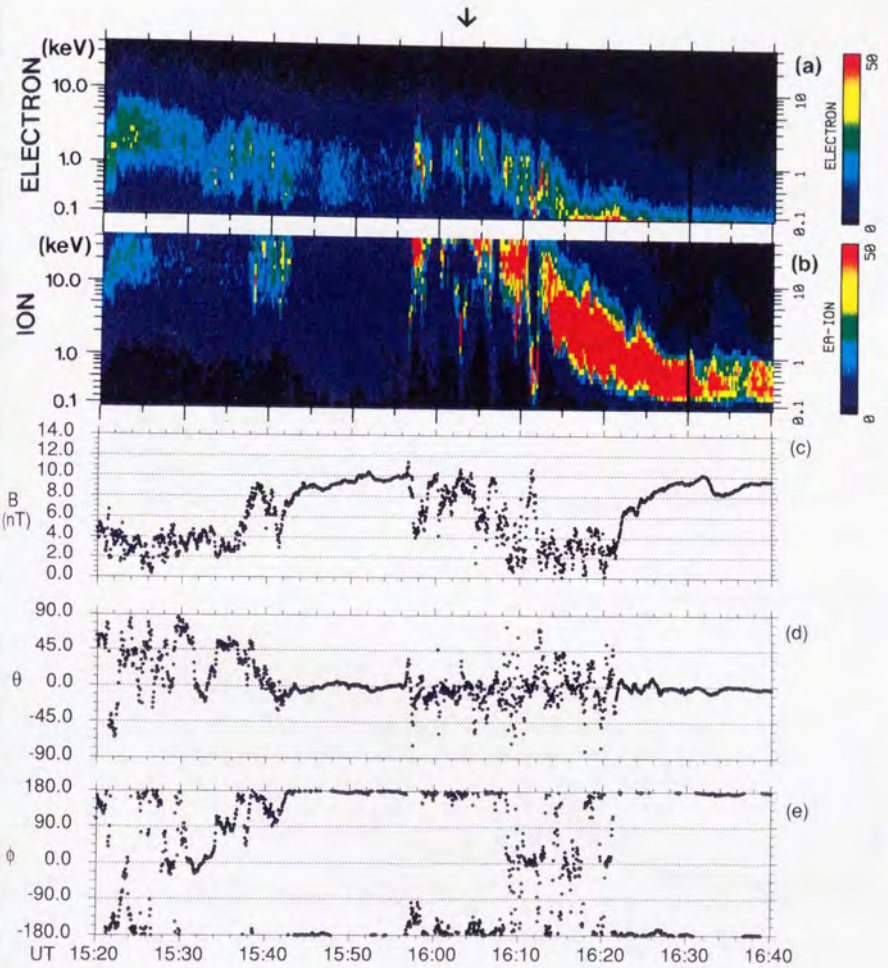
(keV)
ELECTRON
10.0
1.0
0.1
(a)
ELECTRON
50
0
(keV)
ION
10.0
1.0
0.1
(b)
EA-ION
50
0
14.0
12.0
10.0
8.0
6.0
4.0
2.0
0.0
B
(nT)
(c)
90.0
45.0
0.0
-45.0
-90.0
θ
(d)
180.0
90.0
0.0
-90.0
-180.0
ϕ
(e)
UT 15:20
15:30
15:40
15:50
16:00
16:10
16:20
16:30
16:40

Figure 6.2

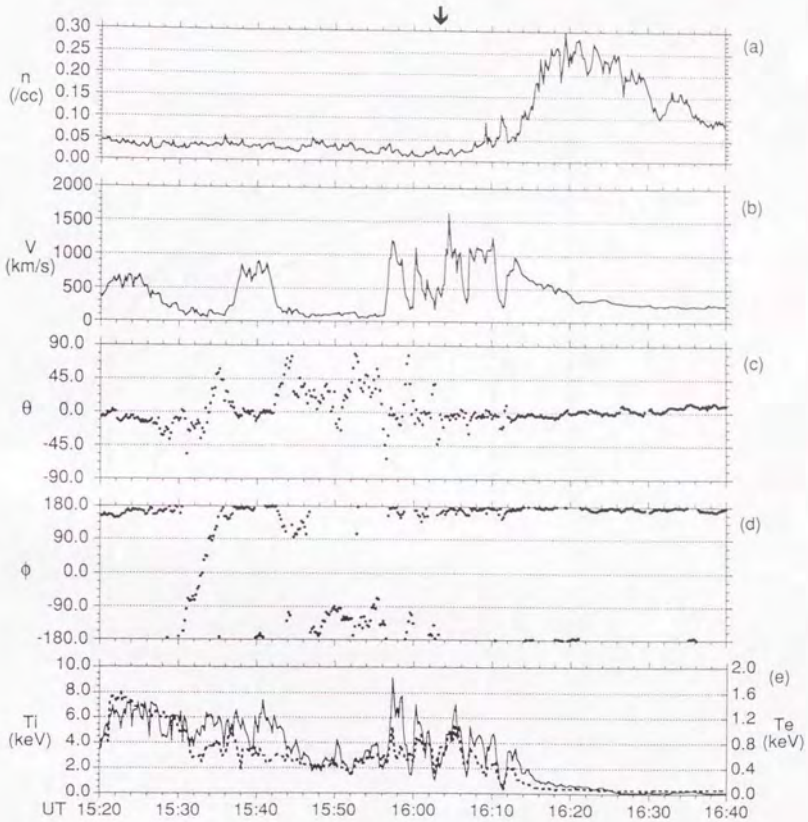
0.30
0.25
0.20
0.15
0.10
0.05
0.00
n
(/cc)
(a)
2000
1500
1000
500
0
V
(km/s)
(b)
90.0
45.0
0.0
-45.0
-90.0
θ
(c)
180.0
90.0
0.0
-90.0
-180.0
ϕ
(d)
10.0
8.0
6.0
4.0
2.0
0.0
Ti
(keV)
2.0
1.6
1.2
0.8
0.4
0.0
Te
(keV)
(e)
UT 15:20
15:30
15:40
15:50
16:00
16:10
16:20
16:30
16:40

Figure 6.3

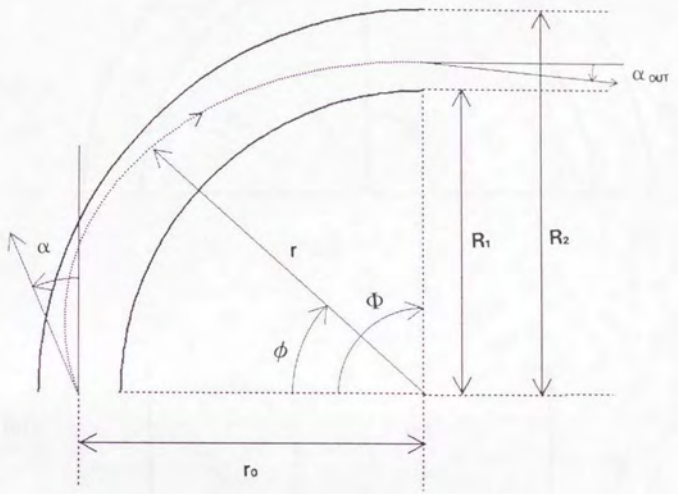

Figure A.1

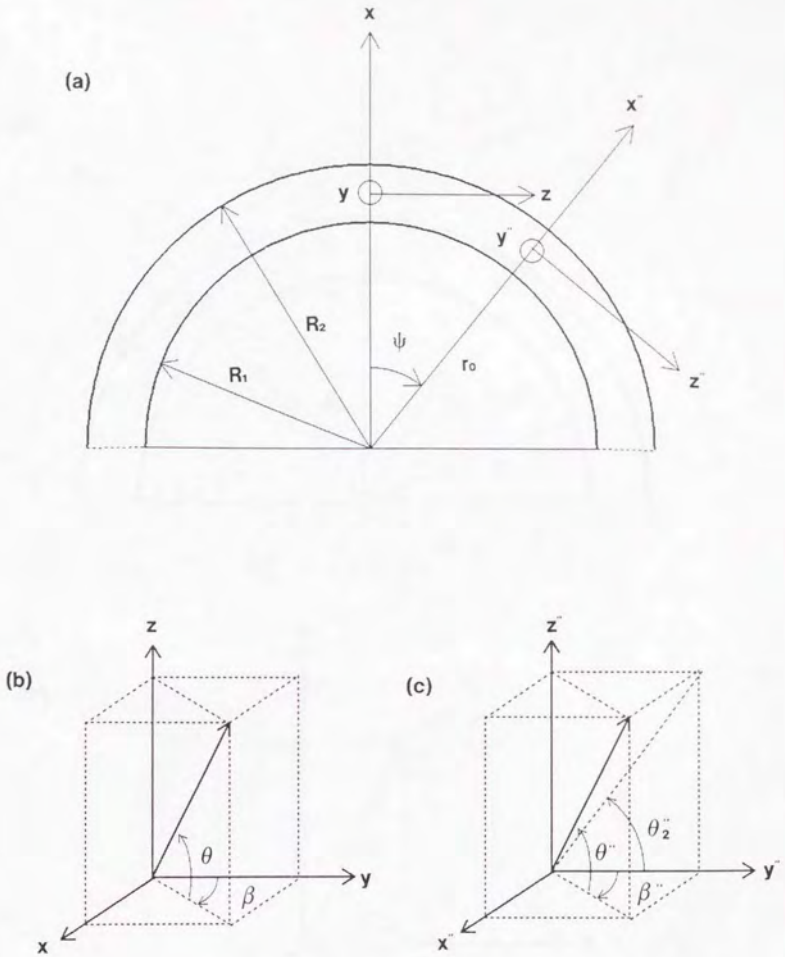

Figure A.2

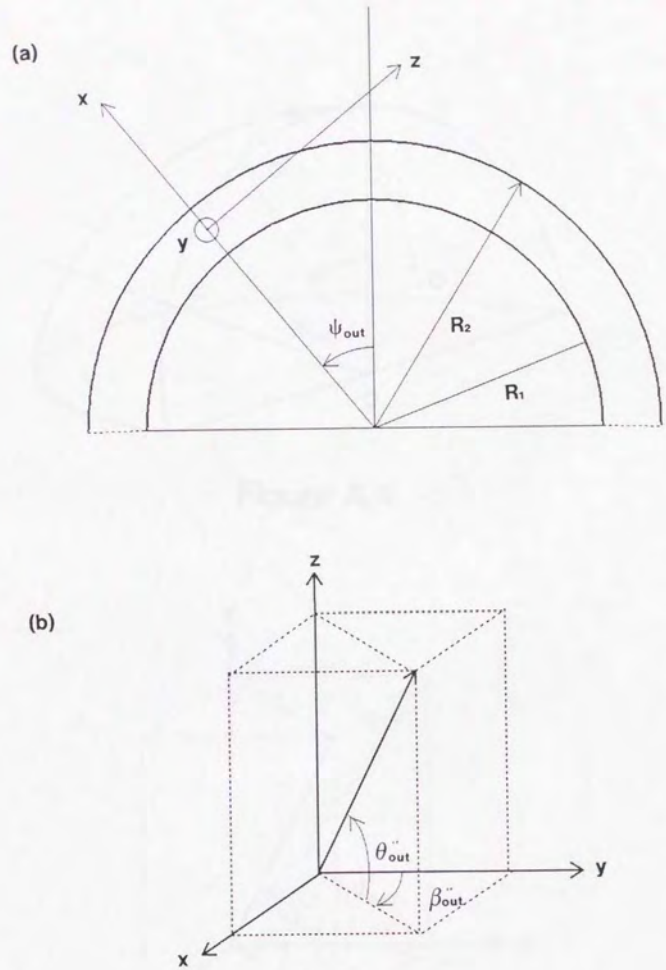

Figure A.3

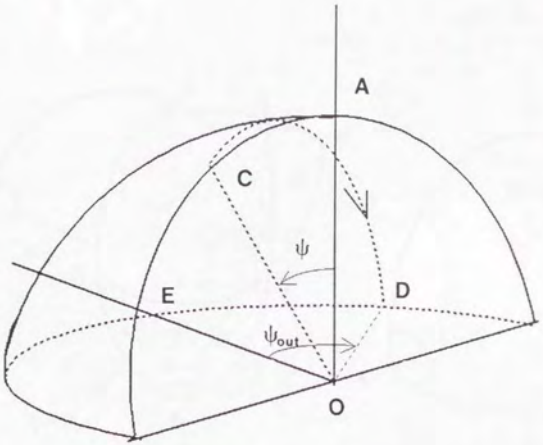

Figure A.4

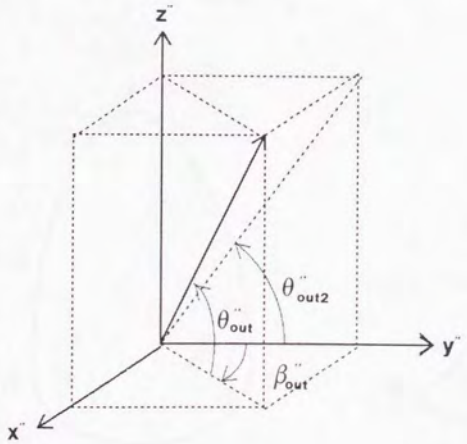

Figure A.5

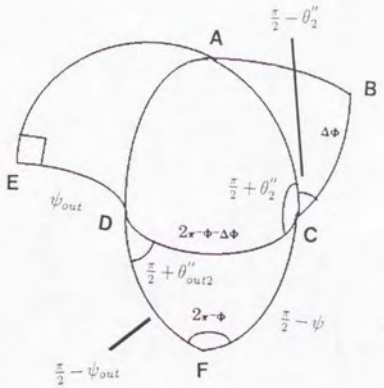

Figure A.6

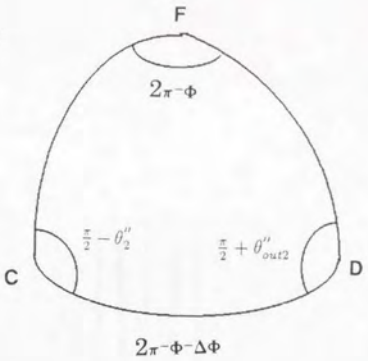

Figure A.7

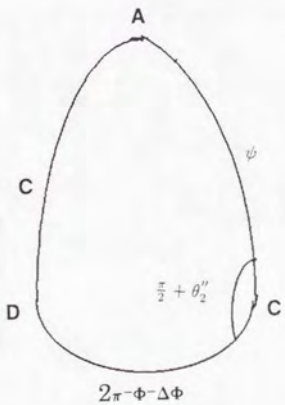

Figure A.8

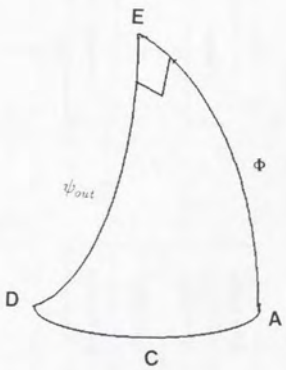

Figure A.9

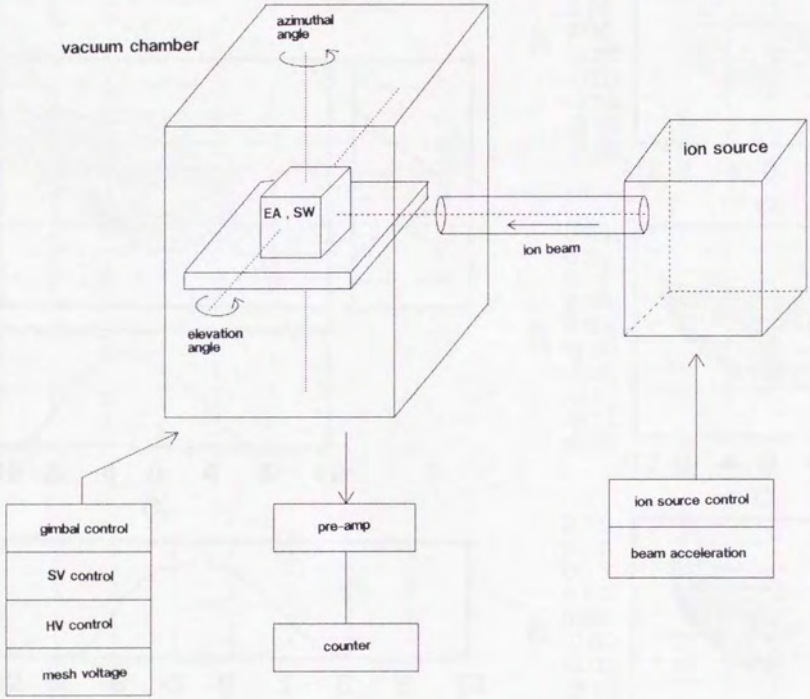
vacuum chamber
azimuthal angle
EA , SW
elevation angle
ion source
ion beam
gimbal control
SV control
HV control
mesh voltage
pre-amp
counter
ion source control
beam acceleration

Figure A.10

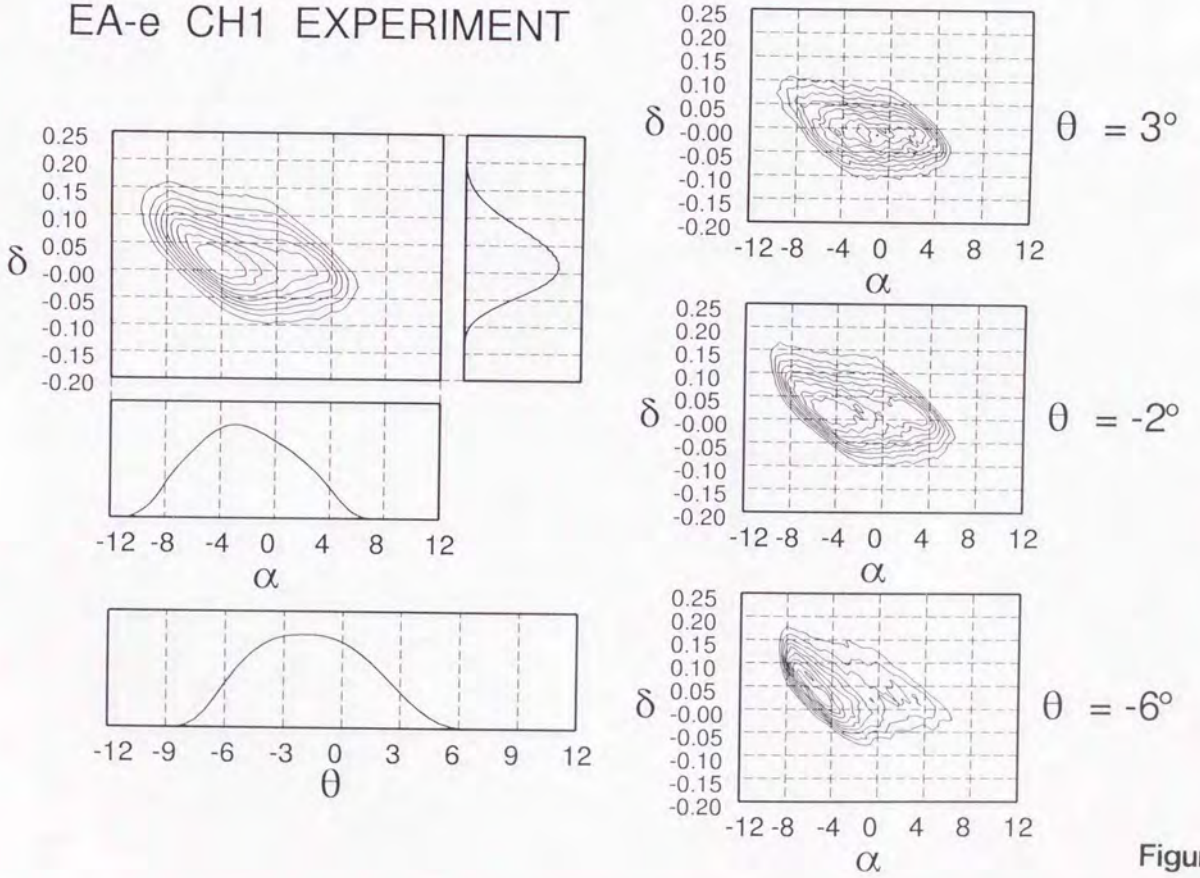
EA-e CH1 EXPERIMENT
δ
0.25
0.20
0.15
0.10
0.05
-0.00
-0.05
-0.10
-0.15
-0.20
-12 -8 -4 0 4 8 12
α
-12 -9 -6 -3 0 3 6 9 12
θ
θ = 3°
θ = -2°
θ = -6°

Figure A.11

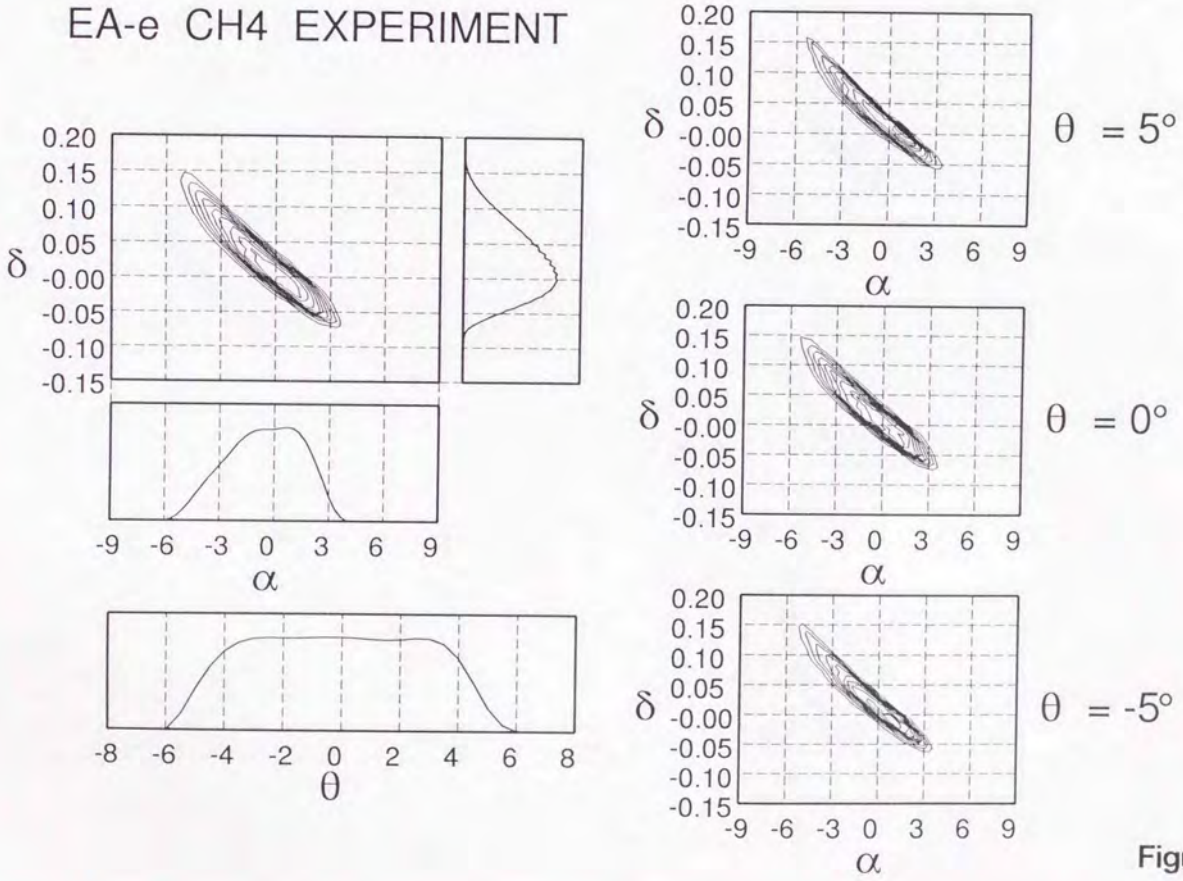
EA-e CH4 EXPERIMENT
δ
0.20
0.15
0.10
0.05
-0.00
-0.05
-0.10
-0.15
-9 -6 -3 0 3 6 9
α
-8 -6 -4 -2 0 2 4 6 8
θ
θ = 5°
θ = 0°
θ = -5°

Figure A.12

EA-i CH1 EXPERIMENT

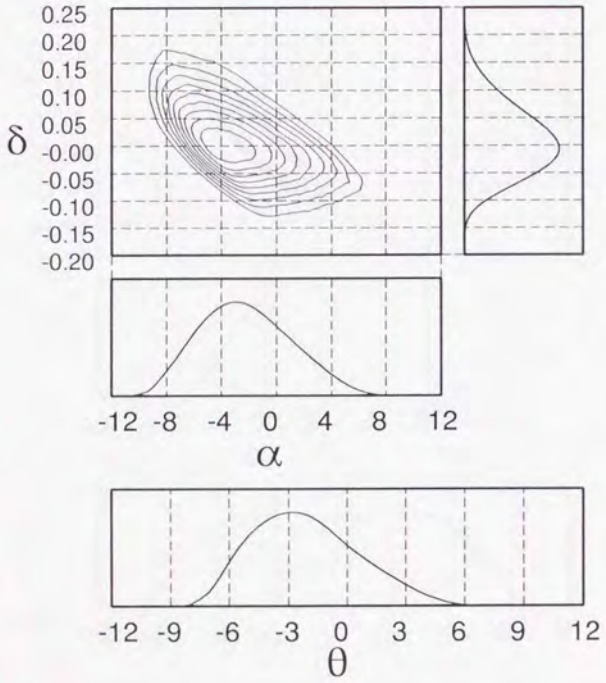

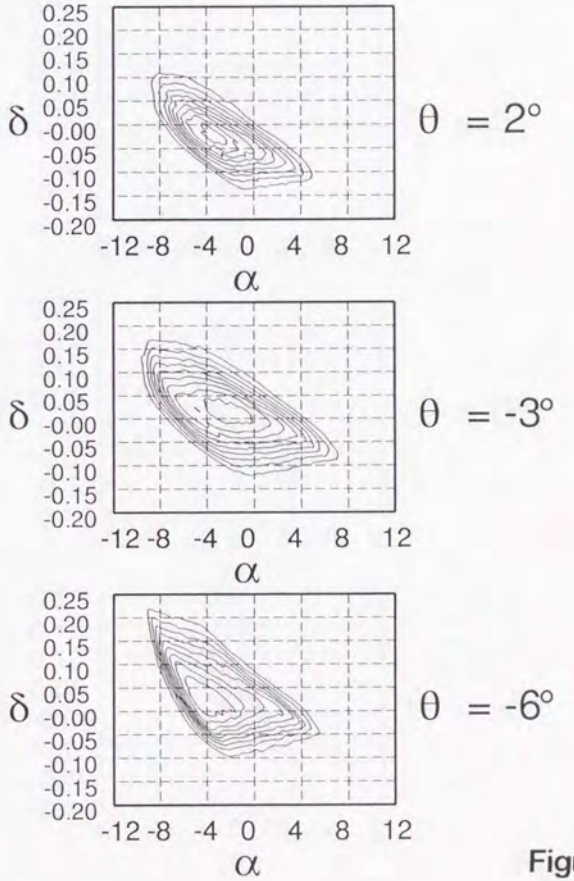

Figure A.13

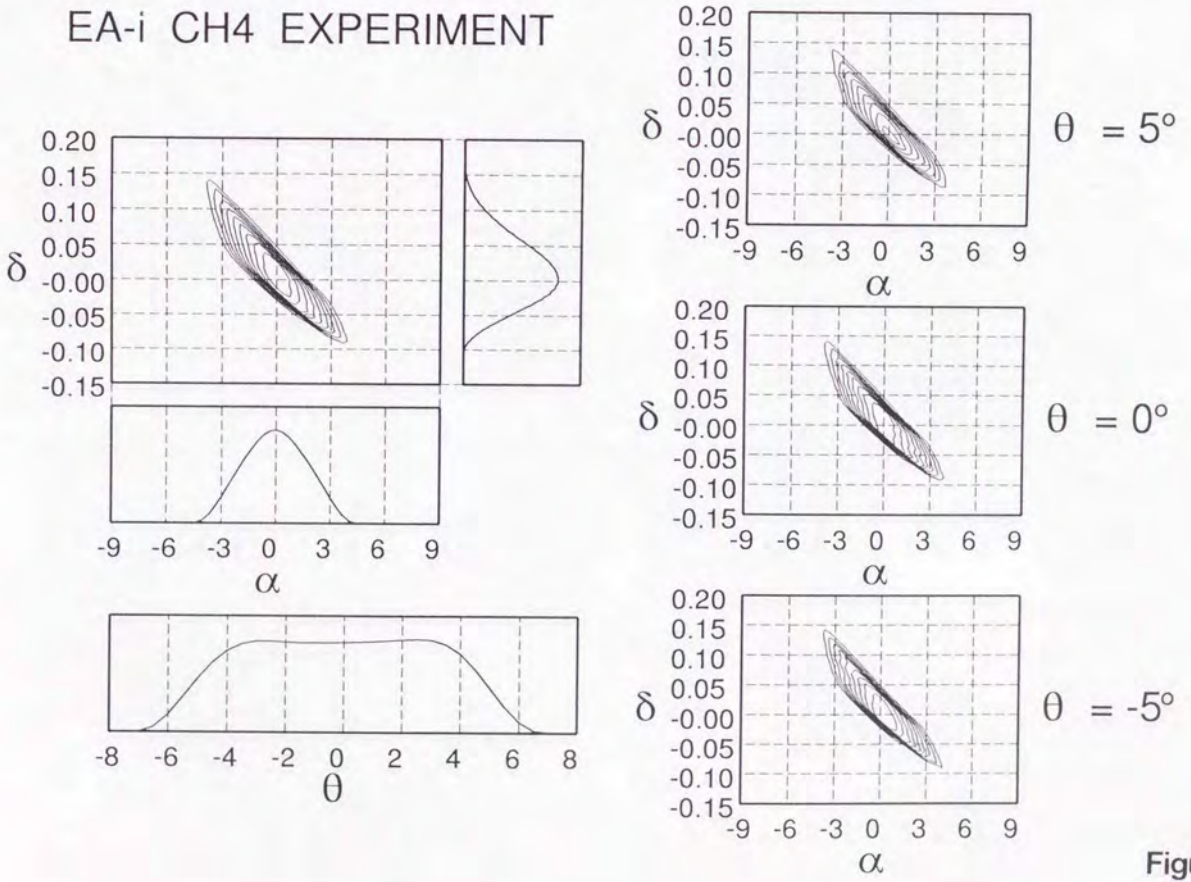

Figure A.14

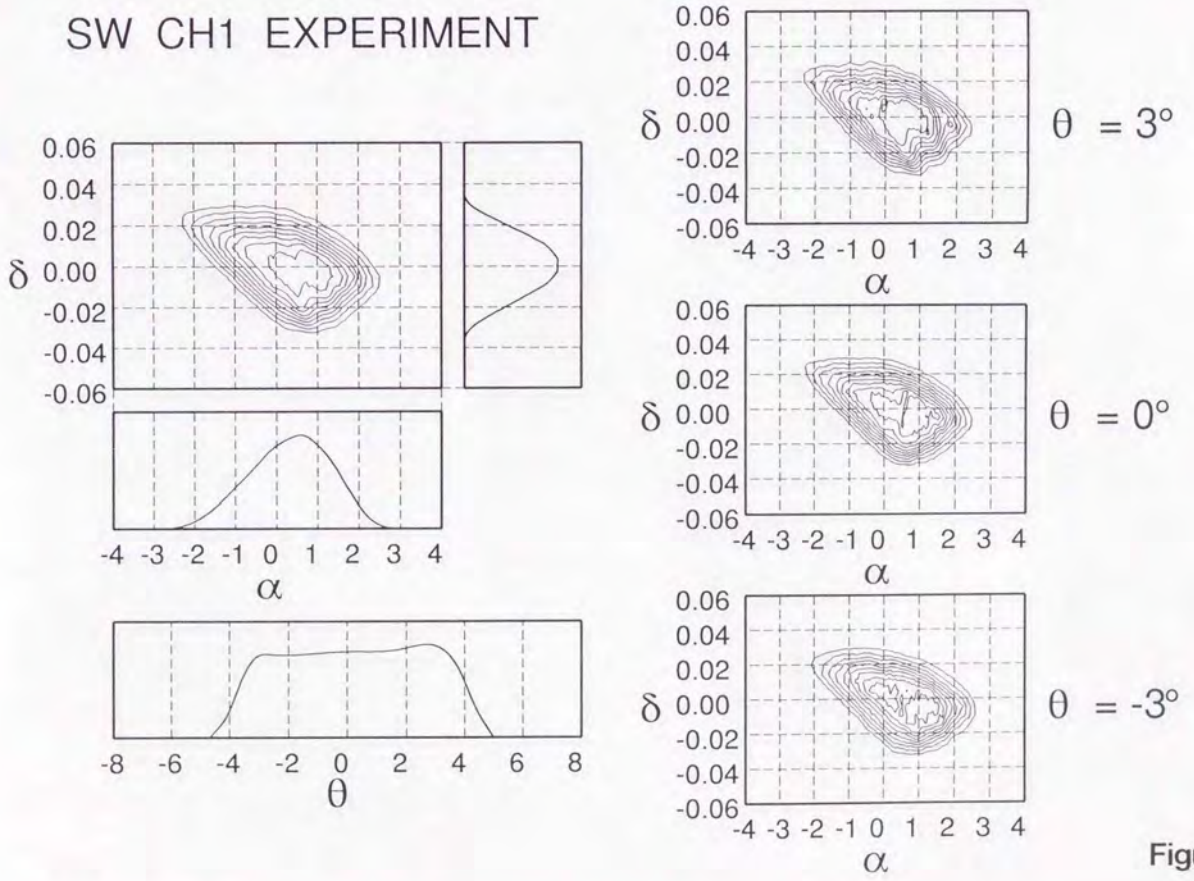
SW CH1 EXPERIMENT
0.06
0.04
0.02
δ 0.00
-0.02
-0.04
-0.06
-4 -3 -2 -1 0 1 2 3 4
α
-8 -6 -4 -2 0 2 4 6 8
θ
θ = 3°
θ = 0°
θ = -3°

Figure A.15

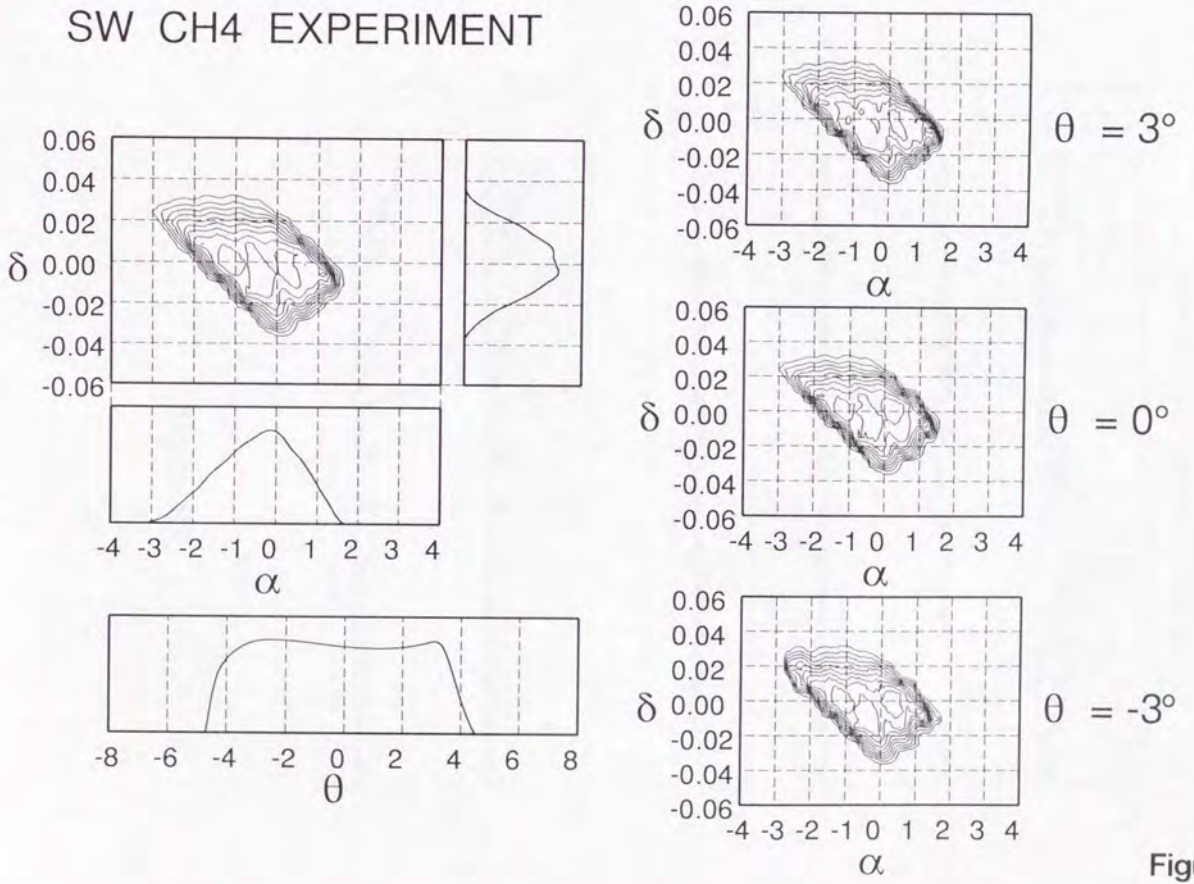
SW CH4 EXPERIMENT
0.06
0.04
0.02
δ 0.00
-0.02
-0.04
-0.06
-4 -3 -2 -1 0 1 2 3 4
α
-8 -6 -4 -2 0 2 4 6 8
θ
θ = 3°
θ = 0°
θ = -3°

Figure A.16

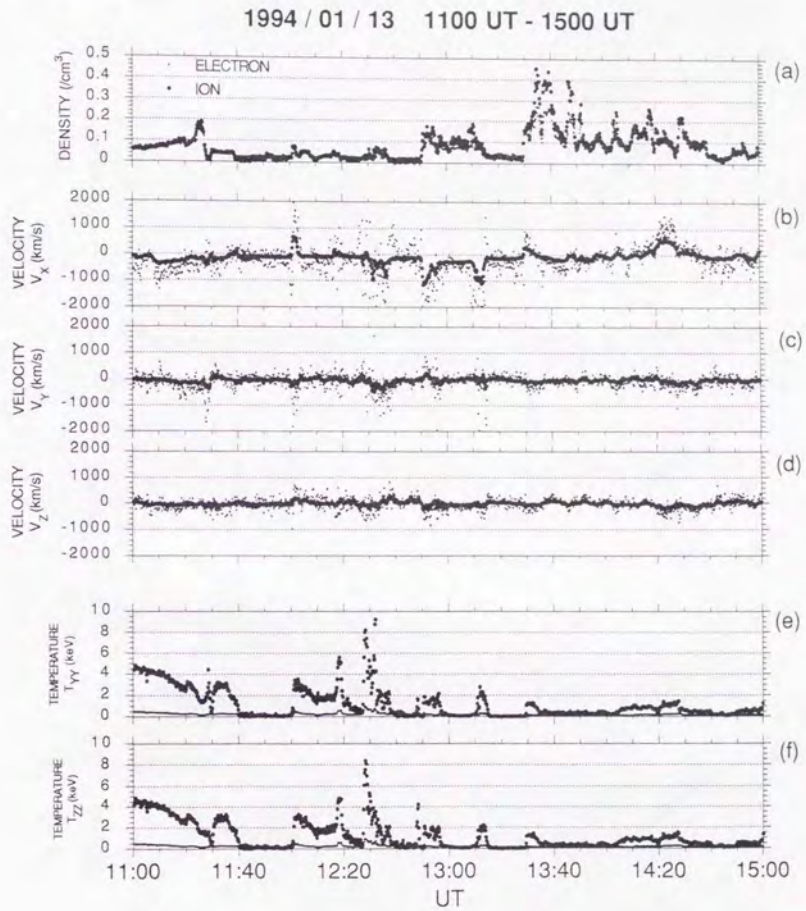
1994 / 01 / 13 1100 UT - 1500 UT
DENSITY (/cm^3)
ELECTRON
ION
(a)
VELOCITY V_X (km/s)
(b)
VELOCITY V_Y (km/s)
(c)
VELOCITY V_Z (km/s)
(d)
TEMPERATURE T_{YY} (keV)
(e)
TEMPERATURE T_{ZZ} (keV)
(f)
11:00
11:40
12:20
13:00
13:40
14:20
15:00
UT

Figure B.1

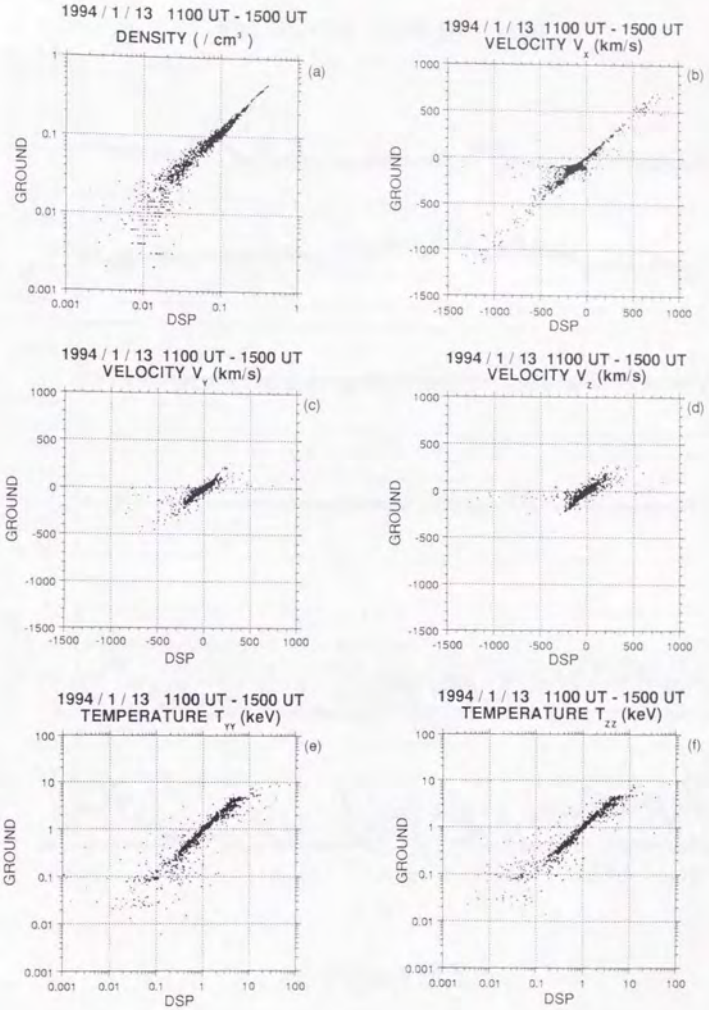
1994 / 1 / 13 1100 UT - 1500 UT
DENSITY (/ cm³)
(a)
GROUND
DSP
1994 / 1 / 13 1100 UT - 1500 UT
VELOCITY V_x (km/s)
(b)
GROUND
DSP
1994 / 1 / 13 1100 UT - 1500 UT
VELOCITY V_y (km/s)
(c)
GROUND
DSP
1994 / 1 / 13 1100 UT - 1500 UT
VELOCITY V_z (km/s)
(d)
GROUND
DSP
1994 / 1 / 13 1100 UT - 1500 UT
TEMPERATURE T_yy (keV)
(e)
GROUND
DSP
1994 / 1 / 13 1100 UT - 1500 UT
TEMPERATURE T_zz (keV)
(f)
GROUND
DSP

Figure B.2

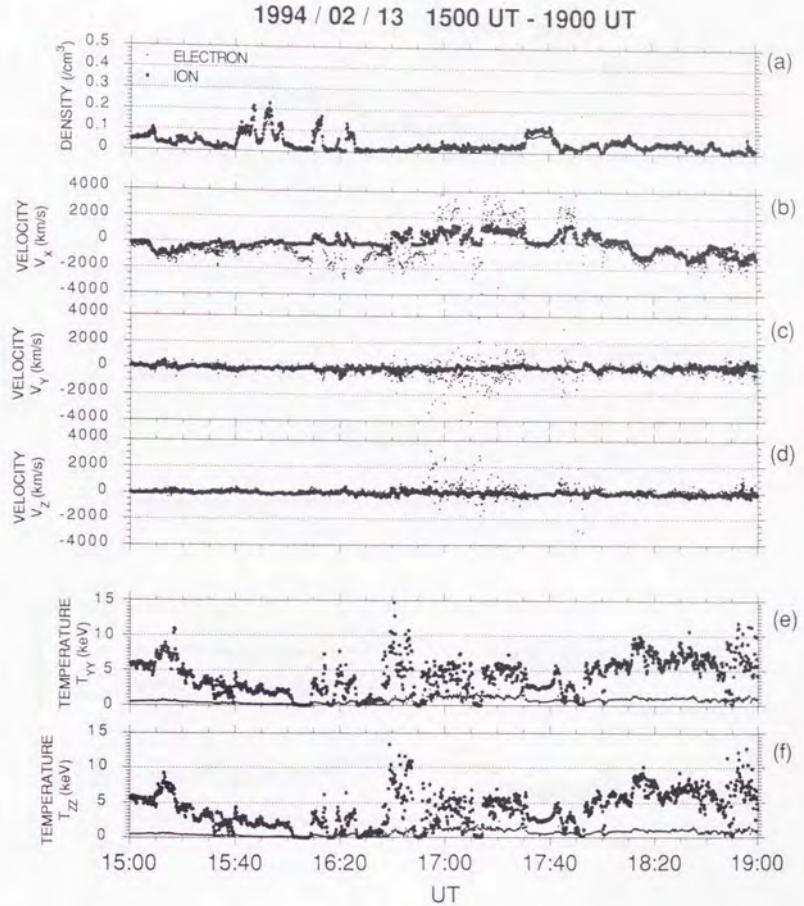
1994 / 02 / 13 1500 UT - 1900 UT
DENSITY (/cm^3)
ELECTRON
ION
(a)
VELOCITY V_X (km/s)
(b)
VELOCITY V_Y (km/s)
(c)
VELOCITY V_Z (km/s)
(d)
TEMPERATURE T_{YY} (keV)
(e)
TEMPERATURE T_{ZZ} (keV)
(f)
15:00
15:40
16:20
17:00
17:40
18:20
19:00
UT

Figure B.3

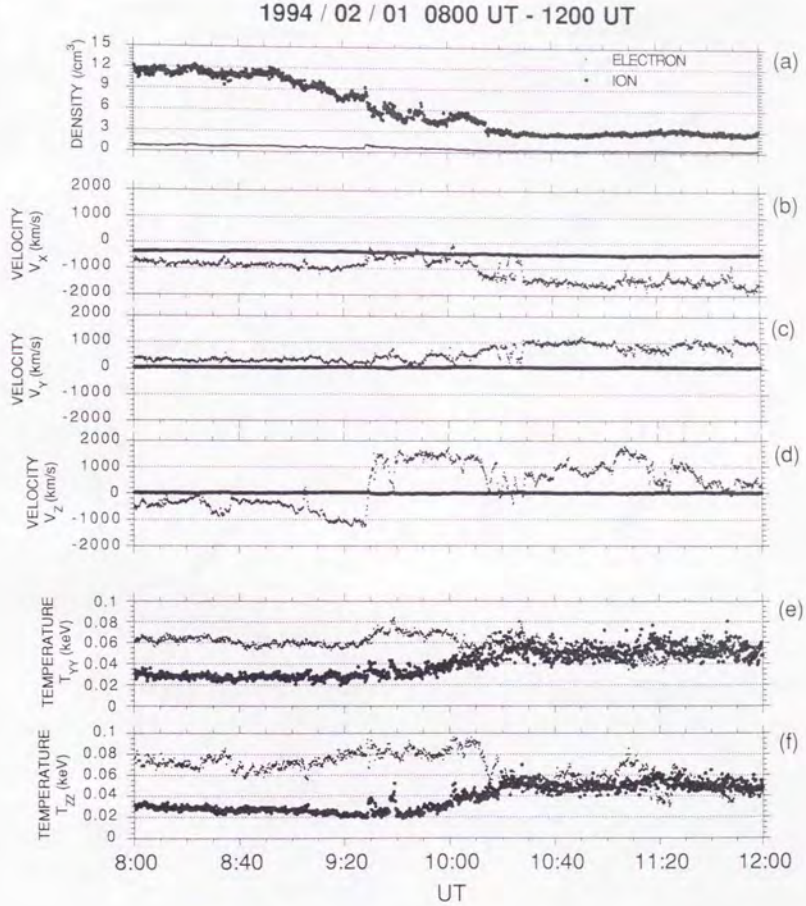
1994 / 02 / 01 0800 UT - 1200 UT
DENSITY (/cm^3)
ELECTRON
ION
(a)
VELOCITY V_X (km/s)
(b)
VELOCITY V_Y (km/s)
(c)
VELOCITY V_Z (km/s)
(d)
TEMPERATURE T_{YY} (keV)
(e)
TEMPERATURE T_{ZZ} (keV)
(f)
8:00
8:40
9:20
10:00
10:40
11:20
12:00
UT

Figure B.4

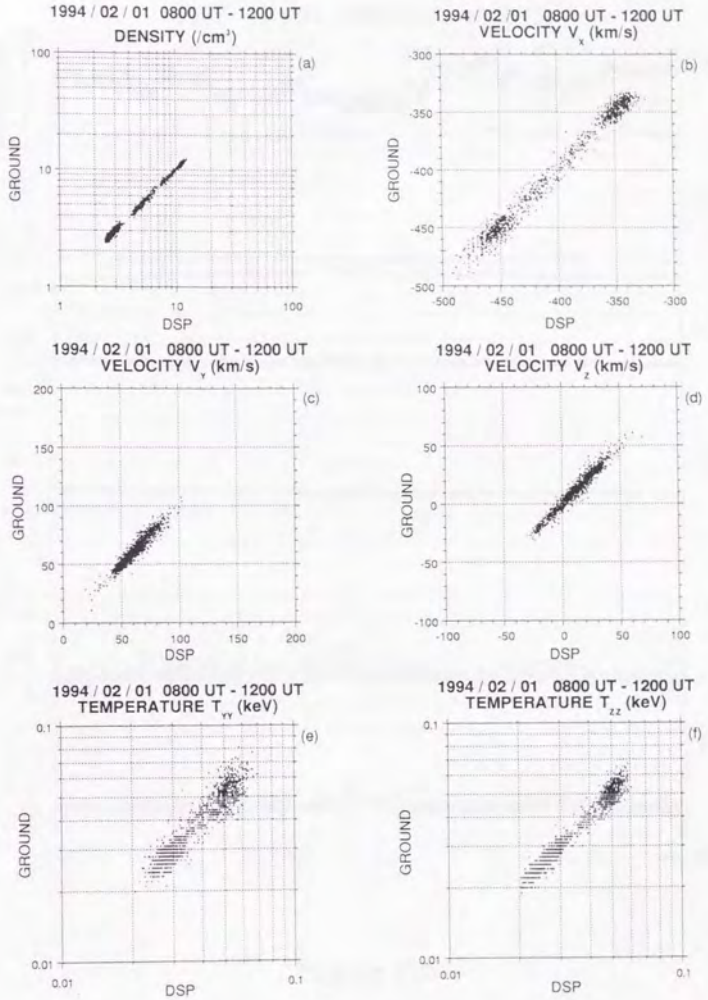
1994 / 02 / 01 0800 UT - 1200 UT
DENSITY (/cm³)
(a)
GROUND
DSP
1994 / 02 /01 0800 UT - 1200 UT
VELOCITY V_x (km/s)
(b)
GROUND
DSP
1994 / 02 / 01 0800 UT - 1200 UT
VELOCITY V_y (km/s)
(c)
GROUND
DSP
1994 / 02 / 01 0800 UT - 1200 UT
VELOCITY V_z (km/s)
(d)
GROUND
DSP
1994 / 02 / 01 0800 UT - 1200 UT
TEMPERATURE T_yy (keV)
(e)
GROUND
DSP
1994 / 02 / 01 0800 UT - 1200 UT
TEMPERATURE T_zz (keV)
(f)
GROUND
DSP

Figure B.5

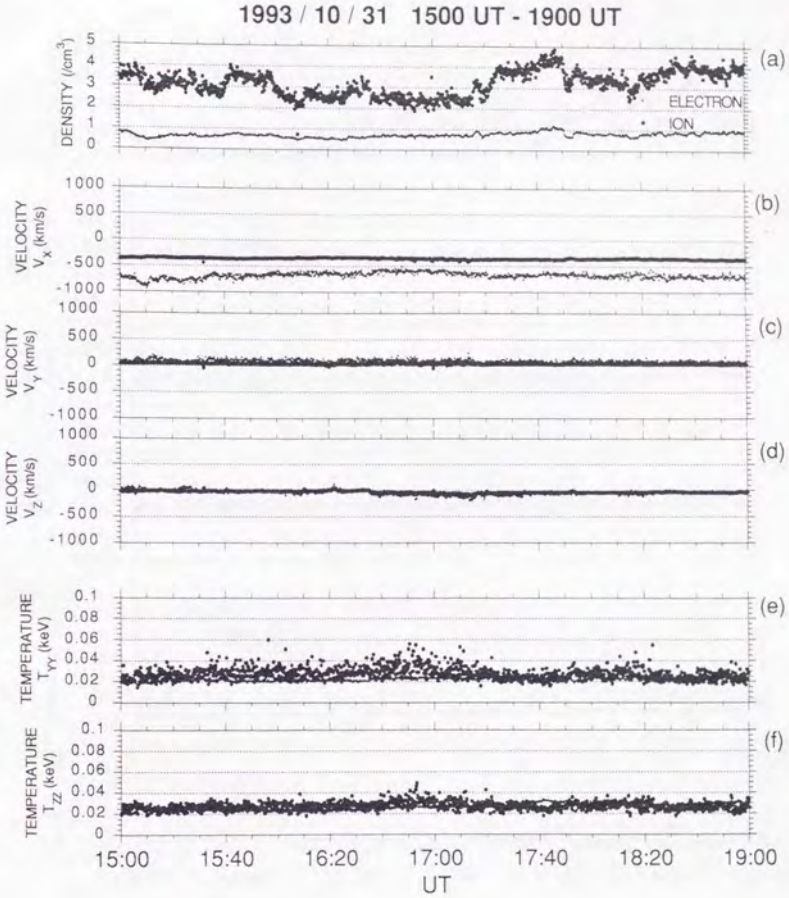
1993 / 10 / 31 1500 UT - 1900 UT
DENSITY (/cm3)
ELECTRON
ION
(a)
VELOCITY Vx (km/s)
(b)
VELOCITY VY (km/s)
(c)
VELOCITY VZ (km/s)
(d)
TEMPERATURE TYY (keV)
(e)
TEMPERATURE TZZ (keV)
(f)
15:00
15:40
16:20
17:00
17:40
18:20
19:00
UT

Figure B.6

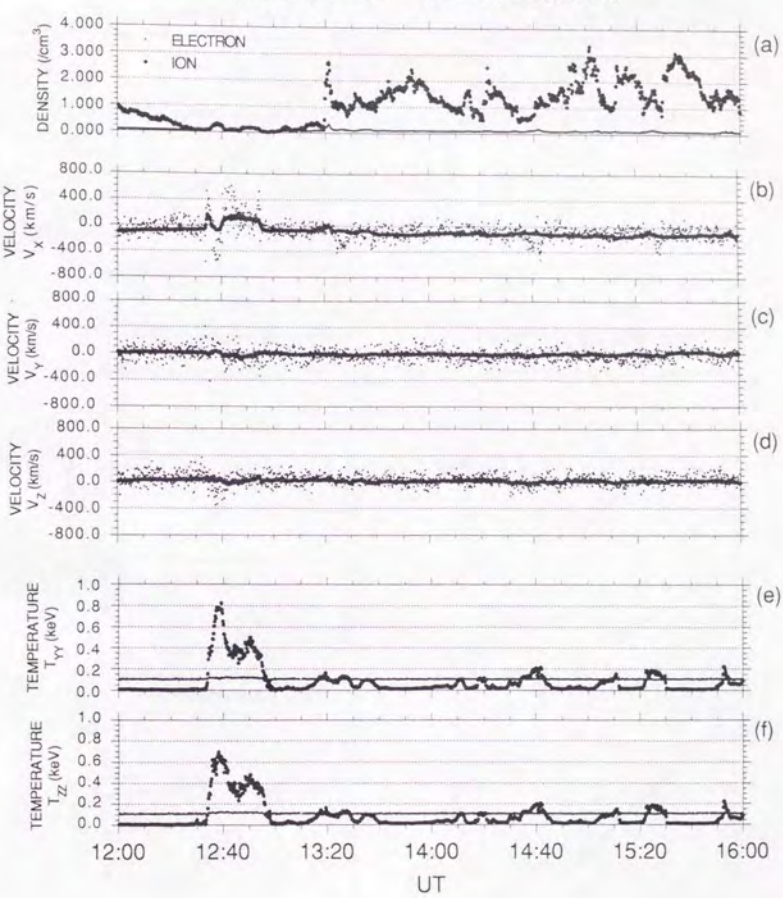
1994 / 01 / 10 1200 UT - 1600 UT
DENSITY (/cm³)
4.000
3.000
2.000
1.000
0.000
ELECTRON
ION
(a)
VELOCITY V_X (km/s)
800.0
400.0
0.0
-400.0
-800.0
(b)
VELOCITY V_Y (km/s)
(c)
VELOCITY V_Z (km/s)
(d)
TEMPERATURE T_YY (keV)
1.0
0.8
0.6
0.4
0.2
0.0
(e)
TEMPERATURE T_ZZ (keV)
(f)
12:00
12:40
13:20
14:00
14:40
15:20
16:00
UT

Figure B.7

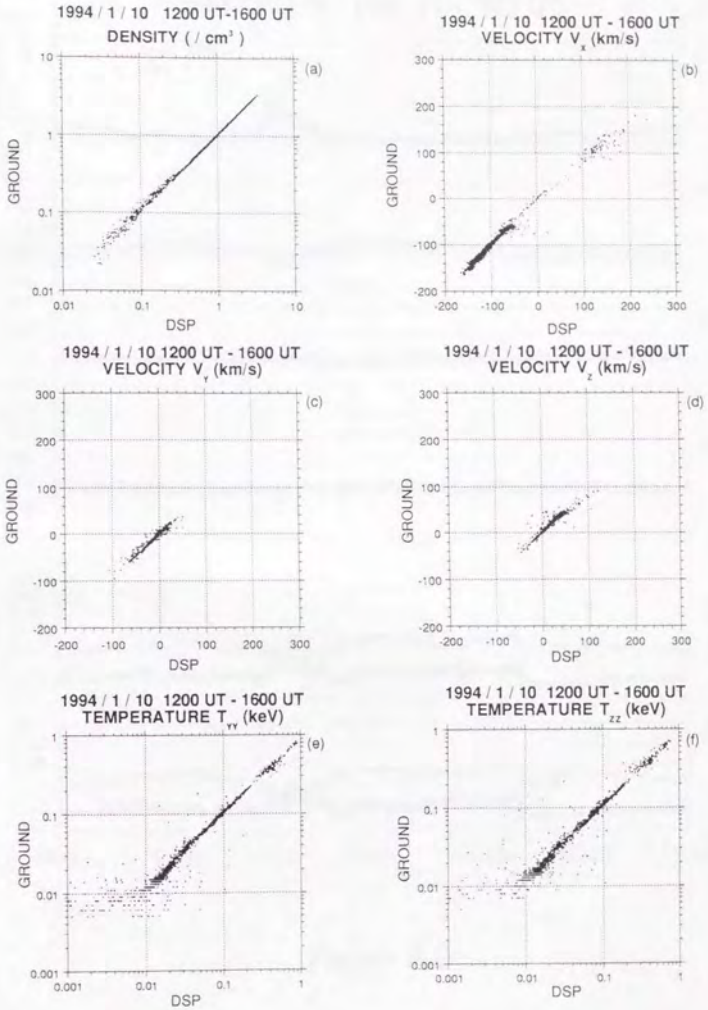
1994 / 1 / 10 1200 UT-1600 UT
DENSITY (/ cm³)
(a)
GROUND
DSP
1994 / 1 / 10 1200 UT - 1600 UT
VELOCITY V_x (km/s)
(b)
GROUND
DSP
1994 / 1 / 10 1200 UT - 1600 UT
VELOCITY V_y (km/s)
(c)
GROUND
DSP
1994 / 1 / 10 1200 UT - 1600 UT
VELOCITY V_z (km/s)
(d)
GROUND
DSP
1994 / 1 / 10 1200 UT - 1600 UT
TEMPERATURE T_yy (keV)
(e)
GROUND
DSP
1994 / 1 / 10 1200 UT - 1600 UT
TEMPERATURE T_zz (keV)
(f)
GROUND
DSP

Figure B.8

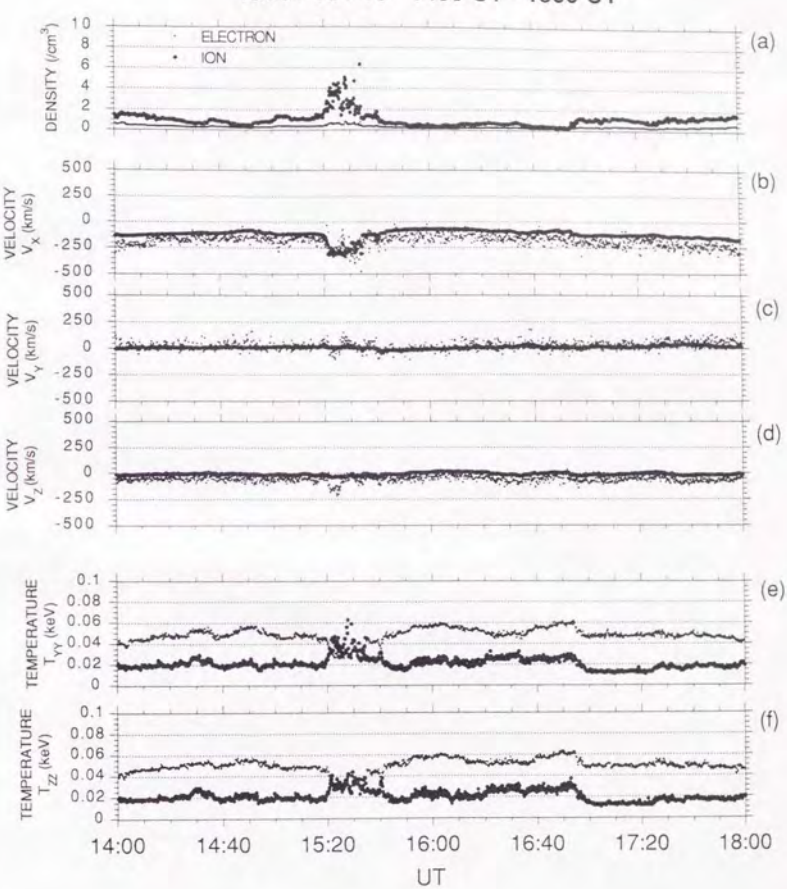
1993 / 10 / 19 1400 UT - 1800 UT
DENSITY (/cm^3)
ELECTRON
ION
(a)
VELOCITY V_X (km/s)
(b)
VELOCITY V_Y (km/s)
(c)
VELOCITY V_Z (km/s)
(d)
TEMPERATURE T_{YY} (keV)
(e)
TEMPERATURE T_{ZZ} (keV)
(f)
14:00
14:40
15:20
16:00
16:40
17:20
18:00
UT

Figure B.9

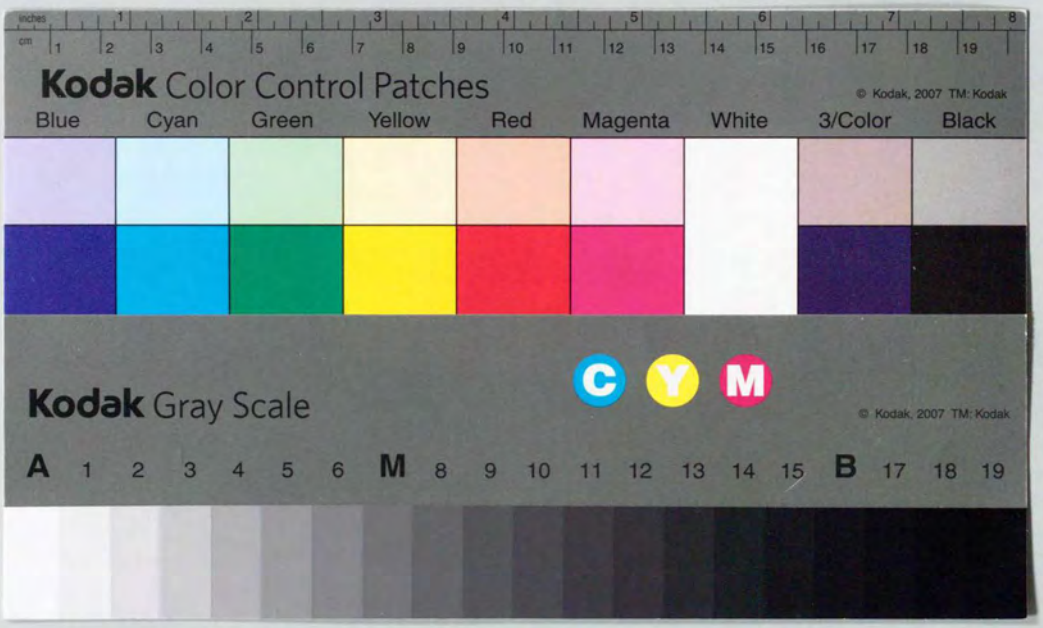
inches
cm
Kodak Color Control Patches
© Kodak, 2007 TM: Kodak
Blue
Cyan
Green
Yellow
Red
Magenta
White
3/Color
Black
C
Y
M
Kodak Gray Scale
© Kodak, 2007 TM: Kodak
A 1 2 3 4 5 6 M 8 9 10 11 12 13 14 15 B 17 18 19